UNIVERSIDADE FEDERAL DE PERNAMBUCO
DEPARTAMENTO DE FÍSICA – CCEN
PROGRAMA DE PÓS-GRADUAÇÃO EM FÍSICA

GABRIEL DA CRUZ BORBA DE ANDRADE

ATOMIC MEMORY USING HIGHER-ORDER NONLINEAR PROCESSES

Recife
2019

GABRIEL DA CRUZ BORBA DE ANDRADE

ATOMIC MEMORY USING HIGHER-ORDER NONLINEAR PROCESSES

Tese apresentada ao Programa de Pós-Graduação em Física da Universidade Federal de Pernambuco, como requisito parcial para a obtenção do título de Doutor em Física.

Área de Concentração: Óptica

Orientador: Prof. Daniel Felinto Pires Barbosa

Co-Orientador: Prof. José Wellington Rocha Tabosa

Recife
2019

Catalogação na fonte
Bibliotecária Arabelly Ascoli CRB4-2068

A553a Andrade, Gabriel da Cruz Borba de
Atomic memory using higher-order nonlinear processes / Gabriel da Cruz Borba de Andrade. – 2019.
111 f.: il., fig.

Orientador: Daniel Felinto Pires Barbosa
Tese (Doutorado) – Universidade Federal de Pernambuco. CCEN. Física. Recife, 2019.
Inclui referências e apêndice.

1. Memórias atômicas. 2. Manipulação de informação. 3. Ordens de não linearidade mais altas. I. Barbosa, Daniel Felinto Pires (orientador). II. Título.

535.2 CDD (22. ed.) UFPE-FQ 2019-60

GABRIEL DA CRUZ BORBA DE ANDRADE

ATOMIC MEMORY USING HIGHER-ORDER NONLINEAR PROCESSES

Tese apresentada ao Programa de Pós-Graduação em Física da Universidade Federal de Pernambuco, como requisito parcial para a obtenção do título de Doutor em Física.

Aprovada em: 04/07/2019.

BANCA EXAMINADORA

_____
Prof. Daniel Felinto Pires Barbosa
Orientador
Universidade Federal de Pernambuco

_____
Prof. Lúcio Hora Acioli
Examinador Interno
Universidade Federal de Pernambuco

_____
Profa. Sandra Sampaio Viana
Examinadora Interna
Universidade Federal de Pernambuco

_____
Profa. Martine Patricia Arlette Chevrollier
Examinadora Externa
Universidade Federal Rural de Pernambuco

_____
Prof. Thierry Marcelino Passerat de Silans
Examinador Externo
Universidade Federal da Paraíba

Abstract

Quantum memories are essential for many tasks in quantum information, especially for long-distance quantum communication protocols, where optical memory would be essential to the synchronization of the different segments of a linear chain of pairs of entangled atomic ensembles. Implementations of atomic-ensemble quantum memory have been carried out using different techniques. Many of them employ essentially first-order ground-state coherences to store the phase information of the incident fields, being the overall nonlinear process of storage and retrieval characterized by the third-order nonlinear susceptibility $\chi^{(3)}$ of the atomic medium, which is connected to four-wave mixing. The present work explores new possibilities for the selective storage of higher order nonlinearity in a sample of cold atoms confined in a magneto-optical trap. Particularly, we demonstrate the storage of a third-, fifth-, and seventh-order nonlinear atom-light interaction into the Zeeman structure of hyperfine cesium $6S_{1/2}$, $F = 3$ ground state. The writing process creates gratings associated with these higher-order nonlinear processes, which can be selectively read by the read beam after a controlled storage time. During this writing process, two different types of grating are formed: coherence and population gratings. Each of them stores only specific orders of nonlinearities, which implies that part of the information is stored in the populations and the other part in the ground-state coherence, leading to particular features in the signal of each order. We also demonstrated that such memories were able to both store and manipulate the orbital angular momentum (OAM) of an input field, obtaining outputs with topological charges that were algebraic functions of the input topological charges. For example, one can retrieve the double or triple of the input topological charges for the memories based on the $\chi^{(5)}$ or $\chi^{(7)}$ processes, respectively. The mechanisms of the nonlinear atomic memory are theoretically analyzed since the creation of the grating until the extraction of the field D, permitting a quantitative calculation of the important physical features. Since such higher-order nonlinearities are associated with processes involving a larger number of photons, this kind of memory can in principle be used to generate multiple quantum-correlated photons, opening the possibility to extend the capability of many quantum information protocols. In this context, we propose a concrete method to generate triplets of correlated photons based on a $\chi^{(5)}$ memory. Finally, we also demonstrate that a Laguerre-Gauss mode can be amplified through a nonlinear stimulated Raman process. This could be important for applications in classical communication using OAM.

Keywords: Atomic memories. Manipulation of information. Higher-order nonlinearities.

Resumo

Memórias quânticas são essenciais para várias tarefas em informação quântica, especialmente em protocolos de comunicação quântica para longas distâncias, onde a memória seria essencial para a sincronização de diferentes segmentos de uma cadeia linear de pares de ensembles emaranhados. Implementações de memórias quânticas em ensembles atômicos veem sendo realizadas utilizando diferentes técnicas. Muitas delas empregam essencialmente coerências de primeira ordem de estados fundamentais para armazenar a informação de fase dos campos incidentes, onde o processo total de armazenamento e recuperação é caracterizado por uma susceptibilidade não linear de terceira ordem, $\chi^{(3)}$, que está conectada com processos de mistura de quatro ondas. O presente trabalho explora novas possibilidades de armazenamento seletivo de ordens de não linearidade numa amostra de átomos frios confinados em uma armadilha magneto-ótica. Particularmente, demonstramos o armazenamento da terceira, quinta e sétima ordem de não linearidade da interação átomo-luz na estrutura Zeeman do estado hiperfino $6S_{1/2}$, $F = 3$ do césio. O processo de escrita cria grades associadas com processos de altas não linearidades, que podem ser seletivamente lidos por um feixe de leitura depois de um tempo de armazenamento escolhido. Durante este processo de escrita, dois tipos diferentes de grades são formadas: grades de coerência e grades de população. Cada uma delas armazena apenas ordens específicas de não linearidades, implicando que parte da informação é armezanada nas populações e a outra parte é armazenada nas coerências dos estados fundamentais, levando a características particulares no sinal de cada ordem. Também demonstramos que estas memórias são capazes de armazenar e manipular o momento angular orbital (MAO) de um campo de entrada, obtendo campos de saída com cargas que são funções algébricas das cargas topológica de entrada. Por exemplo, pode-se recuperar o dobro ou o triplo da carga topológica original para as memórias relacionadas aos processos de $\chi^{(5)}$ e $\chi^{(7)}$, respectivamente. Os mecanismos da memória atômica não linear são analisados também teoricamente desde a criação da grade até a extração do campo D, permitindo um cálculo quantitativo de importantes aspectos físicos. Já que tais ordens de não linearidade estão naturalmente associadas com processos envolvendo um maior número de fótons, estas memórias podem, em princípio, ser usadas para gerar múltiplos fótons correlacionados, abrindo a possibilidade de extender a capacidade de vários protocolos de informação quântica. Neste contexto, propomos um método concreto para gerar tripletos de fótons correlacionados baseado na memória de $\chi^{(5)}$. Finalmente, também demonstramos que um modo de Laguerre-Gauss pode ser amplificado através de um processo Raman estimulado, o que pode se mostrar valioso para aplicações em comunicação clássica utilizando MAO.

Palavras-chave: Memórias atômicas. Manipulação de informação. Ordens de não linearidade mais altas.

Contents

Chapter 1

Introduction

1.1 The necessity of quantum memories

The field of quantum information processing (QIP) has driven great interest of the physics community in the past few decades due to the promise of solving problems intractable by classical means. Quantum computing, which would allow to perform tasks believed to be impossible with its classical analog [1], quantum cryptography, which would allow secure key distribution [2], and teleportation [3, 4] are a few examples. Practical implementations of these new technologies usually depends on the utilization of quantum memories. In reality, quantum memories are needed in any application that demands synchronization of several independent and probabilistic processes. Since in these tasks the information is encoded in the quantum state, a quantum memory would be a device capable of storing and recovering the quantum state.

The motivation that triggered the development of quantum memories for communication, and still one of the most important goals today, are the quantum repeaters for long-distance quantum communication [5, 6, 7]. After the proposition of the quantum repeaters many other applications were found leading to intense experimental and theoretical endeavors [8, 9, 10, 11]. Here we present a few of these applications in the context of quantum networks, where memories are essential.

1.1.1 Quantum Network

Broadly speaking a network is a system consisting in similar parts that are connected together and sharing information. In classical computing it could be a computer connected to other computers or to the internet.

In the case of a quantum network the idea is similar [12, 13]. Quantum information is produced and processed inside individual quantum nodes. The information travels from one site to another through quantum channels, which are usually photons. Obviously, it is necessary to convert the quantum state from the atoms to the photons in a reversible way, such that it can be transferred from the node to the photon and then transferred again to another node. This general idea can apply to a quantum computer or a quantum communication system.

1.1.2 Distributed quantum computation

In a quantum computer one must have hundreds of entangled qubits. The problem is that to maintain and control such entanglement for a long time is very difficult in a practical implementation, and this difficulty grows as one adds more and more qubits. Therefore, even though control of small systems is well established for many systems, like ions [14], scaling is still challenging. This could be circumvented by breaking the computer in smaller units that would process the information in parallel to be joined in the end [15]. Quantum memories are crucial for linking all these units.

1.1.3 Quantum Communication

The concept is analogous for long-distance quantum communication using quantum repeaters. Maximally entangled states are used in most of quantum communication protocols. The problem is that direct distribution of entanglement over long distances becomes impossible due to losses and decoherence during transmission. In classical communication one can introduce amplifiers periodically throughout the path, avoiding any significant degradation of the signal. A direct generalization to the quantum mechanical case is foiled by the no-cloning theorem, which states that one can not conceive a universal device capable of cloning (and as a consequence, amplifying) an arbitrary quantum state [16, 17]. Fortunately, this hindrance can be circumvented by the inclusion of the quantum repeaters [6, 7]. The idea of a quantum repeater is to divide the total distance into shorter segments, where entanglement purification is performed in each node that are subsequently connected by entanglement swapping. Protocols using this concept, like the DLCZ protocol [5], are intrinsically probabilistic, forcing all parts of the network to succeed at the same time if no memory is available. Therefore, the optical memory would be essential to the synchronization of the different segments.

Many physical systems can be used to implement such idea. Here we highlight atomic ensembles, since the results of this thesis are taken using a magneto-optical trap. Successful implementation of atomic ensemble quantum memory has been carried out in many different physical systems, such as electromagnetically induced transparency (EIT) [18, 19], gradient echo memories (GEM) [20], and atomic frequency combs (AFC) [21].

1.2 Quantum memories with processing capabilities

As we stated before, photons are the ideal carriers of quantum information over long distances due to their negligible interaction in free space. However, this also constitutes a problem, since processing demands some sort of interaction between photons. This means that once the photon leaves a node its quantum state can not be easily changed. To circumvent this dilemma one could use a medium to somehow enable photon-photon interaction through nonlinear optical processes [22].

The problem is that the realization of such nonlinear interaction at the single photon level is challenging. The issue becomes clear if one is familiar with the advent of nonlinear optics. As presented briefly in chapter 3, looking at the polarization expansion $\mathbf{P}_i = \mathbf{P}_i^{(0)} + \chi^{(1)}\mathbf{E}_j +$

$\chi^{(2)}\mathbf{E}_j\mathbf{E}_l + \chi^{(3)}\mathbf{E}_j\mathbf{E}_k\mathbf{E}_l + \cdots$ we see that at low optical powers, the materials exhibit only the linear term, and therefore the conventional linear optics. It is only for intense fields that the higher orders also become relevant. Therefore, it is not obvious that strong nonlinear interactions should be easily seen at the level of single photons.

However, a few proposals have been made and implemented during the last years [22, 11]. We could mention:

- The optical Kerr effect in which it is possible to use one field to shift the phase of a second one in a third-order ($\chi^{(3)}$) process. However, since its proposal [23] no experimental implementation was demonstrated.
- Rydberg-blockades have been shown to be an interesting approach to enable two-photon interactions [24]. The basic idea is to combine the EIT effect with the energy-level shifts that suppress excitation of nearby atoms. As in a regular EIT process a weak probe field and a control field induce transparency in an opaque medium. The two fields are coupled in a Λ system. However, if a third field coupled with another excited state (Rydberg state) is used, it is possible to destroy the quantum interference associated with EIT by an amount that depends on the intensity of this new field. Therefore, the probe field can interact with this third field [22, 11]. Since Rydberg excitation blockade hinders the simultaneous excitation of another Rydberg atom inside the blockade radius, this enhances the absorption probability of two photons close in time giving rise to a quantum nonlinearity.

1.3 Quantum memory using higher nonlinear orders

Here we propose to use higher orders of nonlinear interactions, namely $\chi^{(5)}$ and $\chi^{(7)}$, for fundamental studies in quantum optics and applications in quantum information. From the fundamental side, since most of the research in quantum optics uses $\chi^{(2)}$ and $\chi^{(3)}$ processes, these higher-orders can be used to create new states of light. For quantum information applications we propose new quantum memories that can integrate a few of the desired properties for a quantum memory inside a single process. For instance, we show in reference [25] that with the $\chi^{(5)}$ and $\chi^{(7)}$ processes it is possible to combine storage and processing abilities (section 5.11) in a single process. This could prove to be useful for quantum information processing in general, especially in the context of quantum networks.

A quantum memory may be explained in more details as follows. The write process creates coherence and population gratings associated with high-order nonlinear processes, which can be selectively retrieved by a reading beam after a controllable storage time. Each kind of grating can store only specific orders of the nonlinear interaction, leading to special features in each signal [26]. When we add orbital angular momentum (OAM) in the write fields, each atom of the ensemble will accumulate a different amount of OAM from the applied laser beams for each nonlinear process. As a result the new field generated at the read process can have a different charge from the original ones. More than that, the specific spatial configuration chosen for the experiment allows to decide which nonlinear order to be accessed, permitting to select the output charge.

Moreover, in order to obtain any realistic quantum network, one must connect several nodes distributed along the network. This would benefit from multipartite entanglement and the generation of multiphoton quantum correlations. Even though there have been recently an advance in multipartite entanglement in several systems like OPO [27, 28] and multiplexed light modes in the time domain [29], most of the theoretical and experimental proposals made so far are mostly between pairs of nodes [30, 31, 32, 33, 34]. A generalization of theses schemes are fundamental for scalability. Because such higher-order nonlinearities are associated with processes involving a larger number of photons, our scheme can in principle be used to generate multiple quantum-correlated photons, opening the possibility to extend the capability of many quantum information protocols.

We propose a concrete method to generate triplets of correlated photons (chapter 7). The idea is similar to the one proposed in the DLCZ protocol. First the ensemble is prepared in a pure state with all atoms in the same ground-state $|g\rangle$. After that, a write pulse excites just one atom of the ensemble to the excited state creating a small probability to transfer this atom to another ground-state $|s\rangle$ with the simultaneous emission of a photon that we call *photon 1*. A second write field transfers this atom back to $|g\rangle$ with the simultaneous emission of the *photon 2*. Finally, a read field in a mode that fulfills the phase-matching condition, together with the emission of the *photon 3* in the phased-matched direction, closes the $\chi^{(5)}$ process. The correlations among the photons are related to the fact that one is acting over and over on the same atom of the ensemble. It is possible to see this process also as a multiwave-mixing spaced in time in one atom. This idea can be expanded for more photons.

Finally, in the context of applications for classical communications using OAM, we demonstrate in chapter 6 that a LG mode can be amplified through a nonlinear stimulated Raman process [35]. This is important to reverse propagation losses in the signal, especially for long distances.

1.4 Thesis structure

This thesis is organized as follows. We begin explaining the basic concepts that are used throughout the text. Chapter 2 describes briefly the essential concepts behind laser cooling and trapping of neutral atoms and the operation of a Magneto-Optical Trap (MOT), the system used for the experiments. Chapter 3 contains useful concepts of nonlinear optics and the basic nonlinear process that we used to build our memory. In chapter 4 we discuss the OAM of light used in two different realizations. In one of them we use OAM to demonstrate the capacity of the memory to manipulate the stored information. The second part of the thesis, going from chapter 5 to chapter 6, presents the experimental and theoretical results. In chapter 5 we theoretical and experimentally investigate a nonlinear atomic memory in the semi-classical regime. In chapter 6 we discuss a Raman gain used in the amplification of light carrying OAM. Finally, in chapter 7 we discuss the nonlinear atomic memory in the single-photon regime.

PART I

Basic Concepts

Chapter 2

Laser cooling and trapping

2.1 Introduction

Here we will describe briefly the essential concepts behind the operation of a Magneto-Optical Trap (MOT). We start describing the mechanical effects of light on atoms, namely the dipole force and the radiation pressure. Then we describe how to use the second force to cool and trap atoms. Finally, we calculate the minimum temperature achievable by Doppler cooling. We will follow the standard treatment given in many textbooks [36, 37, 38, 39, 40, 41, 42].

2.2 Force on two-level atoms

There are essentially two types of mechanical forces that light can exert on atoms, which are associated with the dispersive and the absorptive properties of the interaction. The first one is a conservative force called the dipole force associated to the potential energy of the dipole induced by the presence of the electric field. The second is a nonconservative force called radiation pressure related to absorption and re-emission of photons from the incident field.

2.2.1 Derivation of the forces

If one considers the atom as being infinitely heavy and at rest only the internal degrees of freedom are important. However, to describe the mechanical effects of light on atoms we need to consider the external degrees of freedom as well. The Hamiltonian for an atom in the presence of an external electrical field E is

$$H = \frac{\mathbf{P}^2}{2M} + H_A - \mathbf{d}\cdot\mathbf{E} \tag{2.1}$$

where H_A is the Hamiltonian of the free atom and $\mathbf{d}$, $\mathbf{P}$, and M are the electric dipole moment, the momentum, and the mass of the atom. In classical mechanics the force is given by the equation

$$\mathbf{F} = \frac{d\mathbf{P}}{dt}\,. \tag{2.2}$$

A quantum version of Newton's laws can be found using the Ehrenfest theorem, which states that the expectation value of a quantum mechanical operator must be equivalent to the behavior

of the same classical quantity. Then, using the Heisenberg equations for $\mathbf{P}$

$$\begin{aligned}\frac{d}{dt}\langle \mathbf{P}\rangle &= \frac{i}{\hbar}\left\langle \overbrace{[H,\mathbf{P}]}^{i\hbar\frac{\partial H}{\partial \mathbf{R}}}\right\rangle \\ &= -\frac{\partial H}{\partial \mathbf{R}}\end{aligned} \tag{2.3}$$

where we used that the operator $\mathbf{P} = -i\hbar\nabla$ and $\mathbf{R}$ is the position of the center of mass. Then using Eq.(2.3) and Eq.(2.1), we find

$$\frac{d}{dt}\langle \mathbf{P}\rangle = \sum_{i=x,y,z}\langle d_i \nabla_R E_i(\mathbf{R},t)\rangle \tag{2.4}$$

If we consider $\mathbf{r}_c = \langle R\rangle$ as the center of the atom

$$M\frac{d^2}{dt^2}\langle \mathbf{r_c}\rangle = \sum_{i=x,y,z}\langle d_i \nabla_R E_i(\mathbf{r_c},t)\rangle \tag{2.5}$$

We make two assumptions to solve the right-hand side of Eq.(2.5). In the first we consider that the de Broglie wavelength of the atom, $\lambda_B = h/Mv$, is frequently much smaller than the wavelength λ of the incident optical field, which determines the rate of spatial variations of the electric field. Thus, the electric field does not vary significantly in the region where the atom is localized and it can be considered constant. Hence one can write

$$\langle d_i \nabla_R E_i(\mathbf{r_c},t)\rangle = \langle d_i\rangle \nabla_R E_i(\mathbf{r_c},t) \tag{2.6}$$

The second assumption is that the internal and external degrees of freedom evolve in different time scales. More specifically, the internal degrees of freedom evolve over time T_{int} scales on the order of the excited state lifetime Γ^{-1}, while the external degrees of freedom evolve over time T_{ext} scales on the order of $\hbar/E_{recoil}$, where E_{rec} is the recoil energy that an atom gains when it absorbs a photon. In general $\Gamma^{-1} \ll \hbar/E_{recoil}$ (for sodium $T_{ext} \approx 400T_{int}$ [40]). This implies that for an appreciable change in the external degrees of freedom [in this case, in r_c on the left-hand side of Eq.(2.5)], the internal degrees of freedom [in this case in the dipole moment $\langle d\rangle$ on the right-hand side of Eq.(2.5)] would have already reached the steady-state. Therefore, we can use the steady-state solution for $\langle d\rangle$ calculated using Bloch equations or in the Bloch-vector formalism [40]

$$\begin{aligned}\langle d\rangle &= 2(d_{12})\left[\sigma_{12}e^{i\omega t} + \sigma_{21}e^{-i\omega t}\right] \\ &= 2(d_{12})\left[u\cos(\omega t) - v\sin(\omega t)\right]\ ,\end{aligned} \tag{2.7}$$

where $u = \sigma_{12} + \sigma_{21}$ and $v = -i(\sigma_{12} - \sigma_{21})$. We consider the electric field to be of the form

$$E(\mathbf{r},t) = \mathbf{e}_{rad}E_0(\mathbf{r})\cos\left[\omega t + \phi(\boldsymbol{r})\right]\ , \tag{2.8}$$

where $E_0(\mathbf{r})$ and $\phi(\mathbf{r})$ are the amplitude and phase, respectively. We assume that the polarization vector $\mathbf{e}_{rad}$ does not depend on the position. The time origin can always be chosen so that $\phi(\mathbf{0}) = 0$. Hence

$$\nabla E(\mathbf{0},t) = \mathbf{e}_{rad}\left[\cos(\omega t)\nabla E_0(\mathbf{0}) - E_0(\mathbf{0})\sin(\omega t)\nabla\phi(\mathbf{0})\right] . \tag{2.9}$$

Substituting Eqs.(2.9) in Eq.(2.5), and taking the average in time we find

$$\begin{aligned} F &= M\frac{d^2}{dt^2}\langle\mathbf{r_c}\rangle \\ &= \sum_{i=x,y,z}(d_{12})_i(e_{rad})_i\left[u\nabla E_0(\mathbf{0}) + vE_0(\mathbf{0})\nabla\phi(\mathbf{0})\right] \\ &= \mathbf{d}_{12}\cdot\mathbf{e}_{rad}\left[u\nabla E_0(\mathbf{0}) + vE_0(\mathbf{0})\nabla\phi(\mathbf{0})\right] , \end{aligned} \tag{2.10}$$

There are two contributions in Eq.(2.10). The first is the radiation pressure

$$F_{rad} = \mathbf{d}_{12}\cdot\mathbf{e}_{rad}vE_0(\mathbf{0})\nabla\phi(\mathbf{0}) , \tag{2.11}$$

and the second is the dipole force

$$F_{dip} = \mathbf{d}_{12}\cdot\mathbf{e}_{rad}u\nabla E_0(\mathbf{0}) . \tag{2.12}$$

It is convenient to rewrite them in terms of the Rabi frequency

$$\Omega = -\mathbf{d}_{12}\cdot\mathbf{e}_{rad}\frac{E_0}{\hbar} . \tag{2.13}$$

Then

$$F_{dip} = -\hbar u\nabla\Omega , \tag{2.14a}$$

$$F_{rad} = -\hbar v\Omega\nabla\phi(\mathbf{0}) . \tag{2.14b}$$

Note that if the electric field amplitude has a null gradient, F_{dip} vanishes. On the other hand, if the electric field phase has a null gradient, F_{rad} vanishes. In the next sections we will focus on F_{rad}, since only this term is relevant to this thesis.

2.2.2 Radiation pressure

Now we will examine in detail the term in (2.11) which is a force due to absorption and reemission of the incident light. Since it is not possible to reverse the spontaneous emission, the action of the force is not a reversible process, leading to the conclusion that this is a dissipative force.

As pointed before, F_{rad} does not vanish for a null gradient of the electric field amplitude. Therefore, we consider a plane wave with a constant amplitude as our electric field to simplify our calculations. Then,

$$E(\mathbf{r},t) = \mathbf{e}_{rad}E_0(\mathbf{r})\cos\left[\omega t - \boldsymbol{k}\cdot\mathbf{r}\right] \tag{2.15}$$

with a constant amplitude $E_0(\mathbf{r}) = E_0$ and phase $\phi(\mathbf{r}) = -\mathbf{k}\cdot\mathbf{r}$. Then

$$\nabla\phi(\mathbf{r}) = -\mathbf{k} \tag{2.16}$$

and

$$F_{rad} = v\Omega\hbar\mathbf{k}\ . \tag{2.17}$$

In the steady-state (see [40])

$$v\Omega = \Gamma\rho_{22}\ . \tag{2.18}$$

Then

$$F_{rad} = \Gamma\rho_{22}\hbar\mathbf{k}\ . \tag{2.19}$$

Since $\Gamma\rho_{22}$ is the rate of photons emitted spontaneously, we conclude from (2.19) that the rate of change of momentum (an thus the force F_{rad}) is equal to the photon momentum $\hbar\mathbf{k}$ times the number of photons spontaneously emitted per unit time.

However, in the steady-state the number of photons absorbed per unit time $\frac{dN_{ph}}{dt}$ is equal to the number of photons emitted spontaneously per unit time (see [40]). Thus we have

$$F_{rad} = \hbar\mathbf{k}\left\langle\frac{dN_{ph}}{dt}\right\rangle\ . \tag{2.20}$$

The interpretation of Eq.(2.20) is clear. The rate of momentum transfer to the atom, i.e. the force acting on it, should be due to absorption, spontaneous emission, and stimulated emission. Absorption of a photon leads to the transfer of its momentum $\hbar k$ from the optical field to the atom. Stimulated emission of a photon leads to the transfer of momentum $\hbar k$ from the atom back to the incident beam in the same direction. Spontaneous emission also leads to a loss of momentum $\hbar k$ from the atom, but the photon is emitted in random directions. Since the recoil associated with the spontaneous emission is in a random direction, its average over many emission events results in a zero net effect on the atomic momentum. However, the recoil associated with the absorption is always in the same direction. Thus the average momentum gained by the atom is $\hbar k$ times the mean number of photons absorbed. If only absorption and stimulated emission were present, the atom would absorb and emit in the same direction, resulting in a zero net force. It is the spontaneous emission that breaks this symmetry, making the difference between absorption and stimulated emission be nonzero, allowing a net transfer of momentum to the atoms. If the incident beam is weak, stimulated emission can be neglected and the force will be basically due to absorption as in Eq.(2.20).

If the beam is strong, the radiative force saturates. By replacing the expression of ρ_{22} (see [40]) in the steady-state in Eq.(2.19) we find

$$F_{rad} = \hbar\mathbf{k}\Gamma\frac{\left(\frac{\Omega}{2}\right)^2}{\delta^2 + (\frac{\Gamma}{2})^2 + \frac{\Omega^2}{2}}\ . \tag{2.21}$$

Increasing the intensity does not increase the force indefinitely but it saturates to a maximum value of $\hbar k\Gamma/2$, because ρ_{22} has a maximum value of $1/2$. The physical explanation is quite intuitive. Even though the increase of the intensity would increase the rate of absorption, and consequently the transfer of momentum from the field to the atom, it would also increase the rate of stimulated emission, for which the transfer of momentum is opposite in direction compared to the absorption, compensating the total momentum transfer.

2.3 Optical Molasses

In section 2.2.2 we presented a discussion of the radiation pressure on the atoms exerted by a single laser beam. In this section we extend the previous treatment to the case of two counter-propagating beams with same frequency, intensity and polarization interacting with the atom. We label the laser propagating in the same direction of the atom as $-$, since the Doppler effect decreases its frequency, and the other one as $+$. We also define the positive direction of the axis in the direction of the beam $-$. The total force is then[1]

$$\begin{aligned}
F_{tot} &= F_- + F_+ \\
&= F_{rad}(\omega - \omega_0 - kv) - F_{rad}(\omega - \omega_0 + kv) \\
&= \hbar k\Gamma \frac{\left(\frac{\Omega}{2}\right)^2}{(\omega - \omega_0 - kv)^2 + (\frac{\Gamma}{2})^2 + \frac{\Omega^2}{2}} + \hbar(-k)\Gamma \frac{\left(\frac{\Omega}{2}\right)^2}{(\omega - \omega_0 + kv)^2 + (\frac{\Gamma}{2})^2 + \frac{\Omega^2}{2}} \\
&= \hbar k\Gamma \left[\frac{\left(\frac{\Omega}{2}\right)^2}{(\omega - \omega_0 - kv)^2 + (\frac{\Gamma}{2})^2 + \frac{\Omega^2}{2}} - \frac{\left(\frac{\Omega}{2}\right)^2}{(\omega - \omega_0 + kv)^2 + (\frac{\Gamma}{2})^2 + \frac{\Omega^2}{2}} \right] .
\end{aligned} \tag{2.22}$$

Defining $\delta = \omega - \omega_0$ and $x = kv$, and assuming low velocities, $kv \ll \Gamma$, we can expand

$$f_\pm(x) = \frac{1}{(\delta \pm x)^2 + (\frac{\Gamma}{2})^2 + \frac{\Omega^2}{2}} \approx f_\pm(0) + \frac{df_\pm(x)}{dx}\Big|_{x=0} x = \left[\frac{1}{\delta^2 + (\frac{\Gamma}{2})^2} \mp \frac{2\delta}{\left[\delta^2 + (\frac{\Gamma}{2})^2\right]^2} x \right] . \tag{2.23}$$

Then

$$\begin{aligned}
F_{tot} &= F_- + F_+ \\
&= \hbar k\Gamma (\frac{\Omega}{2})^2 \left\{ \left[\frac{1}{\delta^2 + (\frac{\Gamma}{2})^2} + \frac{2\delta}{\left[\delta^2 + (\frac{\Gamma}{2})^2\right]^2} x \right] - \left[\frac{1}{\delta^2 + (\frac{\Gamma}{2})^2} - \frac{2\delta}{\left[\delta^2 + (\frac{\Gamma}{2})^2\right]^2} x \right] \right\} \\
&= 4\hbar k \underbrace{2\left(\frac{\Omega}{\Gamma}\right)^2}_{\frac{I}{I_s}} \frac{\frac{2\delta}{\Gamma}}{\left[1 + (\frac{2\delta}{\Gamma})^2\right]^2} kv \\
&= 4\hbar k^2 \frac{I}{I_s} \frac{\frac{2\delta}{\Gamma}}{\left[1 + (\frac{2\delta}{\Gamma})^2\right]^2} v \\
&= -\alpha v ,
\end{aligned} \tag{2.24}$$

where $I = |E_0|^2$ and $I_s = \frac{\pi hc\Gamma}{3\lambda^3}$ are the intensity and saturation intensity, respectively, and

$$\alpha = -4\hbar k^2 \frac{I}{I_s} \frac{\frac{2\delta}{\Gamma}}{\left[1 + (\frac{2\delta}{\Gamma})^2\right]^2} , \tag{2.25}$$

[1] Here in this section we consider v as the velocity and not the Bloch component like in section 2.2.2

is the damping coefficient. Observe that Eq. 2.24 has the form of a viscous force. Therefore, in the case of the radiation force, the light exerts a frictional force just like a particle in a viscous fluid. This is the reason why the technique to cool atoms using this force is known in the literature as optical molasses.

Note also that the force in Eq. 2.24 opposes the velocity for $\delta < 0$ and therefore damps the movement. For $\delta > 0$ the force is positive and therefore increases the velocity. Thus, cooling requires red frequency detuning.

With the above results we can calculate the rate of change of the kinetic energy. This would give a quantitative result for the rate of the cooling process that will also be useful to calculate the Doppler limit in section 2.5:

$$\frac{d}{dt}\left(\frac{1}{2}mv^2\right) = mv\frac{dv}{dt} = vF_{tot} = -\alpha v^2 \,. \tag{2.26}$$

2.4 The magneto-optical trap (MOT)

The optical molasses technique can only cool the atoms, but does not trap them. However, if the counter-propagating laser beams (two for each axis) have opposite circular polarization, this configuration can be turned into a trap by the addition of a magnetic field gradient, as illustrated in Fig.2.1. Two coils with currents in opposite directions produce a quadrupole magnetic field that vanishes at the origin. Consider a simple $J = 0$ and $J = 1$ transition to illustrate the principle of the MOT. Close to the origin, where the magnetic field $B = 0$, there is a uniform field gradient that produces a Zeeman shift in the three sub-levels (with $M_J = 0, \pm 1$) of the $J = 1$ level (the $J = 0$ remains unperturbed). The shift in the z direction is

$$\delta E = g_J \mu_B \frac{dB}{dz} M_J z = \beta z \,, \tag{2.27}$$

which varies linearly with the atom's position (see Fig.2.1). For $z > 0$ the sub-level $M_J = -1$ has its energy lowered and the sub-level $M_J = +1$ has its energy raised, while for $z < 0$ we have the opposite (see Fig.2.1). Therefore, since all the beams frequencies are below the resonance (considering an atom at rest), if the atom is moving in the $z > 0$ direction it will absorb more photons from the σ^- beam, since it is closer to the resonance. This causes an imbalance in the radiation force, creating a net force that pushes the atom back towards the trap center. A similar process occurs for $z < 0$ but with the σ^+ interacting more strongly with the atoms (see Fig.2.1).

We can analyze this process mathematically by including the Zeeman shift in Eq.(2.22).

$$\begin{aligned} F_{MOT} &= F_{\sigma^+} + F_{\sigma_-} \\ &= F_{rad}(\omega - \omega_0 - kv - \beta z) - F_{rad}(\omega - \omega_0 + kv + \beta z) \\ &= -\alpha v - \frac{\alpha\beta}{k} z \,. \end{aligned} \tag{2.28}$$

The Eq.(2.28) shows that the imbalance in the radiation force caused by the Zeeman effect leads to a restoring force similar to a spring Kz, with the elastic constant $K = \frac{\alpha\beta}{k}$.

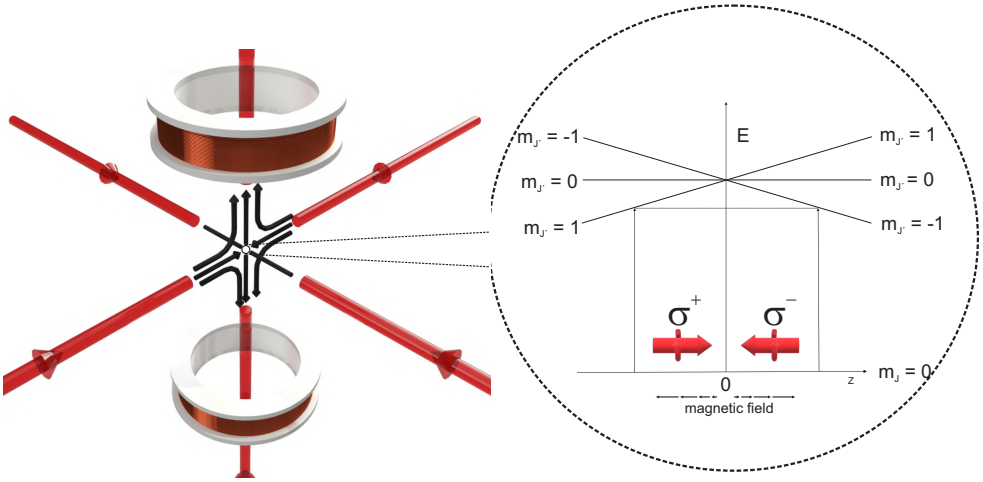

Figure 2.1 The schematic setup of a three dimensional magneto-optical trap. Three counter-propagating laser fields with opposite circular polarizations cool down the atoms. A pair of coils in anti-Helmholtz configuration creates a magnetic field (whose direction is represented by the arrows at the center) that vanishes at the center and increases linearly as one moves away from it. The figure on the right side shows the idea of a magneto-optical trap for an atom with a transition $J = 0 \rightarrow J = 1$. The inhomogeneous magnetic field shifts the Zeeman degeneracy of the upper state inducing the atom to absorb more photons to the counter-propagating field due to the selection rules. For $z > 0$ the sub-level $M_J = -1$ has its energy lowered and the sub-level $M_J = +1$ has its energy raised, making the $M_J = 0 \rightarrow M_J = -1$ transition resonant and more probable. For $z < 0$ we have the opposite. As a consequence a net force appears pushing the atom back towards the trap center.

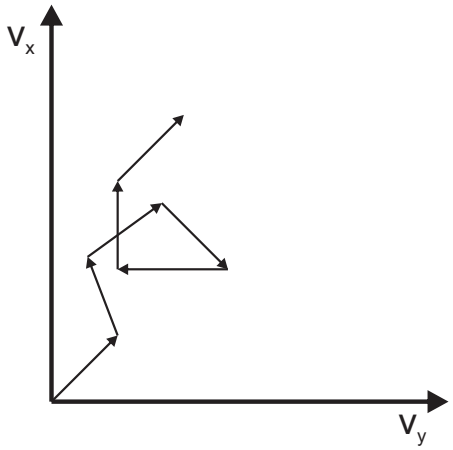

Figure 2.2 The recoil of an atom from each absorption and spontaneous emission causes the atomic velocity to change by the recoil velocity v_r in a random direction. Thus the atom undergoes a random walk in velocity space with steps of length v_r.

2.5 The Doppler cooling limit

Our treatment so far makes it appear as though the atom may be completely stopped by the cooling force. This is not the case. This apparent discrepancy appears because we have only considered the average cooling force. Physically, this force results from many absorption and spontaneous emission cycles, which are accompanied by fluctuations in both processes. These are responsible for a diffusion of the atomic momentum. These diffusion mechanisms in the velocity space are responsible for a heating of the translational degrees of freedom.

The spontaneous emission that always accompanies the cooling force causes the atom to recoil in random directions. Each of these recoils leads to a random walk of the velocity (see Fig.2.2). We remember that in a random walk all the steps are statistically independent, and the probability distribution is characterized by a zero mean $\langle v \rangle = 0$ but with a non-vanishing root-mean-squared $\sqrt{N}l$, where l is the step length, or a variance Nl^2.

In our case a step will occur whenever a photon is absorbed or emitted, and the length of each step is the photon momentum $\hbar k$. Since scattering means absorption followed by emission it represents effectively two steps in a random walk in the velocity space with size $\hbar k/m$, where m is the mass of the atom (see Fig.2.2).

Thus, for an atom initially at rest, after one step we can write the mean squared velocity as

$$\left\langle v^2 \right\rangle_{recoil} = \left(\frac{\hbar k}{m}\right)^2 . \tag{2.29}$$

Since the scattering occurs at a rate R_{scatt}, after a time t the atom scattered a number of photons $N = R_{scatt}t$. Then, the mean squared velocity increased as

$$\left\langle v^2 \right\rangle = N\left(\frac{\hbar k}{m}\right)^2 = R_{scatt}t2\left(\frac{\hbar k}{m}\right)^2 . \tag{2.30}$$

The factor 2 takes into account the fact that a scattering is a two step process as mentioned above. Thus the heating rate is

$$\frac{d}{dt}\left\langle v^2\right\rangle_{heat} = 2R_{scatt}\left(\frac{\hbar k}{m}\right)^2 , \tag{2.31}$$

where the scattering rate for six beams is

$$R_{scatt} = \frac{6I}{I_{sat}}\frac{\left(\frac{\Gamma}{2}\right)^3}{\Delta^2+\left(\frac{\Gamma}{2}\right)^2} . \tag{2.32}$$

Including the heating and the cooling rate into the same equation, we find that

$$\begin{aligned}\frac{d}{dt}\left\langle v^2\right\rangle &= \frac{d}{dt}\left\langle v^2\right\rangle_{heat} + \frac{d}{dt}\left\langle v^2\right\rangle_{cool} \\ &= 2R_{scatt}\left(\frac{\hbar k}{m}\right)^2 - \alpha\left\langle v^2\right\rangle .\end{aligned} \tag{2.33}$$

In the steady state $\frac{d}{dt}\left\langle v^2\right\rangle = 0$, and

$$\begin{aligned}\left\langle v^2\right\rangle &= \frac{2R_{scatt}}{\alpha}\left(\frac{\hbar k}{m}\right)^2 \\ &= -\frac{3\hbar\Gamma}{4m}\frac{1+\left(\frac{2\Delta}{\Gamma}\right)^2}{\left(\frac{2\Delta}{\Gamma}\right)} .\end{aligned} \tag{2.34}$$

According to the equipartition theorem the kinetic energy is related to the temperature by

$$\frac{1}{2}m\left\langle v^2\right\rangle = \frac{3}{2}k_BT , \tag{2.35}$$

which gives

$$k_BT = -\frac{\hbar\Gamma}{4}\frac{1+\left(\frac{2\Delta}{\Gamma}\right)^2}{\left(\frac{2\Delta}{\Gamma}\right)} . \tag{2.36}$$

We can calculate the detuning that will give the lowest temperature by differentiating Eq.2.36 by Δ. We find that the temperature is minimized for $\Delta = -\frac{\Gamma}{2}$, which gives the Doppler temperature T_D

$$T_D = -\frac{\hbar\Gamma}{2k_B} . \tag{2.37}$$

It is possible to achieve temperatures below the Doppler limit. The existence of a Zeeman structure in the alkalis allows the appearence of new processes. One of the most remarkable ones is the Sisyphus effect [43]. A detailed description of these effects can be found in the literature [36, 37, 38, 39, 40, 41, 42].

Chapter 3

Nonlinear optics

In this chapter we introduce a few concepts of nonlinear optics that are useful for understanding the experiments presented later, such as the polarization expansion (section 3.1), the wave equation for nonlinear interaction (section 3.3), and the phase-matching condition (section 3.4). We also introduce in section 3.5 the method to systematically discriminate a specific higher-order susceptibility that we used later as an inspiration to develop the atomic memory using higher-order nonlinearities.

3.1 Polarization expansion

It's well known from classical electrodynamics that the polarization $\vec{P}(t)$ of a material depends upon the strength of the applied electric field $\vec{E}(t)$ [44, 45]. Moreover, the polarization can be described by a Taylor series in powers of the field strength. For the ith cartesian component of the polarization we have

$$\begin{aligned} P_i &= P_i^{(0)} + \sum_j \left(\frac{\partial P_i}{\partial E_j}\right) E_j + \frac{1}{2!}\sum_{jk}\left(\frac{\partial P_i}{\partial E_j \partial E_k}\right) E_j E_k + \frac{1}{3!}\sum_{jkl}\left(\frac{\partial P_i}{\partial E_j \partial E_k \partial E_l}\right) E_j E_k E_l + \cdots \\ &= P_i^{(0)} + \chi^{(1)} E_j + \chi^{(2)} E_j E_l + \chi^{(3)} E_j E_k E_l + \cdots . \end{aligned} \tag{3.1}$$

In most cases the material doesn't have a permanent dipole moment making the $P_i^{(0)}$ term zero, leaving any dipole moment to be induced by the external field. The terms $\chi^{(1)}$, $\chi^{(2)}$, and $\chi^{(3)}$ are known as first, second, and third order susceptibilities, respectively. In the low-intensity regime only the first term is relevant and the induced polarization depends only linearly with the field $\vec{E}(t)$. This case is the conventional linear optics. However, for intense fields the higher orders also become relevant, and besides the linear term one starts to see that the material's response also depends on the second, third, and other powers of the electric field. By strong fields we mean that the lowest order correction, $\chi^{(2)}\vec{E}(t)\vec{E}(t)$, should be comparable with the first one $\chi^{(1)}\vec{E}(t)$, i.e., when the applied electric field is comparable with the internal electric field $E = e/a_0^2$ where a_0 is the Bohr radius, but obviously not strong enough to ionize the atom. Typically, only laser light is sufficiently intense to provide these nonlinear responses of the material.

As one can see from Eq. 3.1 the susceptibilities $\chi^{(i)}$ are tensors. More specifically, $\chi^{(1)}$ is a second-rank tensor, $\chi^{(2)}$ is a third-rank tensor, and so on. In addition, for an isotropic

medium $\chi^{(1)}_{jk} = \chi^{(1)}_{kj}$, i.e, the tensor is diagonal. Moreover, because of the vectorial nature of $\vec{E}$ and $\vec{P}$, they are odd under inversion symmetry. These two statements imply that $\chi^{(2n)}$, with $n = 1,2,3,...$, vanishes for a medium with inversion symmetry. This is the case for a cloud of cold atoms, the atomic system used here. Therefore, we will only consider odd terms in the susceptibilities[1]

$$P_i = \varepsilon_0 \chi^{(1)} E_j + \chi^{(3)} E_j E_k E_l + \chi^{(5)} E_j E_k E_l E_m E_n \cdots . \tag{3.2}$$

3.2 Nonlinear optical phenomena

The beginning of nonlinear optics is usually attributed to Franken in 1961, with the observation of second harmonic generation [48]. After that, plentiful nonlinear optical phenomena have been discovered and applied in many situations, such as sum-frequency generation, difference-frequency generation, multiwave mixing, self-focusing and self-defocusing, optical bistability, optical soliton, etc. [47, 49, 50]. Among these various processes we would like to highlight the multiwave mixing, which is directly related to the work presented in this thesis.

Before describing the multiwave mixing (MWM) process, we start by a simpler example: the four-wave mixing (FWM) in the sense that appears here in this thesis. Broadly speaking, FWM is the nonlinear optical process where three input fields interact through the third-order susceptibility [$\chi^{(3)}$] generating a fourth field. A similar idea holds for the six-wave mixing process (SWM). In this case, we have a fifth-order nonlinear process mediated by the the fifth-order susceptibility [$\chi^{(5)}$], where five fields interacts to produce a sixth field. The MWM is a generalization to the nth order of nonlinearity.

3.3 The wave equation for nonlinear interaction

We have shown previously how the nonlinear response of the medium to the incident fields can induce a polarization that can even develop new frequency components that were not present in the input radiation. This induced polarization acts as a source for a new electromagnetic field in Maxwell's equation. Here we show the standard mathematical tools used to describe and quantify most of the nonlinear processes found in classic textbooks [47, 51, 50].

An electromagnetic wave propagating in the medium obeys the Maxwell equations:

$$\nabla \cdot \boldsymbol{D} = \rho \, , \tag{3.3a}$$

$$\nabla \cdot \boldsymbol{B} = 0 \, , \tag{3.3b}$$

$$\nabla \times \boldsymbol{H} = \frac{\partial \boldsymbol{D}}{\partial t} + \boldsymbol{J} \, , \tag{3.3c}$$

[1] A short comment should be made here for completeness. After a substantial advance in the laser industry, we have today lasers with very high intensities and very short pulse durations, that makes the assumptions for traditional nonlinear optics no longer applicable. It is possible to find in the literature unexpected $\chi^{(2)}$ effects in inversion symmetric materials [46]. Also this rule for centrosymmetric materials holds in the electric-dipole approximation. For other multipole processes the second-order susceptibility may not vanish [47].

$$\nabla \times \boldsymbol{E} = -\frac{\partial \boldsymbol{B}}{\partial t} \,. \tag{3.3d}$$

with the constitutive relations

$$\boldsymbol{D} = \varepsilon_0 \boldsymbol{E} + \boldsymbol{P} \,, \tag{3.4a}$$
$$\boldsymbol{B} = \mu_0 \left(\boldsymbol{H} + \boldsymbol{M}\right) \,, \tag{3.4b}$$
$$\boldsymbol{J} = \sigma \boldsymbol{E} \,. \tag{3.4c}$$

where **E** and **H** are the electric and magnetic field strengths, respectively; **D** and **B** are the electric induction and magnetic displacement, respectively; **P** and **M** are the electric and magnetic polarization, respectively; **J** and σ are the current and charge density, respectively. We consider here only media with $\mathbf{M} = 0$ and $\mathbf{J} = 0$. One can separate the linear from the nonlinear part of the polarization leading to the expression

$$\boldsymbol{P} = \varepsilon_0 \chi^{(1)} \boldsymbol{E} + \boldsymbol{P}_{NL} \tag{3.5}$$

Then we obtain

$$\begin{aligned} \boldsymbol{D} &= \varepsilon_0 \boldsymbol{E} + \varepsilon_0 \chi^{(1)} \boldsymbol{E} + \boldsymbol{P}_{NL} \\ &= \varepsilon \boldsymbol{E} + \boldsymbol{P}_{NL} \end{aligned} \tag{3.6}$$

where $\varepsilon = \varepsilon_0 \left(1 + \chi^{(1)}\right)$ is the linear dielectric coefficient. Finally, the Maxwell equations can be simplified to

$$\nabla \times \boldsymbol{E} = -\frac{\partial \left(\mu_0 \boldsymbol{H}\right)}{\partial t} \,, \tag{3.7a}$$
$$\nabla \times \boldsymbol{H} = \frac{\partial}{\partial t} \left(\varepsilon \boldsymbol{E} + \boldsymbol{P}_{NL}\right) \,. \tag{3.7b}$$

If we apply $\nabla\times$ on both sides of Eq. (3.7a) and substitute Eq. (3.7b) into it, we find

$$\nabla \times \nabla \times \boldsymbol{E} + \mu_0 \varepsilon \frac{\partial^2 \boldsymbol{E}}{\partial t^2} = -\mu_0 \frac{\partial^2 \boldsymbol{P}_{NL}}{\partial t^2} \,. \tag{3.8}$$

or using $c = 1/\sqrt{\mu_0 \varepsilon_0}$

$$\nabla \times \nabla \times \boldsymbol{E} + \frac{1}{c^2} \frac{\varepsilon}{\varepsilon_0} \frac{\partial^2 \boldsymbol{E}}{\partial t^2} = -\frac{1}{\varepsilon_0 c^2} \frac{\partial^2 \boldsymbol{P}_{NL}}{\partial t^2} \,. \tag{3.9}$$

This is the wave equation for describing light propagation in the nonlinear medium. If $\boldsymbol{P}_{NL} = 0$ we have only terms on the left side, which is the ordinary wave equation in vacuum. The term on the right side is the polarization source term that we mentioned before. This is the nonlinear response of the medium.

We use the relation $\nabla \times \nabla \times \mathbf{E} = \nabla \left(\nabla \cdot \mathbf{E}\right) - \nabla^2 \mathbf{E}$. If we have an isotropic medium, $\nabla \cdot \mathbf{E} = 0$, and Eq. 3.9 reduces to

$$\nabla^2 \boldsymbol{E} - \frac{n^2}{c^2} \frac{\partial^2 \boldsymbol{E}}{\partial t^2} = \frac{1}{\varepsilon_0 c^2} \frac{\partial^2 \boldsymbol{P}_{NL}}{\partial t^2} \,, \tag{3.10}$$

where we neglect the tensor nature of χ considering ε a scalar quantity and used $n = \sqrt{\varepsilon/\varepsilon_0}$.

Now suppose we have a monochromatic plane wave propagating along the z direction such as

$$\boldsymbol{E}(\boldsymbol{r},t) = \boldsymbol{\mathcal{E}}(\boldsymbol{z},t)e^{i(kz-\omega t)}\,, \tag{3.11a}$$

$$\boldsymbol{P}_{NL}(\boldsymbol{r},t) = \boldsymbol{\mathcal{P}}_{NL}(\boldsymbol{z},t)e^{i(k'z-\omega t)}\,, \tag{3.11b}$$

where k and k' are the wave vectors of the laser and polarization fields, respectively. Substituting Eqs. (3.11a) and (3.11b) into 3.10, we find

$$\nabla^2\mathscr{E}(z,t) = \left[\left(\frac{\partial^2}{\partial z^2} + i2k\frac{\partial}{\partial z} - k^2\right)|\mathscr{E}(z,t)|\right]e^{i(kz-\omega t)}\,, \tag{3.12a}$$

$$\frac{\partial^2}{\partial t^2}\mathscr{E}(z,t) = \left[\left(\frac{\partial^2}{\partial t^2} + i2\omega\frac{\partial}{\partial t} - \omega^2\right)|\mathscr{E}(z,t)|\right]e^{i(kz-\omega t)}\,, \tag{3.12b}$$

$$\frac{\partial^2}{\partial t^2}P_{NL}(z,t) \approx -\omega^2\,|P_{NL}(z,t)|\,e^{i(k'z-\omega t)}\,. \tag{3.12c}$$

We now use the slowly varying field amplitude approximation

$$\left|\frac{\partial^2\mathscr{E}(z,t)}{\partial z^2}\right| \ll \left|k\frac{\partial\mathscr{E}(z,t)}{\partial z}\right|\,, \tag{3.13a}$$

$$\left|\frac{\partial^2\mathscr{E}(z,t)}{\partial t^2}\right| \ll \left|\omega\frac{\partial\mathscr{E}(z,t)}{\partial t}\right|\,, \tag{3.13b}$$

and the relations $v = c/n$ and $k = (\omega/c)n$ to find

$$\frac{\partial\mathscr{E}(z,t)}{\partial z} + \frac{1}{v}\frac{\partial\mathscr{E}(z,t)}{\partial t} = \frac{i\omega}{2\varepsilon_0 cn}\frac{\partial P_{NL}(z,t)}{\partial z}e^{i\Delta kz} \tag{3.14}$$

where $\Delta k = k' - k$ is the phase mismatch between the electric field and the nonlinear polarization.

3.4 Phase-matching condition

The phase mismatch introduced in the last section carries an important significance in nonlinear optics and in the experiments described in the following chapters. In this section we want to introduce the basic concept of the phase matching condition. We choose a three-wave mixing process as a simple example where it appears naturally.

Two incident monochromatic fields at different frequencies and with the same propagation direction interact in the nonlinear medium generating a third wave. The two input electrical fields can be expressed as

$$E_i(z,t) = \mathscr{E}_i(z)e^{i(k_i z-\omega_i t)} + c.c.\,, \tag{3.15}$$

where $i = 1,2$. These fields will induce a polarization $P_3(z,t)$ that will be the nonlinear source term of Eq. 3.14 and can be represented as

$$P_3(z,t) = \mathscr{P}_3 e^{i(k_3 z-\omega_3 t)} + c.c.\,, \tag{3.16}$$

where

$$\mathscr{P}_3 = \varepsilon_0 \chi^{(2)} \mathscr{E}_1 \mathscr{E}_2 \, . \tag{3.17}$$

Therefore, using the nonlinear wave equation (Eq. 3.14) derived in the previous section, after the slowly varying amplitude approximation, one ends up with the following equation for the third field [47, 51]

$$\frac{d\mathscr{E}_3}{dz} = \frac{2id_{eff}\omega_3^2}{k_3 c^2} \mathscr{E}_1 \mathscr{E}_2 e^{i\Delta k z} \, , \tag{3.18}$$

where $\Delta k = k_1 + k_2 - k_3$ and $\chi^{(2)} = d_{eff}$. For simplicity, it is assumed that the power lost by the input fields $\mathscr{E}_1$ and $\mathscr{E}_2$ is negligible, i.e. the conversion of the input fields into the generated field is not too large, and we can consider $\mathscr{E}_1$ and $\mathscr{E}_2$ as constants. Then, we can just integrate Eq. 3.18 in z to find

$$\begin{aligned} \mathscr{E}_3 &= \frac{2id_{eff}\omega_3^2}{k_3 c^2} \mathscr{E}_1 \mathscr{E}_2 \int_0^L e^{i\Delta k z} dz \\ &= \frac{2id_{eff}\omega_3^2}{k_3 c^2} \mathscr{E}_1 \mathscr{E}_2 \left[\frac{e^{i\Delta k L} - 1}{i\Delta k} \right] \, . \end{aligned} \tag{3.19}$$

The intensity of the field $\mathscr{E}_3$ is given by the time-averaged Poynting vector,

$$I_3 = 2n_3 \varepsilon_0 c |\mathscr{E}_3|^2 \, . \tag{3.20}$$

Then

$$\begin{aligned} I_3 &= \left| \frac{2id_{eff}\omega_3^2}{k_3 c^2} \mathscr{E}_1 \mathscr{E}_2 \right|^2 \left| \frac{e^{i\Delta k L} - 1}{i\Delta k} \right|^2 \\ &= AI_1 I_2 \overbrace{\left| e^{i\frac{\Delta k L}{2}} \right|^2}^{=1} \left| \frac{e^{i\frac{\Delta k L}{2}} - e^{-i\frac{\Delta k L}{2}}}{i\Delta k} \right|^2 \\ &= AI_1 I_2 L^2 \frac{2sin^2\left(\frac{\Delta k L}{2}\right)}{(\Delta k L^2)^2} \\ &= AI_1 I_2 L^2 \frac{sin^2\left(\frac{\Delta k L}{2}\right)}{\left(\frac{\Delta k L^2}{2}\right)^2} \\ &= AI_1 I_2 L^2 sinc^2\left(\frac{\Delta k L}{2}\right) \, , \end{aligned} \tag{3.21}$$

where A is a constant that absorbed all the other constants that appeared in front of I_1 and I_2. From Eq.3.21 we note first that, in second-harmonic generation, the field is proportional to the intensities I_1 and I_2 of the input fields, and second that all phase mismatch is in $sinc^2\left(\frac{\Delta k L}{2}\right)$. This phase-mismatch factor is plotted in Fig.3.1 and shows that the process efficiency decreases with $\Delta k L$. The explanation is that as L increases and becomes greater than $1/\Delta k$, the generated wave gets out of phase with the polarization, and the energy flows back to the input waves

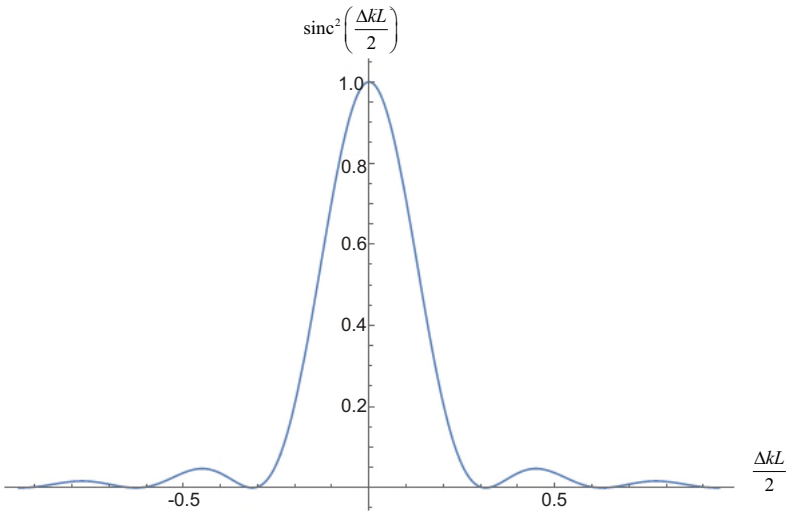

Figure 3.1 Plot of the function $sinc^2(\frac{\Delta kL}{2})$ that defines the amplitude variation of the generated signal in the phase-matching direction.

[47]. We also see from Fig.3.1 that the highest efficiency is at $\Delta k = 0$ which is the perfect phase-matching condition.

The physical interpretation for this is the following. If one sees each atom of the material as an individual oscillating dipole, when this phase matching condition is perfectly fulfilled, all the dipoles oscillates in phase so that the field emitted by each dipole adds coherently in the phase matching condition direction. Therefore, the total intensity emitted by this ensemble of dipoles scales as the square of the number of atoms participating in the process [47].

3.5 The angularly-resolved method

We now consider the importance of the phase-matching condition multiwave mixing processes to describe an important work for understanding the experiments presented later in this thesis. In 1984 Raj and coworkers developed a clever technique to systematically discriminate specific higher-order susceptibilities [52]. The method allows to generate any MWM process, one per time, with only three fields by changing only the direction of one of them. The idea is to use the phase-matching condition to enhance a specific order of nonlinearity with respect to the others.

We start explaining the FWM to generalize to MWM latter. Two input fields, Probe (P) and Forward (F), which hereafter we call grating fields, of the same frequency ω and making a small angle 2θ between them interact in the material producing a grating with a period determined by $\Delta\vec{k} = \vec{k_F} - \vec{k_P}$. By this we mean that the interference of the two fields P and F in the medium creates a population (or index) grating, i.e, a spatial modulation of atomic populations (a density grating) in the region of intersection of the fields [Fig.(3.2a)]. Therefore, the incident counter-propagating Backward (B) field is diffracted in this grating in the $-\vec{k_P}$ direction [53]. The signal corresponding to the diffraction is called here D field.

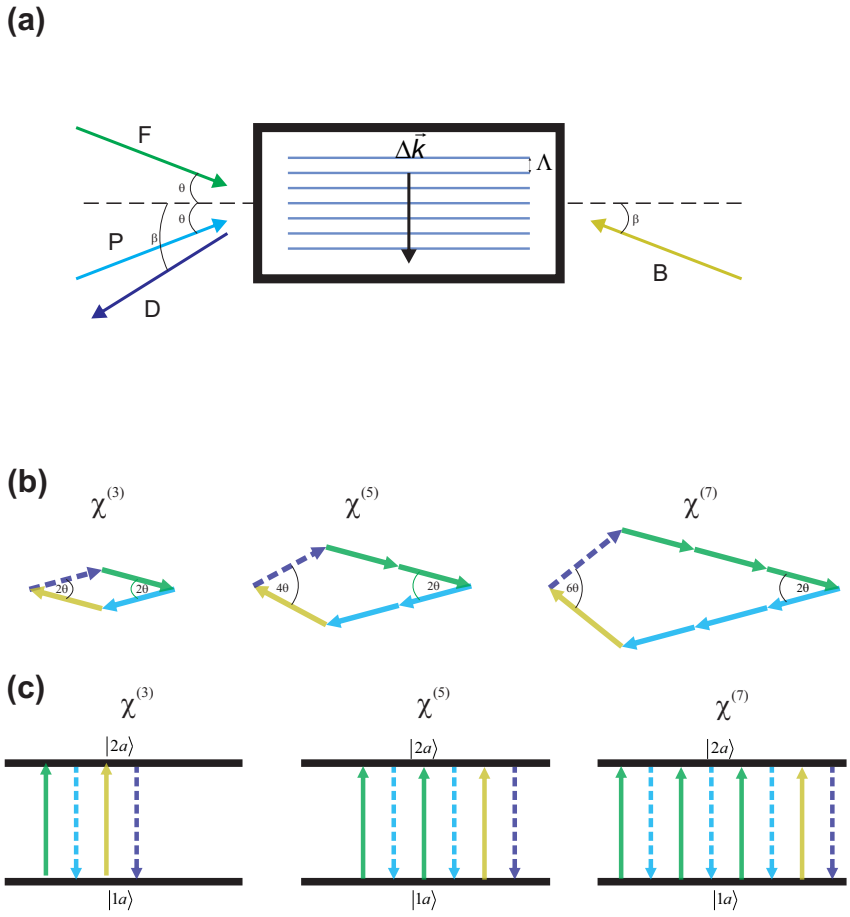

Figure 3.2 (**a**) Two input fields Probe (P) and Forward (F) making a small angle 2θ between them interact in the material producing a grating (indicated by the blue lines) with a period determined by $\Delta\vec{k} = \vec{k_F} - \vec{k_P}$. The incidence of a third counter-propagating beam called Backward (B) at an angle β generates a phase-matched signal. (**b**) Wave vector diagram for the phase matching conditions. (**c**) Absorption-emission sequence in two-level systems.

If the beams are intense, the response of the medium becomes nonlinear and the grating becomes anharmonic producing terms $(\Delta k)^n = \left(\vec{k_F} - \vec{k_P}\right)^n$. The incidence of the B field with wavevector $\vec{k}_B$, same frequency and at an angle β such that $sin\beta = nsin\theta$, generates a phase-matched signal as in the Fig.(3.2a). Note that for small angles the condition $sin\beta = nsin\theta$ corresponds to $\vec{k}_D = \vec{k}_B + n(\vec{k_F} - \vec{k_P})$ as illustrated in Figs.(3.2a) and (3.2b). The lowest order $n = 1$ corresponds to four-wave mixing, in the well known phase conjugation configuration ($\vec{k}_F = -\vec{k}_B$ and $\vec{k}_P = -\vec{k}_D$). Since in this process, with the forward and backward fields counter-propagating to each other, both energy and linear momentum are conserved, in isotropic media, phase-matching is satisfied regardless of the probe direction. In other words, since the momentum contributions of B and F are always canceled, and the D field is always the conjugate of P, the latter can be in any direction.

The absorption-emission sequences for the first three nonlinear orders are depicted in Fig. (3.2c). For the $(2n+1)-$order process, n-paired absorptions and emissions of photons from fields F e P, respectively, are followed by a one-photon absorption of B and one-photon emission of D. In these cases all beams had the same polarization and the processes could be seen in a two-level atom. We will see in the following section that, if the polarizations are different, three or four-level systems are required.

The effectiveness of the method is remarkable and the authors were able to see up to the 11th order of nonlinearity. However, as expected, the efficiency of the generated signal decreases with the increase of the order of nonlinearity for multiple reasons. First due to the reduction of the interaction volume with the order. Second due to the grating fading with atomic motion. As we showed above, the P and F fields create a grating with period $\Lambda = 2\pi/n\Delta k = \frac{\lambda}{2nsin\theta}$. The thermal motion of the atoms mix the population maxima and minima reducing the grating contrast. The smaller the angle between the grating fields, the larger the grating period. As a consequence, the largest conjugated field for four-wave mixing happens when the fields are almost collinear [53]. Thus, small angles are always preferable in this method. As we showed above, higher orders have shorter grating periods (it decreases with $1/n$). More precisely, the fifth order has half of the third, the seventh order has one-third of the third order, and so on. This means that an atom needs to travel two and three time less to blur the fifth and seventh order gratings, respectively. This will have implications in the storage time, when we discuss atomic memories in chapter 5.

A third reason would be obviously the nonlinear process itself. In the model used by the authors, the diffraction efficiency for grating fields with the same intensity scales with $1/\sqrt{(4n^2-1)}$, where $n = 1$ corresponds to $\chi^{(3)}$, $n = 2$ corresponds to $\chi^{(5)}$, $n = 3$ corresponds to $\chi^{(7)}$, and so forth [54]. This implies that the ratio between the various diffraction orders is $[4(n^2-1)/4(m^2-1)]^2$. Therefore, $\chi^{(3)}/\chi^{(5)} = 25$, $\chi^{(5)}/\chi^{(7)} = 5.4$, $\chi^{(7)}/\chi^{(9)} = 3.2$, $\chi^{(9)}/\chi^{(11)} = 2.4$ [54]. These efficiencies are considered by taking the ratio of the peak intensities of the signals and not the total energy.

3.5.1 Polarization rules

Until this point we have not commented in detail about the polarization of the fields involved in the process and its role in it, only mentioning the two-level system case [Fig.(3.2c)].

However, the type of grating created in the medium is polarization dependent. This can lead to various consequences such as differences in the extraction efficiencies, decay rates, etc. To enlighten this statement, consider that all fields have the same polarization. In this case the internal states of the atom can be approximated by a two-level system. Therefore, the fields will create a spatial modulation of the population of the Zeeman sublevels, which corresponds to a population grating. One can also see this process as the interference of the two grating fields in the medium creating an index grating. On the other hand, if the polarizations of the grating fields are orthogonal to each other, these two fields can interact not only through the populations, but also through the Zeeman coherences. No intensity interference pattern can occur. In this case it is the polarization of the total incident field that is spatially modulated, which results in a spatial modulation in the Zeeman atomic coherence. The distinction of population and coherence grating is important since the relaxation rates are different [55].

If all incident fields are linearly or circularly polarized, the polarization of the generated field can be determined from the fact that the atom must return to its initial state at the end of the process, and from the conservation laws of the angular momentum of light and atom. More explicitly, the net angular momentum gained by the atom in the exchange with the three fields must be completely compensated by a single photon of the generated field.

For example, if F and P have the same polarization they will act in a two-level system and the atom will return to the same initial state after the paired interaction with these fields [see Fig. (3.2c)]. As a consequence the generated field will always have the same polarization as the B field (see Fig. (3.2c)). On the other hand, if F and P have orthogonal polarizations, coherence will also be created, so the generated field can have the same polarization as the B field or orthogonal to it, depending if the number of interactions with the grating fields is odd or even.

Conservation laws imply that the process is prohibited if the coherence is created between $\Delta m > 1$ and $\Delta m > 2$ distant sublevels for linear and circular polarizations, respectively. In other words, if the grating fields have orthogonal circular polarizations σ^+ and σ^-, only the $\chi^{(3)}$ process can occur, since after n interactions with these fields the atom would have acquired $2n\hbar$ of angular momentum that would have to be compensated by the absorption of B and emission of D, which can only compensate $2\hbar$. Therefore, $n = 1$, which corresponds to a $\chi^{(3)}$ process, is the only allowed process [see Fig. (3.3a)].

If the grating fields have orthogonal linear polarizations the number of possible processes is much less restricted. Figure (3.3b) shows the $\chi^{(9)}$ case. For an even number of interactions with F and P the polarization of D is parallel to B, while for an odd number of interactions with F and P, the polarization of D is orthogonal to B.

This analysis was confirmed by an experiment where the ratios between the signals having the unexpected polarization and the main signal were always less than 1 : 100 [54].

3.5.2 Frequency up-conversion with $\chi^{(5)}$

It is also possible to use this configuration of multiwave mixing to produce frequency up-conversion [56]. The idea is to use the backward beam B in such a frequency that its wavevector cancels the contribution of the forward beam F. For example, consider a nondegenerate backward six-wave mixing. It is a $\chi^{(5)}$ process with two paired absorptions and emissions of pho-

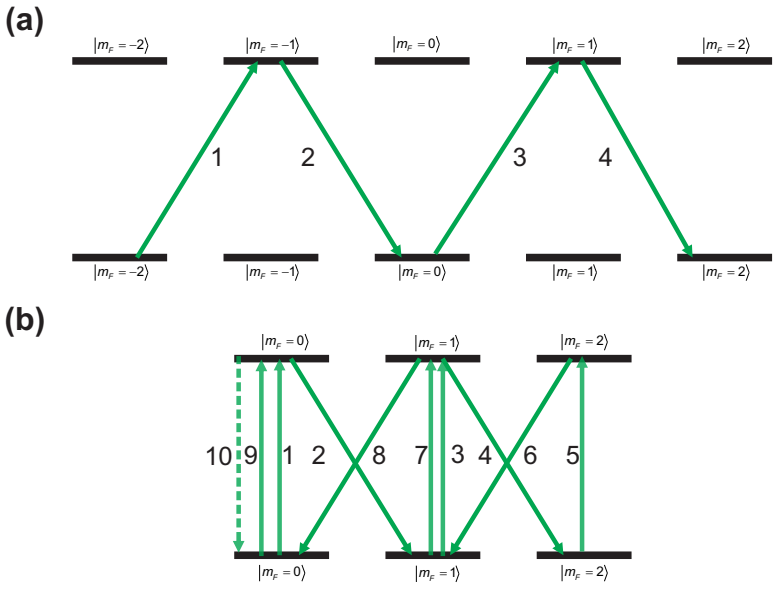

Figure 3.3 Polarization Analysis. (**a**) If the grating fields have orthogonal circular polarizations σ^+ and σ^-, only the $\chi^{(3)}$ process can occur, since after n interactions with these fields the atom would have acquired $2n\hbar$ of angular momentum and wouldn't be able to return to the initial state by the absorption of B and emission of D. (**b**) $\chi^{(9)}$ process for fields with orthogonal linear polarizations. Note that it is possible to return to the initial state by the end of the process.

tons from fields F e P, respectively, followed by a one-photon absorption of B and one-photon emission in D. The generated field D will have a wavevector determined by the phase-matching condition

$$\vec{k}_D = 2(\vec{k}_F - \vec{k}_P) - \vec{k}_B \,. \tag{3.22}$$

Now if we choose B to have the double of the frequency of F, this also implies that it has the double of the wavevector $\vec{k}_B = 2\vec{k}_F$, since $\omega = ck$. Thus, Eq.3.22 becomes

$$\vec{k}_D = -2\vec{k}_P \,. \tag{3.23}$$

This means that phase matching is automatically guaranteed, independently of the direction of the probe, and that the D field will also have twice the frequency of P. Figure 3.4 depicts the idea. Note that in this configuration we have a six-wave mixing process in a four-wave mixing spatial configuration. The B field is counter-propagating to the F field, and the D field is counter propagating to the P field. In a sense, we also have phase-conjugation as in four-wave mixing. More specifically, if F and B are plane waves and the diffraction effects are almost wavelength-independent, the paths of the input and output fields coincide, restoring the original wave front at frequency $2\omega_P$ [56].

If it is possible to do the inverse process entering with a seed in mode D to see the emission in mode P, it would be also possible to do frequency down-conversion.

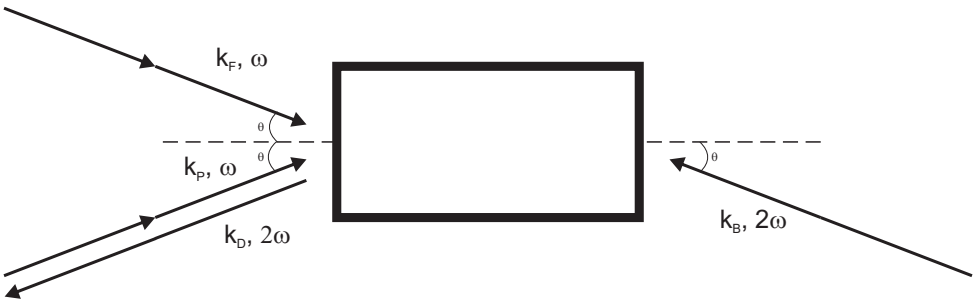

Figure 3.4 Scheme for multiwave mixing with frequency conversion.

Chapter 4

Orbital angular momentum of light

In this chapter we discuss briefly the orbital angular momentum (OAM) of light. We succinctly explain what it is and how it differs from the spin angular momentum. Then we discuss how to generate beams with OAM and how they can be used in quantum information.

4.1 Orbital Angular Momentum of Light

Light carries energy and both linear and angular momenta. The total angular momentum contains basically two contributions. The first is related to the polarization of light. The second part is associated with the spatial profile of the light intensity and phase. Since this is less intuitive than the first part, it was not explored until the early 1900s.

The spin angular momentum is the most intuitive part in our quantum-mechanical era mindset. Since light is constituted by photons, and the photons, by their turn, have spin equal to $\hbar$, then circularly-polarized light has angular momentum. Even though this is correct, Poynting in 1909, and therefore, before the creation of the concept of photon, already stated that circularly polarized light can have angular momentum [57]. Therefore, it is possible to show that light has angular momentum straight from classical electromagnetism without appealing to the concept of photon or any other quantum aspect of light. That is the approach that we will follow to demonstrate the existence of orbital angular momentum of light.

Consider a general field whose amplitude is given by $u(x,y,z,\phi) = u_0(x,y,z)e^{-ikz}e^{i\phi l}$. In the paraxial approximation the electromagnetic fields can be written as

$$B = ik\left[u\hat{y} + \frac{i}{k}\frac{\partial u}{\partial y}\hat{z}\right]e^{ikz}\,, \tag{4.1a}$$

$$E = ik\left[u\hat{x} + \frac{i}{k}\frac{\partial u}{\partial x}\hat{z}\right]e^{ikz}\,. \tag{4.1b}$$

Thus the Poynting vector can be calculated as

$$\varepsilon_0\left\langle \mathbf{E}\times\mathbf{B}\right\rangle = \frac{\varepsilon_0}{2}\left(u\nabla u^* - u^*\nabla u\right) + \omega k\varepsilon_0|u|^2\hat{\mathbf{z}}\,. \tag{4.2}$$

Suppose a field such that $u(r,\phi,z) = u_0(r,z)e^{il\phi}$, then the ϕ component of the Poynting vector is

$$\varepsilon_0\left\langle \mathbf{E}\times\mathbf{B}\right\rangle_\phi = \varepsilon_0\omega l\frac{|u|^2}{r}\,. \tag{4.3}$$

The total angular momentum density is given by the cross product of **r** and the linear momentum density

$$j_z = \mathbf{r} \times \frac{1}{c^2}\mathbf{S} = \varepsilon_0 \omega l |u|^2 \,. \tag{4.4}$$

The energy density is

$$w = c\varepsilon_0 \langle \mathbf{E} \times \mathbf{B} \rangle_z = c\varepsilon_0 \omega k |u|^2 = \varepsilon_0 \omega^2 |u|^2 \,. \tag{4.5}$$

If we take the ratio between the angular momentum density and the energy density we find

$$\frac{j_z}{w} = \frac{l}{\omega}. \tag{4.6}$$

Integrating

$$\frac{J_z}{W} = \frac{\int\int r dr d\phi \, (r \times \langle \mathbf{E} \times \mathbf{B} \rangle)_z}{c \int\int r dr d\phi \, (\langle \mathbf{E} \times \mathbf{B} \rangle)_z} = \frac{l}{\omega}. \tag{4.7}$$

If we multiply by $\hbar$ we find that the angular momentum per photon is $\hbar l$.

4.2 Spin and orbital angular momentum

It can be demonstrated that the total angular momentum of the light can be separated into the spin part, which is associated to the polarization of the electric field, and an orbital part, which is associated to the phase and intensity structure of the beam. The total angular momentum **J** can be written as [58, 59, 60]

$$\boldsymbol{J} = \int dV \varepsilon_0 \boldsymbol{r} \times (\boldsymbol{E} \times \boldsymbol{B}) = \boldsymbol{L} + \boldsymbol{S} \,, \tag{4.8}$$

where **L** and **S** are the orbital and spin parts, respectively. If one writes **B** in terms of the vector potential **A**, it is possible to show after some algebra that Eq. 4.8 can be written as

$$\boldsymbol{J} = \varepsilon_0 \int dV \left[E_i \, (\boldsymbol{r} \times \boldsymbol{\nabla}) A_i + (\boldsymbol{E} \times \boldsymbol{A}) \right] - \varepsilon_0 \int (\boldsymbol{r} \times \boldsymbol{\nabla}) \boldsymbol{E} \cdot d\boldsymbol{S} \,. \tag{4.9}$$

Under some circumstances the surface integral vanishes [58] and we are left with

$$\boldsymbol{L} = \varepsilon_0 \int dV E_i \, (\boldsymbol{r} \times \boldsymbol{\nabla}) A_i \,, \tag{4.10a}$$

$$\boldsymbol{S} = \varepsilon_0 \int dV \, (\boldsymbol{E} \times \boldsymbol{A}) \,. \tag{4.10b}$$

Note that **L** depends on the choice of the origin, just like an orbital angular momentum would (also note the resemblance with the angular momentum operator from quantum mechanics), while **S** does not. This means that **L** is an extrinsic angular momentum, whereas **S** is an intrinsic angular momentum. Moreover, the term ∇A_i in **L** shows the dependence on the phase gradient of the field [60], while **S** clearly depends on the vectorial nature of **E** suggesting a natural association with the spin.

4.2.1 OAM in the quantum level

At the end of section 4.1 it was shown that the ratio of OAM to energy is $\frac{\hbar\ell}{\hbar\omega}$. This would imply that the OAM per photon is $\hbar\ell$, giving us an integer OAM per photon, which is a quantum property. However, we have considered so far the orbital angular momentum only in classical terms. Nonetheless, it is worthy mentioning that OAM is a result of the spatial structure of the beam. Therefore, one should expect also to observe OAM at the single photon level.

Nienhuis and van Enk described theoretically the propagation of fields with OAM using operators [61]. They demonstrate that the Gouy phase is equal to the dynamical phase of a quantum-mechanical harmonic oscillator with time-dependent energy, from where it follows that ℓ is the eigenvalue of this operator. The implication is that one has a quantized OAM.

4.3 Generating beams with OAM

There are some well known modes of the electromagnetic field that can carry OAM. One of the most used, due to the easiness of implementation in laboratories, is the Laguerre-Gaussian mode $LG_p^\ell(\rho,\phi)$. This mode can be described in cylindrical coordinates (ρ,ϕ,z) at the plane $z=0$ by

$$\mathscr{E}(\vec{r}) = LG_p^\ell(\rho,\phi) = \mathscr{E}_0 \left(\frac{\rho\sqrt{2}}{w_0}\right)^{|\ell|} e^{-\frac{\rho^2}{w_0}} e^{-i\ell\phi} L_p^{|\ell|}\left(\frac{2\rho^2}{w_0^2}\right), \tag{4.11}$$

where w_0 and $\mathscr{E}$ are, respectively, the beam waist and amplitude, and $L_p^{|\ell|}$ is the associated Laguerre polynomial with radial index p.

There are several techniques for generating a Laguerre-Gauss mode that use specially designed laser cavities, cylindrical lenses or phase plates [58]. Here it is presented the method that became the most common approach to produce Laguerre-Gauss beams and the one used in this thesis, which uses computer-generated holograms [62]. A hologram is a recorded interference pattern between the desired field and a reference field. Therefore, in many cases one wants to produce the interference pattern between the Gaussian mode, that is readily available from lasers, and the LG mode. If one now shines the reference beam on the hologram, usually a Gaussian mode, the desired mode will be generated.

If two coherent fields $E_1 e^{i\phi_1}$ and $E_2 e^{i\phi_2}$ interfere, a spatial intensity pattern modulated by $2E_1E_2\cos(\phi_1+\phi_2)$ will be produced. This would be the traditional line grating showed in Fig. (4.1a). When we interfere a plane wave with a Hermite-Gauss mode we produce a pattern $E_0 r/\omega e^{-\frac{ikr^2}{2R}\pm i\theta}$ [62]. If the beams are collinear, $\pm\theta = (n+\frac{1}{2})\pi + \frac{kr^2}{2R}$ and we have the interference pattern of Fig. 1 of reference [62]. If the beams are not collinear, then $\pm\theta = (n+\frac{1}{2})\pi + \frac{kr^2}{2R} + kr\sin\gamma\cos\theta$ [62], where γ is the angle between the fields, and we have the interference pattern of Fig. 2 of reference [62]. In Fig. (4.1b) we have a similar interference pattern between a plane wave with a LG beam. These last patterns created by fields with an angle between them are the desired ones, since we usually want to separate the fields easily in the laboratory.

The pattern can be understood as a target phase combined with a diffraction grating. The re-

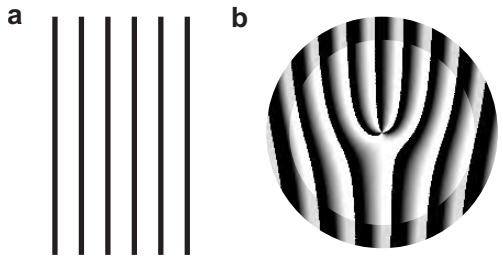

Figure 4.1 Interference patterns. (a) Illustrative interference pattern between two plane waves. (b) Illustrative interference pattern between a plane wave and a Laguerre-Gauss mode when the beams are not collinear.

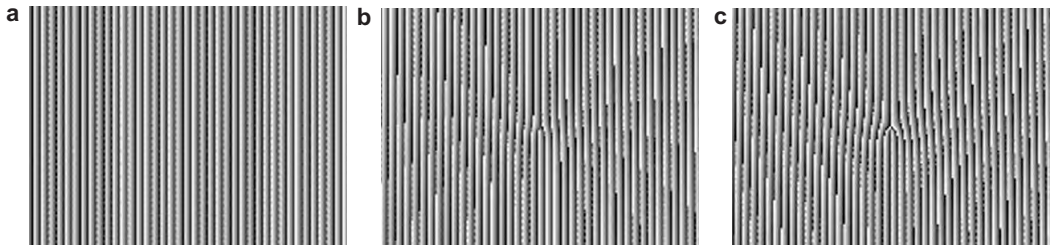

Figure 4.2 Hologram for generation of LG beams. (a) Hologram for $\ell = 0$. (b) Hologram for $\ell = 1$. (c) Hologram for $\ell = 2$

sult is the "forked-grating" shown in Fig. 4.2 that not only reshapes the reflected beam, but also diffracts in the first order the LG beam, and all the other spurious beams are scaterred to other directions (see Fig. 4.3). Therefore, one can separate spatially the field with the desired phase and amplitude structure. The advantage of this method is that these patterns can be created on Spatial Light Modulators (SLM), a commercial device that manipulates the intensity and the phase of the light beams. These gratings can be programed in a computer and reproduced on the LCD interface of the SLM in real time, making it possible to modify it in real time as well.

Another way to interpret the grating showed in Fig. 4.2 is as a line grating with a dislocation at the center. The center line actually splits into two. This means that the diffraction angle in the upper part of the grating it is larger than in the bottom part. This difference exerts a "torque" on the beam, giving a twist to it. This twist will be larger if the central line splits in three lines instead of two. Therefore, changing the pattern we can generate beams with different orbital-angular-momentum values. The important part of this method is to shine not any part of the grating, but the part that contains the fork.

4.4 OAM in quantum information: high-dimensional spaces

Most of the theoretical proposals and experimental implementations in quantum information science are performed in a two dimensional space using qubits, the quantum analog of the classical smallest unit of data, the bit. In classical computation this basic unit can take two values, 0 and 1. The quantum counterpart can be in a superposition of 0 and 1. However, it

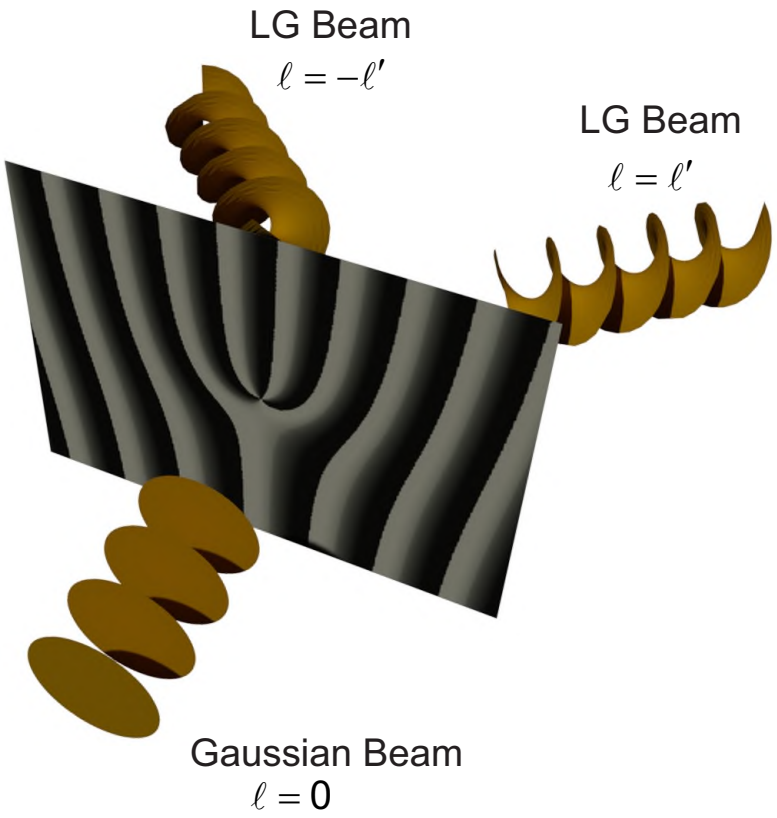

Figure 4.3 Laguerre-Gaussian mode generation from a Gaussian beam. An incident Gaussian beam is transformed by the hologram into a Laguerre-Gauss beam. The order $+1$ of diffraction generates the desired mode with a topological charge ℓ'. The order -1 generates a mode with a topological charge $-\ell'$.

is possible to generalize this idea using higher-dimensional spaces, where the basic unit can go beyond two states. The first question would be: What is the advantage of using higher-dimensional spaces? We name a few:

1. **Increase of encoding capacity.** The first benefit would be the amount of information that could be encoded in each photon. Usually it is considered that the channel capacity is given by Shannon's entropy where one can encode $log_2(d)$ bits per photon. For example, in a fourth dimensional space, where each ququart can encode 2 bits of information $|0\rangle = |00\rangle$, $|1\rangle = |01\rangle$, $|2\rangle = |10\rangle$, and $|3\rangle = |11\rangle$ [63].

2. **More efficient quantum computation.** Campbell et al. demonstrated that distillation techniques using higher-dimensional spaces can outperform qubits counterparts by several orders of magnitude [64]. One can also encode qubits in larger spaces like a qutrit to achieve a more efficient circuit structure [63, 65].

3. **Communication without monitoring signal disturbance.** Quantum key distribution (QKD) uses the quantum nature of the states to achieve secure communication. Broadly speaking since measurements in quantum mechanics change the state, projecting it in a lower dimensional space, any attempt to distinguish the encoded information in the sent quantum state will irreversibly transform it, allowing the detection of an eavesdropper. Therefore, most of the protocols for QKD try to identify parameters that might have been changed by eavesdropping. Using higher-dimensional spaces it is possible to envisage quantum key distribution protocol without monitoring signal disturbance [66, 67].

With that said, how could we prepare these higher-dimensional states in practice? There are various physical systems that can be used, but we focus on orbital angular momentum of light. Here, we just recall that the topological charge increases in discrete steps of $\hbar\ell$, where ℓ is an unbounded integer. Therefore, one can explore OAM to encode information beyond one bit per photon.

Differently from the qubit systems where one can find complete sets of quantum gates, general unitary transformations for qudits encoded in OAM are still a challenge [63]. We plan to give a few suggestions toward this goal using higher-order nonlinear processes in the later chapters.

PART II

Semi-classical regime

Chapter 5

Atomic memory in the semi-classical regime

5.1 Introduction

In this chapter we investigate theoretically and experimentally a nonlinear atomic memory for light by using higher-order atom-field interactions in the semi-classical regime. This chapter is organized as follows. We begin explaining the general idea of the experiment in section 5.2. From section 5.3 to section 5.8 the experimental setup is presented in details. In section 5.9 the theoretical model is explained. This section is subdivided for expository purposes. The writing, dephasing, and reading processes are considered in subsections 5.9.1, 5.9.2, and 5.9.3, respectively. Analytical and numerical solutions are derived to have a deeper understanding of each of these processes and ultimately optimize them. Results and comparisons with the theoretical model are presented in section 5.10. Finally, in section 5.11 the results regarding the utilization of this memory with OAM are shown. The results discussed were published in [26] and [25].

5.2 General idea of the experiment

The basic spatial configuration employed here relies on a method that allows an angular selection of a specific order of nonlinearity [52], presented in chapter 3. The scheme can be summarized as follows [Fig. (5.1a)]. Two optical beams W and W' (writing beams), with linear orthogonal polarizations and an angle $2\theta \approx 2^\circ$ between them, interact with the medium, storing their phase information in it. As a consequence, several gratings, each one corresponding to a different number of interactions with the writing beams, are created that can be selectively accessed by properly choosing the angle of incidence β of the reading beam R, that is switched on after a certain delay t_s. The result of the interaction of R with the induced Zeeman coherence or population is a phased-matched pulse D [see Figs. (5.1a) and (5.1b)], with an electric field amplitude given by

$$\mathscr{E}_D(\vec{r}) \propto \chi^{(2n+1)}\mathscr{E}_R(\vec{r})[\mathscr{E}_W(\vec{r})\mathscr{E}^*_{W'}(\vec{r})]^n e^{i\vec{k}_D\cdot\vec{r}}\,, \tag{5.1}$$

where $\mathscr{E}_i(\vec{r})$ represents the electric field envelop of the beam i ($i = W, W', R, D$) for an atom at position $\vec{r}$, $\vec{k}_i$ is its wavevector, and the phase-matching condition and energy conservation

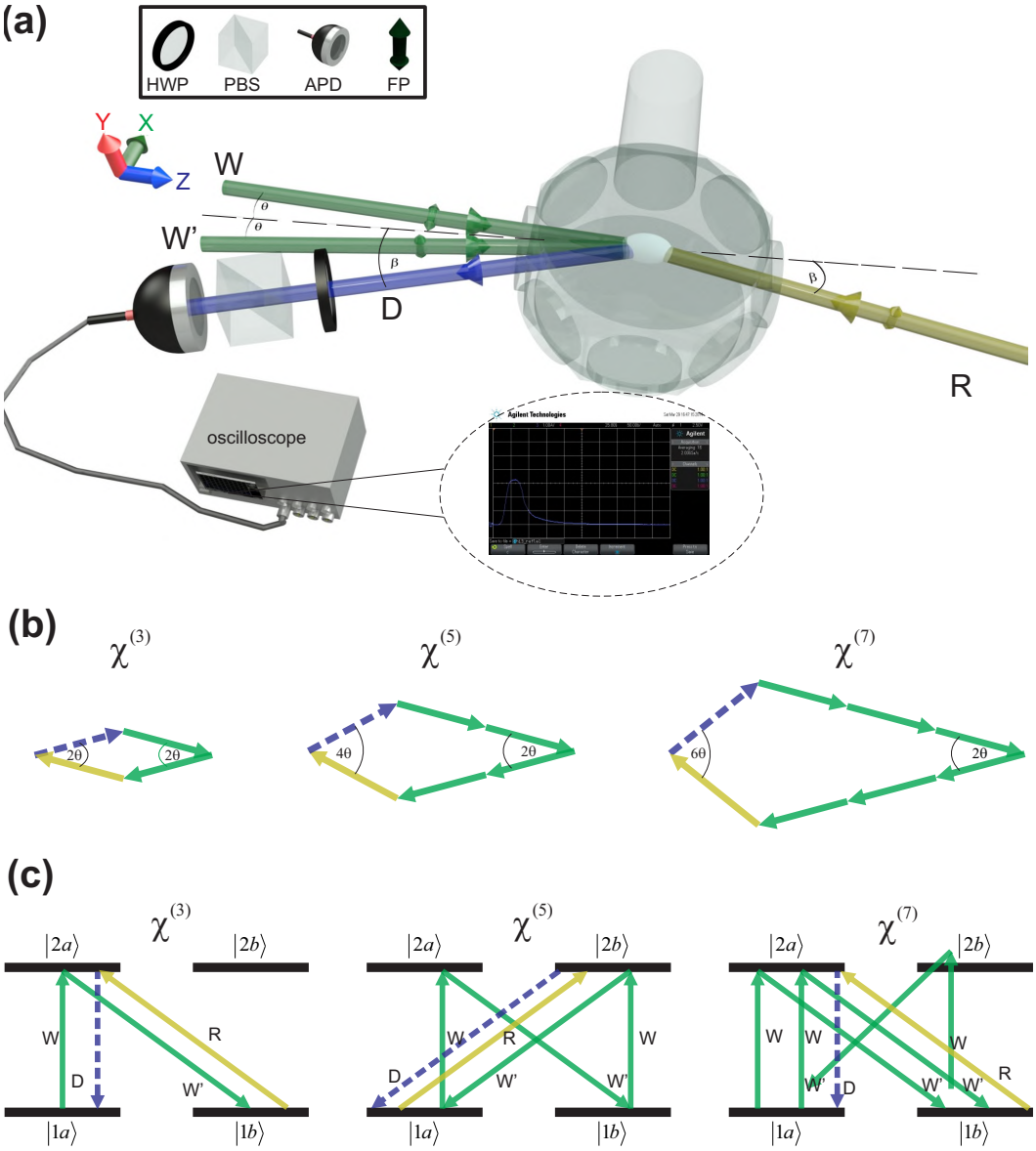

Figure 5.1 Simplified experimental configuration for generation of nonlinear optical memories. (**a**) The cold sample inside the cell is irradiated by two writing beams W and W', forming an angle 2θ between them, generating the population and coherence gratings. A reading beam R switched on after a controllable delay, selects the order of nonlinearity by choosing the angle β with the bisectrix between W and W'. The field polarization (FP) of the retrieved signal D is analyzed with a polarizing beam splitter (PBS), a half wave-plate (HWP), and an avalanche photodetector (APD). The inset shows an example of the signal D observed directly on the oscilloscope screen. This pulse is generated by the medium at the moment that the reading field R is switched on. (**b**) Wave vector diagram for the phase matching conditions, with colors following the scheme for the fields in panel (a). (**c**) Absorption-emission sequence in a generic four-level system associated with the Zeeman sublevels of the hyperfine transition $(F = 3) \rightarrow (F' = 2)$ of cesium D_2 line.

imposes that $\vec{k}_D = n(\vec{k}_W - \vec{k}_{W'}) + \vec{k}_R$ and $\omega_D = n(\omega_W - \omega_{W'}) + \omega_R$. The inset of Fig. (5.1a) show an example of such pulse, observed directly on the oscilloscope screen.

Overall, each process is associated with an effective nonlinear susceptibility $\chi^{(2n+1)}$. The absorption-emission sequence for each nonlinear order is depicted in Fig. (5.1c). For the $2n+1$ order process, n-paired absorptions and emissions of photons in the modes W and W', respectively, are followed by a one-photon absorption of R and one-photon emission of D.

The experiment is performed in a cloud of cold cesium atoms obtained from a magneto-optical trap (MOT) using the Zeeman structure of the hyperfine levels $6S_{1/2}(F=3)$ and $6P_{3/2}(F'=2)$. Three pairs of Helmholtz coils are employed to compensate for residual magnetic fields. The current values of the compensation coils are found by two techniques: microwave spectroscopy in the cesium clock transition $6S_{1/2}(F=3) \rightarrow 6S_{1/2}(F=4)$ [68] and observation of Larmor precession of the atomic memory [69].

In the following sections the formation of the cloud of cold atoms, the fields sequence and other details of the experimental apparatus are explained in more detail.

5.3 Vacuum housing

The whole system is enclosed in a vacuum chamber at a pressure of approximately 10^{-8} mbar sustained by an ion pump (Agilent VacIon plus 20). This high vacuum is necessary to avoid background collisions that would eventually push atoms away from the trapping region. The sequence to achieve this high vacuum can be summarized as follows. First we connect a mechanical pump (Varian Mechanical Vacuum Pumps sd 40) that lowers the pressure to 10^{-3} mbar. Then the turbomolecular pump (Agilent Turbo V81-AG), which is combined with the previous pump in the same equipment, starts to operate automatically reaching 10^{-7} mbar. At this point we can switch on the ion pump to lower the pressure until 10^{-8} mbar. The ion pump can only operate at low pressures, otherwise it may be damaged. Once the desired vacuum is achieved, we close the valve and disconnect the mechanical and turbomolecular pumps. From this point on, only the ion pump remains responsible for keeping the vacuum.

We use alkali metal dispensers as a controllable atom source (Alvatec AS-Cs-60-S) to load Cesium atoms in the vacuum chamber. The sublimation point for such alkali in high vacuum is extremely low. For pure Cesium this can be only 22°C at 1×10^{-6} mbar. Since we work in pressures around 1×10^{-8} mbar, pure alkali dispensers would be unsuitable. Therefore, the dispensers consists of an alloy of an alkali metal with a metal like bismuth inside a stainless steel tube with a sublimation temperature of 450°C at 1×10^{-6} mbar. The dispenser releases pure alkali metal when heated by a current, with the flow proportional to the current. Differently from loading the MOT from a constant background vapor, the dispenser allows to control the number of atoms in the trap (and consequently to vary the optical depth) and the background vapor pressure of cesium. This Cesium vapor fills up the whole chamber by free diffusion including the glass cell, where the MOT will be formed. The glass cell is an octagon with 2.75 cm in height and 5.5 cm in diameter. Each side has a viewport with a diameter of 2.5 cm.

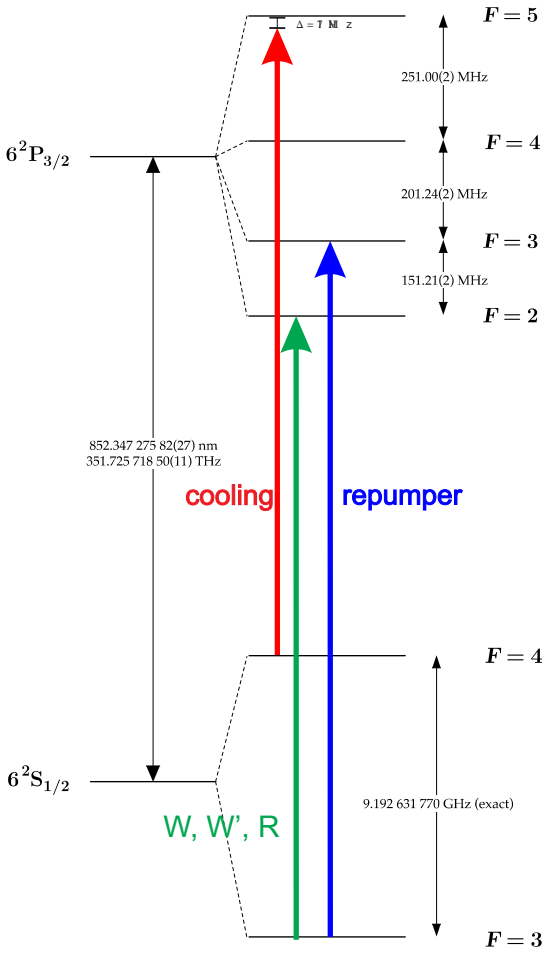

Figure 5.2 Cesium MOT transitions. The cooling laser is tuned 17 MHz below resonance from the $6S_{1/2}(F=4) \rightarrow 6P_{3/2}(F'=5)$ transition, while the repumper is exactly on resonance with the $6S_{1/2}(F=3) \rightarrow 6P_{3/2}(F'=3)$ transition. The write and read fields are tuned to the $6S_{1/2}(F=3) \rightarrow 6P_{3/2}(F'=2)$ transition. The numbers were taken from [70].

5.4 Magneto-optical trap (MOT)

In chapter 2 we already discussed the physical principle of the MOT. Here we detail the practical implementation used in our apparatus. During several years the MOT was the flagship of Atomic Physics. The principles of laser cooling and trapping were already understood and used in laboratories, but the simple and robust setup of the MOT was responsible for the popularization of cold atoms. As explained in chapter 2, one needs six counter-propagating fields, two for each Cartesian axis. The beams are conducted by three independent polarization-maintaining (PM) optical fibers to the glass chamber. At the exit of each fiber there is a collimator with a lens $f = 100$mm, that leaves the beam with 1cm of diameter, and a quarter-wave plate, that changes the linearly polarized light leaving the fiber into circularly polarized light. In the opposite direction there is a mirror to retroreflect the beam and another quarter-wave plate that rotates the polarization by 90° (since the beam passes through it twice) producing a counter-propagating beam with orthogonal polarization in the atomic reference frame.

We omitted a practical detail in the explanation of chapter 2. All the analysis was limited to two-level atoms. However, alkaline atoms are not two-level atoms. They have a whole hyperfine structure. The process of cooling consists in absorption-emission cycles, and it usually takes thousands of them to bring the atom close to rest. Therefore, the first thing we need is to choose a cyclic transition, i.e., a transition that, due to selection rules, forces the atom to return to its original ground state after the excitation. Since the selections rules in the dipole approximation are $\Delta F = 0, \pm 1$, the $6S_{1/2}(F = 4) \rightarrow 6P_{3/2}(F' = 5)$ transition of cesium D2 line is chosen as the cooling transition (see Fig. 5.2).

The hyperfine structure leads to another issue. Every time the laser drives the atom from the ground to the excited state, there is a probability for the atom to be excited to another state and, consequently radiate to the other ground state, especially because the cooling beam must be red-detuned (see chapter 2), interrupting the cooling cycle. This optical pumping can be disastrous since it takes thousands of absorption-emission cycles to bring the atom from its initial velocity to rest (for a sodium atomic beam it could be 3×10^4 cycles [71]), and one would end up with all the atoms in a "dark" state in less than 1 ms. This optical pumping problem was well known since the first studies of deceleration of atomic beams [71]. The solution is to use another laser with a frequency resonant to the transition of the other hyperfine ground state to pump back the atom to the ground state where the cooling laser is. This laser is called repumper. In the cesium case it can be in the $6S_{1/2}(F = 3) \rightarrow 6P_{3/2}(F' = 4)$ or $6S_{1/2}(F = 3) \rightarrow 6P_{3/2}(F' = 3)$ transition. In both cases the atoms have a probability to fall to $6S_{1/2}(F = 4)$ after the excitation.

We use one diode laser (Toptica DL 100), with an output power of approximately 70 mW, to all the six cooling beams and a second diode laser (Toptica DL 100 with a tampered amplifier), with an output power of approximately 200 mW, for the repumper, write, and read beams. The cooling laser is amplified by a tampered amplifier (Toptica BoostA 500 mW). Since we use acousto-optic modulators (AOM) for temporal switching, the cooling laser is locked at the cross-over $F = 4-5$, which is exactly midway to the transitions $6S_{1/2}(F = 4) \rightarrow 6P_{3/2}(F' = 4)$ and $6S_{1/2}(F = 4) \rightarrow 6P_{3/2}(F' = 5)$, while the repumper is locked at the cross-over $F = 2-3$, which is exactly midway to the transitions $6S_{1/2}(F = 3) \rightarrow 6P_{3/2}(F' = 2)$ and $6S_{1/2}(F = 3) \rightarrow 6P_{3/2}(F' = 3)$. A pair of independent AOMs are used to tune the cooling laser and repumping

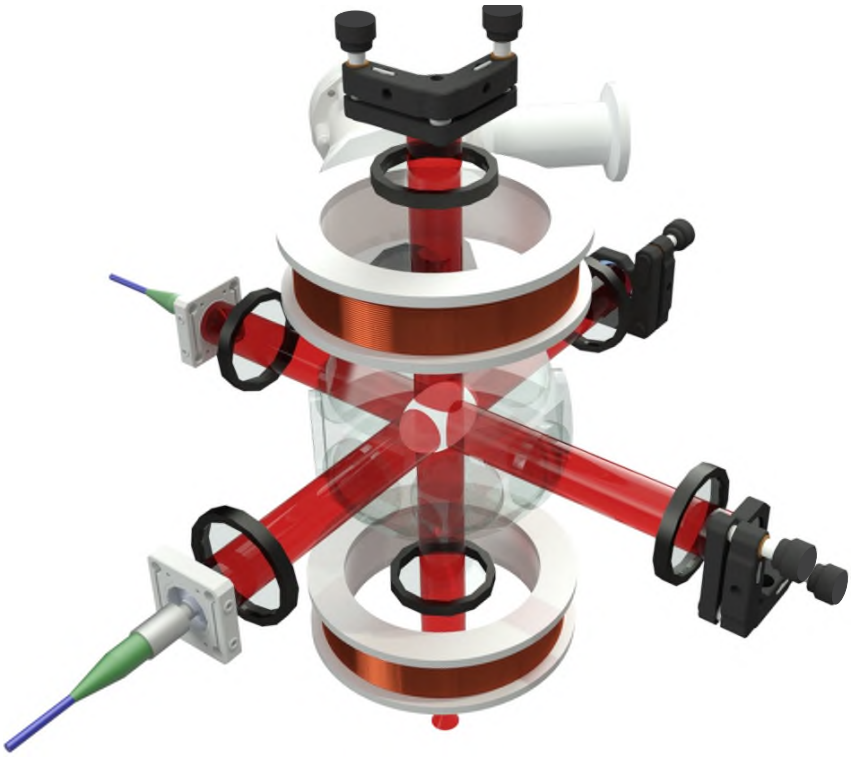

Figure 5.3 Basic implementation of the MOT. Three independent PM optical fibers conduct the beams to the glass chamber (z-axis fiber not shown for simplicity). At the exit of each fiber there is a quarter-wave plate that changes the linearly polarized light that leaves the fiber into circularly polarized light. In the opposite direction a mirror is placed to retroreflect the beam with another quarter-wave plate in front to rotate the polarization in 90° producing a counter-propagating beam with orthogonal polarization. Two coils with currents running in opposite directions generate the magnetic field in anti-Helmholtz configuration.

laser frequencies to 17 MHz below resonance from the $6S_{1/2}(F=4) \rightarrow 6P_{3/2}(F'=5)$ transition and exactly on resonance with the $6S_{1/2}(F=3) \rightarrow 6P_{3/2}(F'=3)$ transition, respectively. We choose the $6S_{1/2}(F=3) \rightarrow 6P_{3/2}(F'=3)$ for the repumper instead of $6S_{1/2}(F=3) \rightarrow 6P_{3/2}(F'=4)$, because we use the same laser for the beams of the experiment per se, the writing and the reading beams, which are tuned to the $6S_{1/2}(F=3) \rightarrow 6P_{3/2}(F'=2)$ transition.

Two coils with currents running in opposite directions generate the magnetic field gradient in anti-Helmholtz configuration. The field is zero at the center and increases linearly as we move away from it. Each coil has 207 turns of copper wire with a diameter of 10.5 cm. The current flowing is about 4 A producing an estimated gradient of 10 G/cm in the MOT region.

One last comment is about the optimization of the cloud. If the beams configuration is symmetrical, i.e. the beams are exactly counter-propagating and have the same power, the cloud should be close to a sphere. However, we deliberately misalign the beams to produce a pencil-shaped atomic sample that points in the same direction as the writing and reading beams. This makes the medium optically thicker along the desired direction enhancing the coupling between light and matter. Consequently, this also increases the measured value of the

optical depth. The practical consequences are quite significant. For example, we can observe an improvement on the observed signals amplitude of the order of 16 for a variation of the optical depth from 1.15 to 4.42.

5.5 Control system

All the pulsed quantities of the experiment, such as the magnetic field, cooling, repumper, writing, and reading fields, are electronically controlled by a National Instruments board (NI PCI 6602 80 MHz), operated by a LabVIEW (National Instruments) software. All the pulses are generated in 23 ms long cycles and they repeat themselves at the end of each cycle. First we generate a pulse to switch on the cooling and repumper beams for 21 ms and 20 ms, respectively. The MOT magnetic field remains on during the same 20ms of the repumper (see Fig.5.4). The coils that compensate any residual magnetic fields have no temporal control and stay on continually. During the extra 1ms of the cooling beams pulse the atoms are optically pumped from $6S_{1/2}(F=4)$ to $6S_{1/2}(F=3)$, preparing the desired initial state. After preparing our initial state, we wait for 1.2 ms to eliminate any magnetic field transients and to avoid leakage from the MOT beams. The experiment concerning the atomic memory occurs in the final 800 μ s of the cycle (Fig.5.4). This interval is short enough to guarantee that the atoms will not leave the confinement region and the cloud will not expand significantly, since they are sufficiently cold. A simple calculation can clarify this. If we consider an atom initially at rest we find that it takes 20 ms for its free fall from a 2 mm height, which is a typical cloud diameter. This is about 500 times greater than the total 40 μs window where the memory experiment takes place.

The write beam stays on for 25 μs imprinting its phase information in the medium. The grating can be formed in a shorter time, but we intentionally exaggerate the period to guarantee a steady state. The same goes for the reading beam pulse, that is switched on for 15 μs. As we will show later, the signal emitted by the medium during the reading process varies between hundreds of nanoseconds to a few microseconds (less than 10).

5.6 Write and read beams configuration

The writing fields have orthogonal linear polarizations set by the transmission of two polarizing beam splitters (PBS) inverted to each other. They both pass through a single acousto-optic modulator (AOM), which allows to control jointly their frequencies and amplitudes, and have both a waist of the order of 1.2 mm in the ensemble. The reading beam is controlled by an independent AOM. It has a waist of approximately 1.5 mm and linear polarization parallel to W'. There is no applied magnetic field, thus we define here the quantization axis as being parallel to the polarization of the W beam. The writing beams are resonant with the transition $6S_{1/2}(F=3) \rightarrow 6P_{3/2}(F'=2)$ while the reading beam may be detuned by Δ in relation to this transition.

All the beams are conducted to the experiment through polarization-maintaining (PM) optical fibers. We have one fiber for the writing beam, whose power is split with a PBS to produce

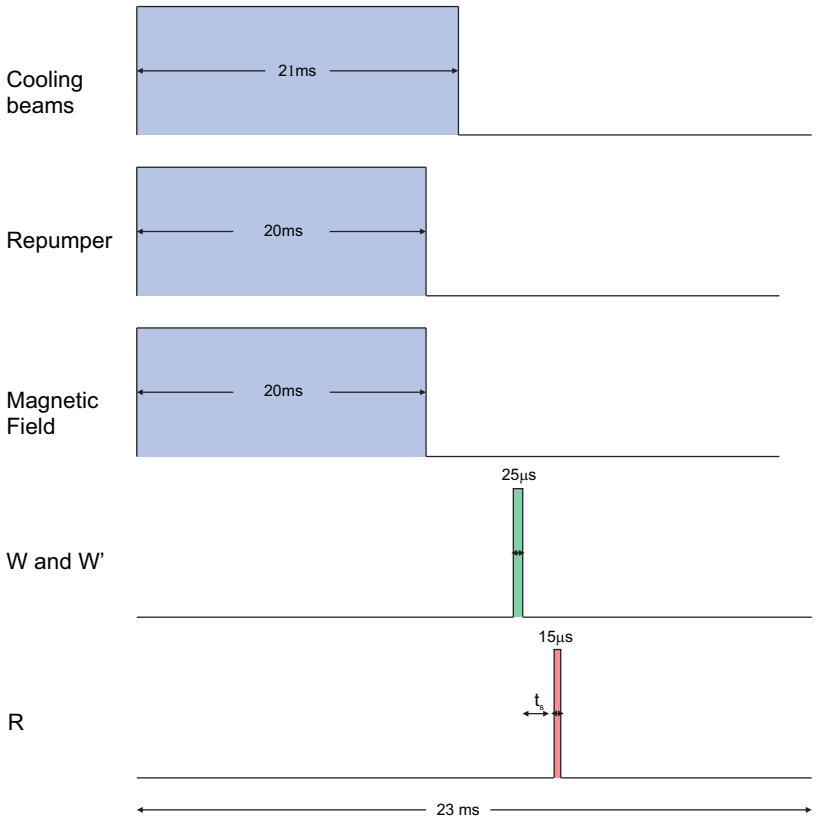

Figure 5.4 Experiment pulse sequence. The cooling beam stays on during 21ms, while the repumper and the magnetic field are on during 20ms. During the extra 1ms of the cooling beams pulse the atoms are optically pumped from $6S_{1/2}(F=4)$ to $6S_{1/2}(F=3)$ preparing the desired initial state. After that the write beam is switched on for 25 μs imprinting the phase information in the medium. Finally, the reading beam pulse is switched on after a delay t_s for 15 μs recovering a signal.

the W and W' beams. Another fiber is used for the reading beams. The power is split with two PBSs but into three parts. We preset the direction of the $\chi^{(3)}$, $\chi^{(5)}$, and $\chi^{(7)}$ reading beams with three pairs of mirrors. We control the power going to each direction by rotating half-wave plates before each PBS. Therefore, only one direction is used in each measureament. If we want to see the $\chi^{(3)}$ signal we rotate the half-wave plates to leave all the power in the $\chi^{(3)}$ read field direction and zero in the $\chi^{(5)}$ and $\chi^{(7)}$ directions. The same goes for the other two orders. In the experiments and results showed below it is never used more than one read field at the same time. Only one order is observed by turn. We also use three extra PBSs before each pair of mirrors to clean the polarization for each reading field.

The waist of each beam is crucial. Since we are attempting to investigate higher-order nonlinearities, the interaction volume of the beams in the sample is very important. We try to shine almost the entire cloud (about 70%) to include as much atoms as possible in the process, to increase the signal. The shape of the cloud can also collaborate to the phase-matching of the different diffraction orders. In our case the W, W' have approximately 1.3 mm and the reading beam 1.5 mm. A smaller waist, say 200 μm, is enough to observe the $\chi^{(3)}$ signal, but is not enough to observe the $\chi^{(5)}$ and $\chi^{(7)}$ signals, at least with our optical depths. These waists were the optimum values for our experiment. Obviously if one is able to increase the atomic density in the cloud even further the optimum values could be different.

5.7 Detection

The detection system here is relatively simple compared to the single photon counter-part described in chapter 7. Since each signal, as we will show in section 5.9.3, should have a well defined polarization according to the theory, the whole detection was mounted to enable the identification of the polarization of the signals. All the polarizations involved are linear and defined in relation to the reading beam. A PBS is used to split the two components of the polarization and each component is detected by avalanche photo detectors (Thorlabs APD 110A/M) for intense fields (not for single photons) in free space. This is different from the single photon case of chapter 7, which has only in-fibers detectors. The model APD 110A/M has a bandwidth of 50 MHz, which is fast enough to not distort the pulses unlike other models used previously in our laboratory [72], and operates between a few nW and tenths of μW, enabling to detect the higher orders which typically are in the nanowatt range. For the stronger $\chi^{(3)}$ signals, that could be above the detector maximum input power, we used filters in front of it.

The $\chi^{(3)}$ signal enters through one port of the PBS and the $\chi^{(5)}$ and $\chi^{(7)}$ through the other (see Figure 5.5). This configuration permits to measure the ratio between the two polarization components of each signal. The $\chi^{(3)}$ presented a ratio of 300 to 1 (correct and spurious components, respectively), the $\chi^{(5)}$ 100 to 1, and the $\chi^{(7)}$ 100 to 1. Each APD is connected to a digital oscilloscope (Keysight DSOX2014A) channel, that by its turn is connected to a PC. A LabVIEW (National Instruments) software captures, processes (calculating retrieved peak intensity, energy, and other quantities), and displays graphs of the signal in real time.

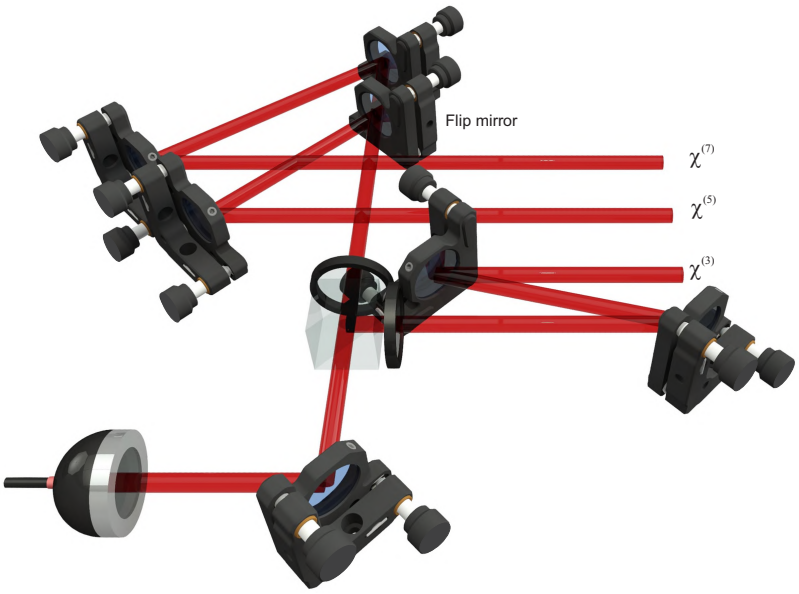

Figure 5.5 Simplified configuration for detection of different signals.

5.8 Cancellation of spurious magnetic fields

As we will detail in the next sections we can establish two main mechanisms for decoherence in our memory. The first one is inhomogeneous broadening of the ground state by spurious magnetic fields [73] and the second one is atomic motion [74, 75]. Therefore, cancellation of stray magnetic fields is crucial to increase the storage time.

5.8.1 Microwave spectroscopy

The principle of the technique explained in this section is also described in [68]. The atoms are prepared in the hyperfine level $6S_{1/2}(F=4)$ and evenly distributed in its Zeeman structure. A microwave pulse with frequency $\omega = (9.2+\delta)GHz$ pumps atoms from $6S_{1/2}(F=4)$ to $6S_{1/2}(F=3)$ by magnetic dipole transitions with $\Delta m = 0, \pm 1$ when its frequency is resonant with the transition $|F=4,m_F\rangle \rightarrow |F=3,m_F\rangle$ (see Fig.5.6). A optical pulse resonant with the transition $6S_{1/2}(F=3) \rightarrow 6P_{3/2}(F'=2)$ probes the population of $6S_{1/2}(F=3)$ for each value of δ.

A homemade rf antenna fed by a microwave analog signal generator (Agilent 8257D PSG) produces the microwave signal. With an output power of 21dBm the microwave pulse is on during $150\mu s$. The pulse sequence is displayed in Fig.5.7. We switch on the probe pulse for $15\mu s$ before and after the microwave pulse for reasons that will be clear soon.

We detect the probe transmission before and after the microwave and subtract the two signals. We scan the microwave signal to detect the variation of the probe transmission when the microwave frequency is resonant with one of the ground state hyperfine transitions $|F=4,m_F\rangle \rightarrow |F=3,m'_F\rangle$, as shown in Fig.(5.6a). When the microwave is not resonant with a transition, no atom is transferred from $6S_{1/2}(F=4)$ to $6S_{1/2}(F=3)$ and the probe resonant with $6S_{1/2}(F=$

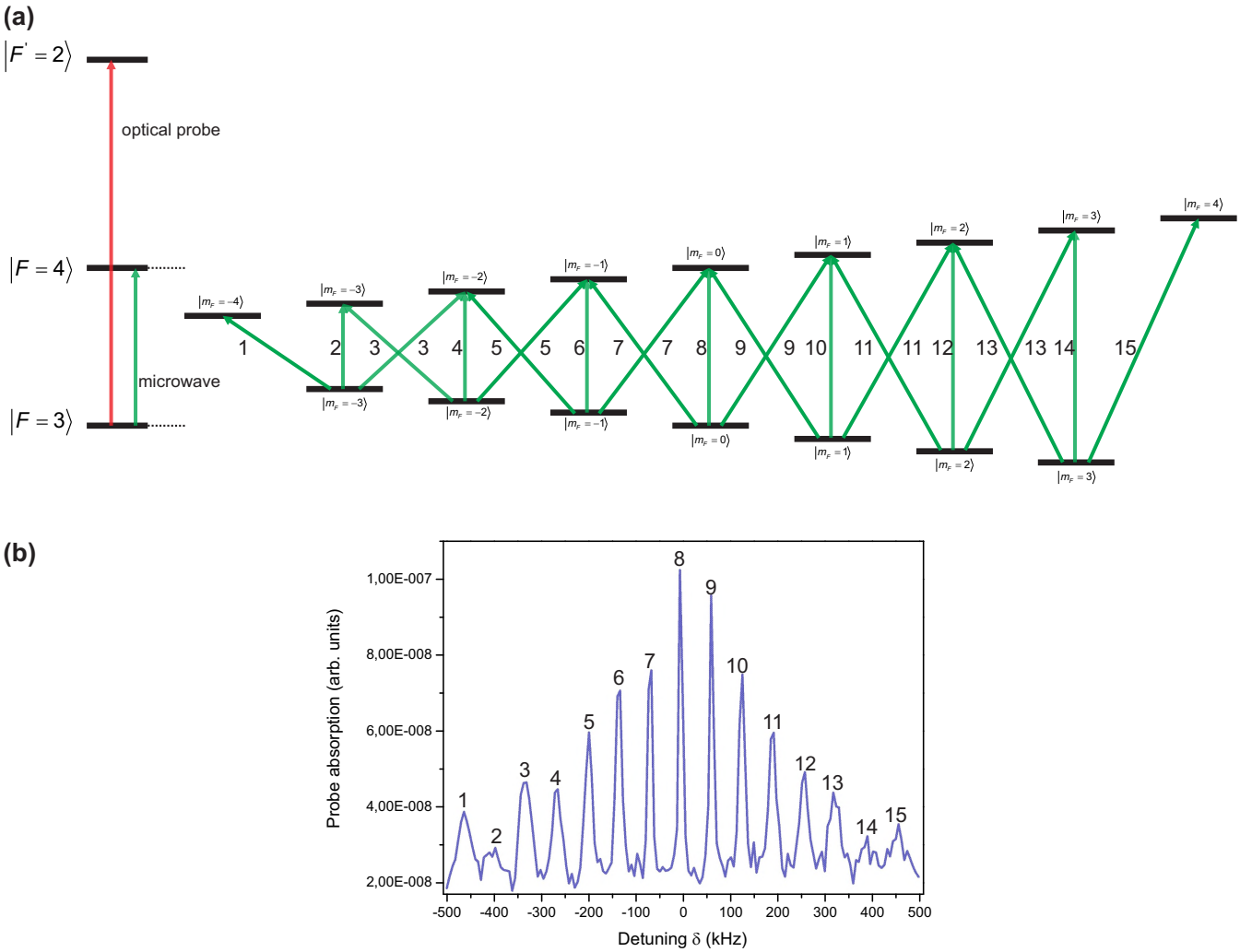

Figure 5.6 Microwave spectroscopy. (a) The atoms are prepared in the hyperfine level $6S_{1/2}(F=4)$ and evenly distributed in its Zeeman structure. A microwave pulse with frequency $\omega = (9.2+\delta)GHz$ pumps atoms from $6S_{1/2}(F=4)$ to $6S_{1/2}(F=3)$ by magnetic dipole transitions with $\Delta m = 0, \pm 1$, when its frequency is resonant with one of the 15 independents transition $|F=4, m_F\rangle \rightarrow |F=3, m'_F\rangle$. The transmission of an optical probe pulse which is switched on before and after the microwave is measured. (b) When the microwave is resonant with one of the transitions, the subtraction is not zero, yielding a peak in the spectrum. All 15 peaks are seen when the residual field is not compensated.

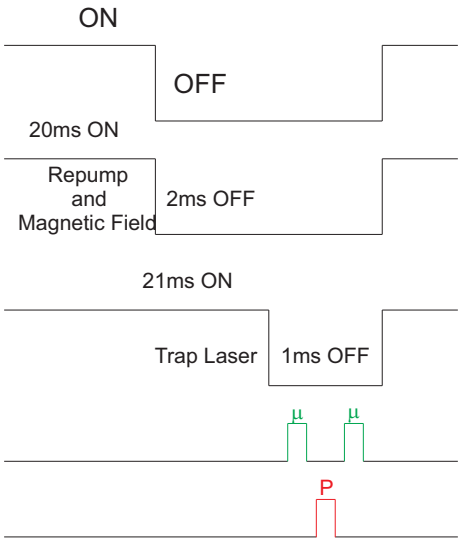

Figure 5.7 Microwave spectroscopy pulse sequence. An optical probe pulse is switched on for $15\mu s$ to set the zero level of absorption. After that the microwave pulse is turned on for $150\mu s$. The optical probe pulse is switched on again for $15\mu s$ to probe if any atom was transferred by the microwave.

3) and $6P_{3/2}(F'=2)$ is not absorbed, yielding a null difference. When the microwave is resonant, population is transferred and we have a non-vanishing subtraction between the probe transmissions, generating peaks, as shown in Fig.(5.6b). There are 21 allowed magnetic dipole transitions with $\Delta m = 0, \pm 1$. However, some of them have the same frequency, leaving only 15 different frequencies. This is depicted in Fig.(5.6a). The transitions with the same frequency have the same label, e.g., the transition $|F=4, m_F=-3\rangle \rightarrow |F=3, m_F=-3\rangle$ and $|F=4, m_F=-2\rangle \rightarrow |F=3, m_F=-2\rangle$ both have the label 3.

The distance between two adjacent peaks also gives a measure of the splitting of the Zeeman sublevels. Since the displacement of a sublevel m_F is $\mu_B g_F m_F B$, where μ_B is the Bohr magneton and g_F is the Landé factor, one finds that the distance between two adjacent peaks is $\mu_B g_F B$. The width of the whole spectrum is $(15-1)\mu_B g_F B = 14\mu_B g_F B$.

Three pairs of Helmholtz coils (one pair for each axis) are used to compensate for stray magnetic fields. The current for each pair is set independently. As we vary the current, the peaks can move far apart, indicating that we are increasing the magnetic field, or close together, indicating that we are minimizing the magnetic field. Therefore, the idea is to cancel the field to a point that all peaks merge into one with the narrowest width possible. Figure (5.8b) shows the spectrum after the cancellation, presenting a width of 53 kHz. This corresponds to a residual field of $B = 53\ \text{kHz}/(14\mu_B g_F) \approx 10.6$ mG.

This method can also be used to probe the efficiency of the optical pumping. If one uses a circular polarized beam to pump all atoms to the extremes of the Zeeman structure the atoms will no longer be evenly distributed and we would see only the outermost peak of the right or left, depending if one uses a σ^+ or σ^- beams [76].

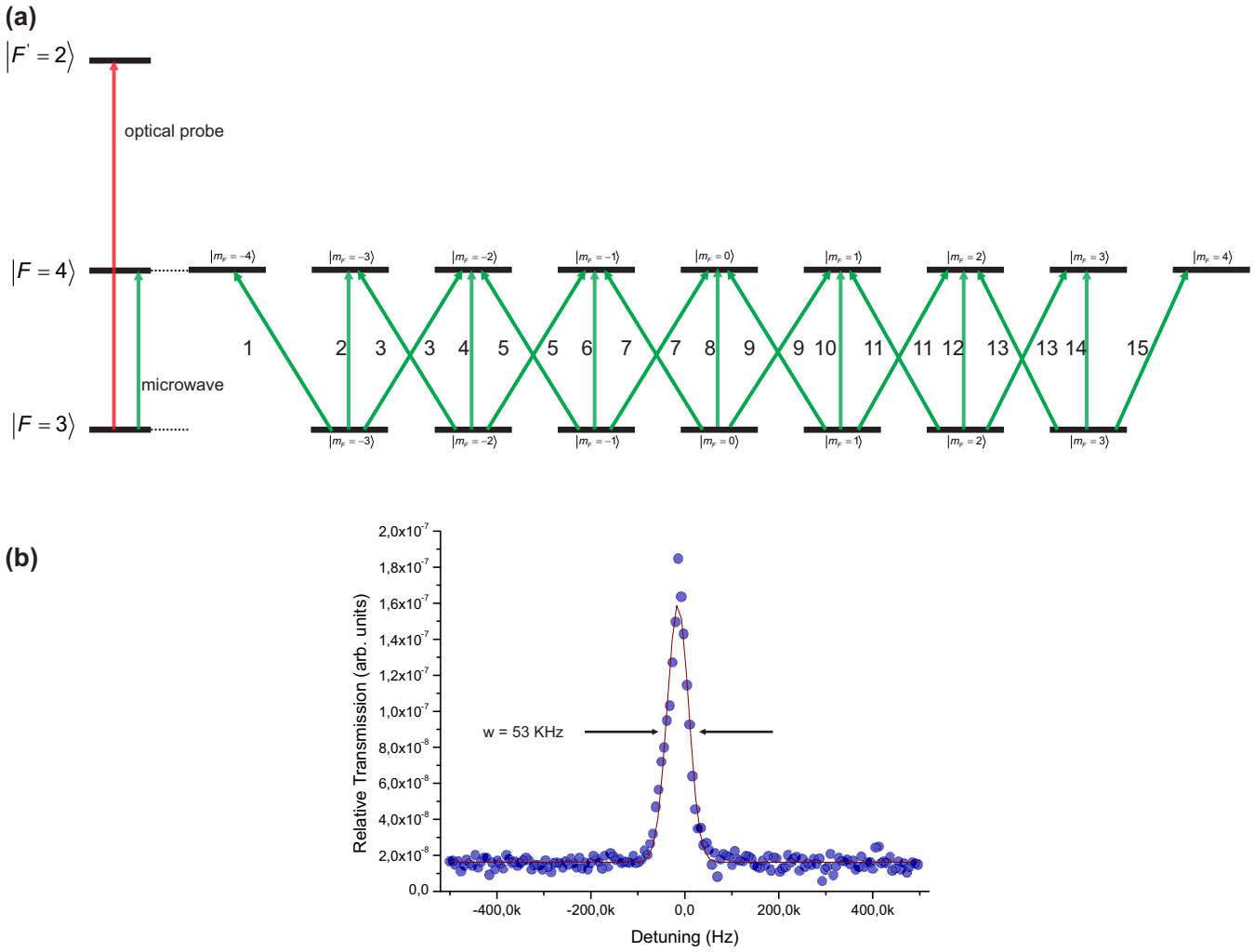

Figure 5.8 Microwave spectroscopy for a cancelled magnetic field. (a) When the residual field is compensated the Zeeman structure becomes completely degenerated. (b) All 15 peaks of Fig.(5.6b) are merged in one.

5.9 Theoretical Model

Here we analyze in detail the mechanisms of the nonlinear optical memory since the creation of the grating up to the extraction of the field D, resulting in a quantitative calculation of the most relevant physical features. Although the actual polarization configuration used in the experiment would lead to the coupling of all the Zeeman sublevels, we approximate the Zeeman degeneracy of cesium as a four-level atom, with two degenerated ground states $|1a\rangle, |1b\rangle$ with zero energy and two degenerated excited states $|2a\rangle, |2b\rangle$ with energy $\hbar\omega_0$.

In order to enlighten the whole process, we divide it into three steps. First, the medium is irradiated for 25 μs by two writing beams W and W', a time long enough to leave the system in a steady state. During this writing process, two different types of grating are formed: a coherence and a population grating. As will be shown, each of them stores only specific orders of nonlinearities, which implies that part of the information is stored in the population and the other part in the ground-state coherence. By information, we mean, for example, the optical phase or the phase associated with beams carrying orbital angular momentum of light. Second, the fields are turned off, letting the system evolve freely. The optical coherences, the excited-state coherences, and the excited populations decay rapidly, leaving the system with only the populations of the ground states and the coherences between them. This is the stage where only the decoherence processes act on the state of the first part. Third, a reading beam R, whose angle of incidence depends on which order is desired to be accessed, is turned on retrieving the information stored in the atomic ensemble as a pulse diffracted along the phase-matching direction with a polarization that leaves the atom in the initial state before the interaction with the writing beams [see Fig. (5.1c)]. In the reading process we are not looking for the steady-state solution as in the writing process, but the full temporal evolution of the optical coherences that induces a polarization in the medium, that, by its turn, generates the detected field.

5.9.1 Writing

We consider an atom excited by two writing fields (W and W'), with orthogonal linear polarizations. The field E_W propagates along the z direction while the field $E_{W'}$ forms a small angle 2θ as depicted in Fig. (7.6a). Then, we can write

$$\vec{E}_W = \frac{1}{2}[\mathscr{E}_W(\vec{r},t)e^{i(k_W z-\omega_W t)} + \mathscr{E}_W^*(\vec{r},t)e^{-i(k_W z-\omega_W t)}]\hat{x}\,, \tag{5.2a}$$

$$\vec{E}_{W'} = \frac{1}{2}[\mathscr{E}_{W'}(\vec{r},t)e^{i(\vec{k}_{W'}\cdot\vec{r}-\omega_{W'}t)} + \mathscr{E}_{W'}^*(\vec{r},t)e^{-i(\vec{k}_{W'}\cdot\vec{r}-\omega_{W'}t)}]\hat{y}\,, \tag{5.2b}$$

where $\mathscr{E}_i(\vec{r},t)$ is the electric field envelope of beam $i (i = W, W')$. The system Hamiltonian can then be written as

$$\hat{H}(t) = \hat{H}_0 + \hat{H}_{int}(t)\,, \tag{5.3}$$

where

$$\hat{H}_0 = \hbar\omega_0\left(|2a\rangle\langle 2a| + |2b\rangle\langle 2b|\right) \tag{5.4}$$

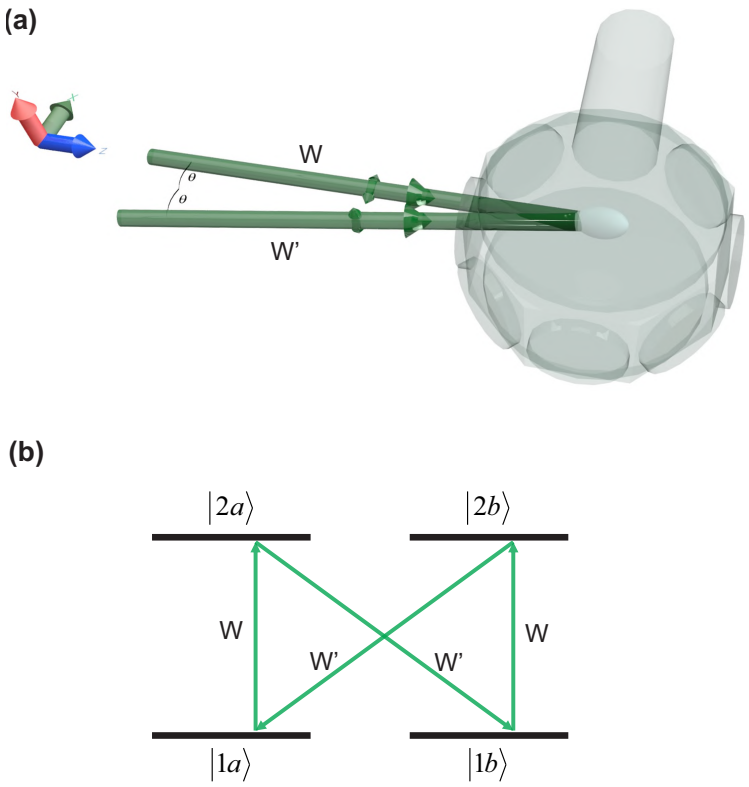

Figure 5.9 (**a**) The cold sample inside the cell is irradiated by two writing fields W and W', with orthogonal linear polarizations and forming an angle 2θ between them. (**b**) Coupling of the writing fields with the internal states of the atom.

is the Hamiltonian for the free atom and

$$\begin{aligned}\hat{H}_{int}(t) = &-\vec{d}_{1a,2a}\cdot\vec{E}(t)\,|1a\rangle\langle 2a| - \vec{d}_{1b,2b}\cdot\vec{E}(t)\,|1b\rangle\langle 2b| \\ &-\vec{d}_{1a,2b}\cdot\vec{E}(t)\,|1a\rangle\langle 2b| - \vec{d}_{1b,2a}\cdot\vec{E}(t)\,|1b\rangle\langle 2a| \\ &+h.c.\end{aligned} \tag{5.5}$$

is the interaction Hamiltonian with $\vec{E} = \vec{E}_W + \vec{E}_{W'}$. The master equation describing the evolution of the system is given by

$$\frac{\partial \rho_{ij}}{\partial t} = \frac{1}{i\hbar}\langle i|[\rho, H]|\,j\rangle + \left(\frac{\partial \rho_{ij}}{\partial t}\right)_{rel} \tag{5.6}$$

where $\left(\frac{\partial \rho_{ij}}{\partial t}\right)_{rel}$ are the relaxation terms, which are introduced phenomenologically. Defining the slowly varying coherences

$$\sigma_{1a,2a} = \rho_{1a,2a}e^{-i\omega t}\,, \tag{5.7a}$$
$$\sigma_{1b,2b} = \rho_{1b,2b}e^{-i\omega t}\,, \tag{5.7b}$$
$$\sigma_{1a,2b} = \rho_{1a,2b}e^{-i\omega t}\,, \tag{5.7c}$$
$$\sigma_{1b,2a} = \rho_{1b,2a}e^{-i\omega t}\,, \tag{5.7d}$$

in the rotating wave approximation, the time evolution of the slowly varying populations and coherences are given by the equations:

$$\frac{d\rho_{2a,2a}}{dt} = \beta\Omega^*_{W'}\sigma_{2a,1b} + \beta\Omega_{W'}\sigma_{1b,2a} + \Omega^*_W\sigma_{2a,1a} + \Omega_W\sigma_{1a,2a} - \Gamma\rho_{2a,2a}\,, \tag{5.8a}$$
$$\frac{d\rho_{2b,2b}}{dt} = \Omega^*_{W'}\sigma_{2b,1a} + \Omega_{W'}\sigma_{1a,2b} + \alpha\Omega^*_W\sigma_{2b,1b} + \alpha\Omega_W\sigma_{1b,2b} - \Gamma\rho_{2b,2b}\,, \tag{5.8b}$$
$$\frac{d\rho_{1a,1a}}{dt} = -\Omega^*_{W'}\sigma_{2b,1a} - \Omega_{W'}\sigma_{1a,2b} - \Omega^*_W\sigma_{2a,1a} - \Omega_W\sigma_{1a,2a} + \frac{\Gamma}{2}(\rho_{2a,2a} + \rho_{2b,2b})\,, \tag{5.8c}$$
$$\frac{d\rho_{1b,1b}}{dt} = -\beta\Omega^*_{W'}\sigma_{2a,1b} - \beta\Omega_{W'}\sigma_{1b,2a} - \alpha\Omega^*_W\sigma_{2b,1b} - \alpha\Omega_W\sigma_{1b,2b} + \frac{\Gamma}{2}(\rho_{2a,2a} + \rho_{2b,2b})\,, \tag{5.8d}$$
$$\frac{d\sigma_{1a,2a}}{dt} = \beta\Omega^*_{W'}\sigma_{1a,1b} - \Omega^*_{W'}\sigma_{2b,2a} + \Omega^*_W\rho_{1a,1a} - \Omega^*_W\rho_{2a,2a} - \left(\frac{\Gamma}{2} + i\Delta\right)\sigma_{1a,2a}\,, \tag{5.8e}$$
$$\frac{d\sigma_{1b,2b}}{dt} = -\beta\Omega^*_{W'}\sigma_{2a,2b} + \Omega^*_{W'}\sigma_{1b,1a} + \alpha\Omega^*_W\rho_{1b,1b} - \alpha\Omega^*_W\rho_{2b,2b} - \left(\frac{\Gamma}{2} + i\Delta\right)\sigma_{1b,2b}\,, \tag{5.8f}$$
$$\frac{d\sigma_{1a,2b}}{dt} = \alpha\Omega^*_W\sigma_{1a,1b} - \Omega^*_W\sigma_{2a,2b} + \Omega^*_{W'}\rho_{1a,1a} - \Omega^*_{W'}\rho_{2b,2b} - \left(\frac{\Gamma}{2} + i\Delta\right)\sigma_{1a,2b}\,, \tag{5.8g}$$
$$\frac{d\sigma_{1b,2a}}{dt} = -\alpha\Omega^*_W\sigma_{2b,2a} + \Omega^*_W\sigma_{1b,1a} - \beta\Omega^*_{W'}\rho_{2a,2a} + \beta\Omega^*_{W'}\rho_{1b,1b} - \left(\frac{\Gamma}{2} + i\Delta\right)\sigma_{1b,2a}\,, \tag{5.8h}$$
$$\frac{d\sigma_{1a,1b}}{dt} = -\alpha\Omega_W\sigma_{1a,2b} - \Omega^*_W\sigma_{2a,1b} - \beta\Omega_{W'}\sigma_{1a,2a} - \Omega^*_{W'}\sigma_{2b,1b}\,, \tag{5.8i}$$
$$\frac{d\sigma_{2a,2b}}{dt} = \alpha\Omega^*_W\sigma_{2a,1b} + \Omega_W\sigma_{1a,2b} + \Omega^*_{W'}\sigma_{2a,1a} + \beta\Omega_{W'}\sigma_{1b,2b} - \Gamma\sigma_{2a,2b}\,, \tag{5.8j}$$

where $\Delta = \omega - \omega_0$ is the detuning,

$$\Omega_j(\vec{r},t) = \frac{id_j\mathscr{E}_j(\vec{r},t)e^{i\vec{k}_j\cdot\vec{r}}}{4\hbar} \tag{5.9}$$

is the Rabi frequency associated with beam j, and $\Gamma/2\pi(=5.2MHz)$ is the total spontaneous decay rate of the cesium excited state. The system is considered closed, so $\rho_{1a,1a}+\rho_{1b,1b}+\rho_{2a,2a}+\rho_{2b,2b}=1$, and α and β are dimensionless coefficients, which are taken to be real and are introduced to take into account the different values of the Clebsch-Gordan coefficients of the transitions. We considered $d_{1b,2b}=\alpha d_{1a,2a}$ and $d_{1a,2b}=\beta d_{1b,2a}$, leaving the equations with four different Rabi frequencies, namely Ω_W, $\alpha\Omega_W$, $\Omega_{W'}$, and $\beta\Omega_{W'}$. These differences in the Rabi frequencies are important as we will see shortly.

The response of the system is found, in the steady state regime, in all orders in the W field and in first, second, and third order in the W' field. The solutions for the coherence and populations, for $\Delta=0$, are

$$\rho^{(0)}_{1a,1a} = \rho^{(0)}_{1b,1b} = \frac{\left(\frac{\Gamma}{2}\right)^2+|\Omega_W|^2}{2\left[\left(\frac{\Gamma}{2}\right)^2+2|\Omega_W|^2\right]}\,, \tag{5.10a}$$

$$\rho^{(1)}_{1a,1a} = \rho^{(1)}_{1b,1b} = 0\,, \tag{5.10b}$$

$$\sigma^{(1)}_{1a,1b} = \Omega_W\Omega^*_{W'}A + \Omega^*_W\Omega_{W'}B\,, \tag{5.10c}$$

$$\sigma^{(2)}_{1a,1b} = \sigma^{(2)}_{1b,1a} = 0\,, \tag{5.10d}$$

$$\rho^{(2)}_{1a,1a} = I + [(\Omega_W\Omega^*_{W'})^2 + (\Omega^*_W\Omega_{W'})^2]J\,, \tag{5.10e}$$

$$\rho^{(2)}_{1b,1b} = K + [(\Omega_W\Omega^*_{W'})^2 + (\Omega^*_W\Omega_{W'})^2]L\,, \tag{5.10f}$$

$$\sigma^{(3)}_{1a,1b} = \Omega_W\Omega^*_{W'}U + \Omega^*_W\Omega_{W'}X + (\Omega_W\Omega^*_{W'})^3\,Y + (\Omega^*_W\Omega_{W'})^3\,Z\,. \tag{5.10g}$$

The quantities A, B, ..., Z, whose full expressions can be found in Appendix A, depend only on the moduli of Ω_W and $\Omega_{W'}$, not contributing to the phase-matching condition. We isolate the $(\Omega_W\Omega^*_{W'})^n$ terms with the phase information $e^{in(\vec{k}_W-\vec{k}_{W'})\cdot\vec{r}}$ outside them. Thus, one can clearly see that for a $\chi^{(2n+1)}$ nonlinearity, the odd terms in n [$\chi^{(3)}$, $\chi^{(7)}$] are stored in the coherence [Eqs. (5.10c) and (5.10g)] and the even terms [$\chi^{(5)}$] are stored in the population [Eqs. (5.10e) and (5.10f)].

Note that there are two terms in each equation of 5.10. The first is in the form $(\Omega_W\Omega^*_{W'})^n$ and the other is its complex conjugate $(\Omega^*_W\Omega_{W'})^n$. The first corresponds to the process described in figure 5.1 where the atoms are absorbing photons from the field W and emitting in the direction of W', whereas the later corresponds to the opposite process, where the atoms are absorbing photons from the field W' and emitting in the direction of W. If the two writing beams have the same intensities (same waist, power, etc.) the two processes are equally probable and physically equivalent. Obviously if one wants to retrieve the signal related to the second process, it is necessary to change the direction of the reading beam and reposition the detector (see figure 5.10). Since we have fixed the direction of the reading beam and the position of the detector, we will only focus on the term related with the process depicted in figure 5.1.

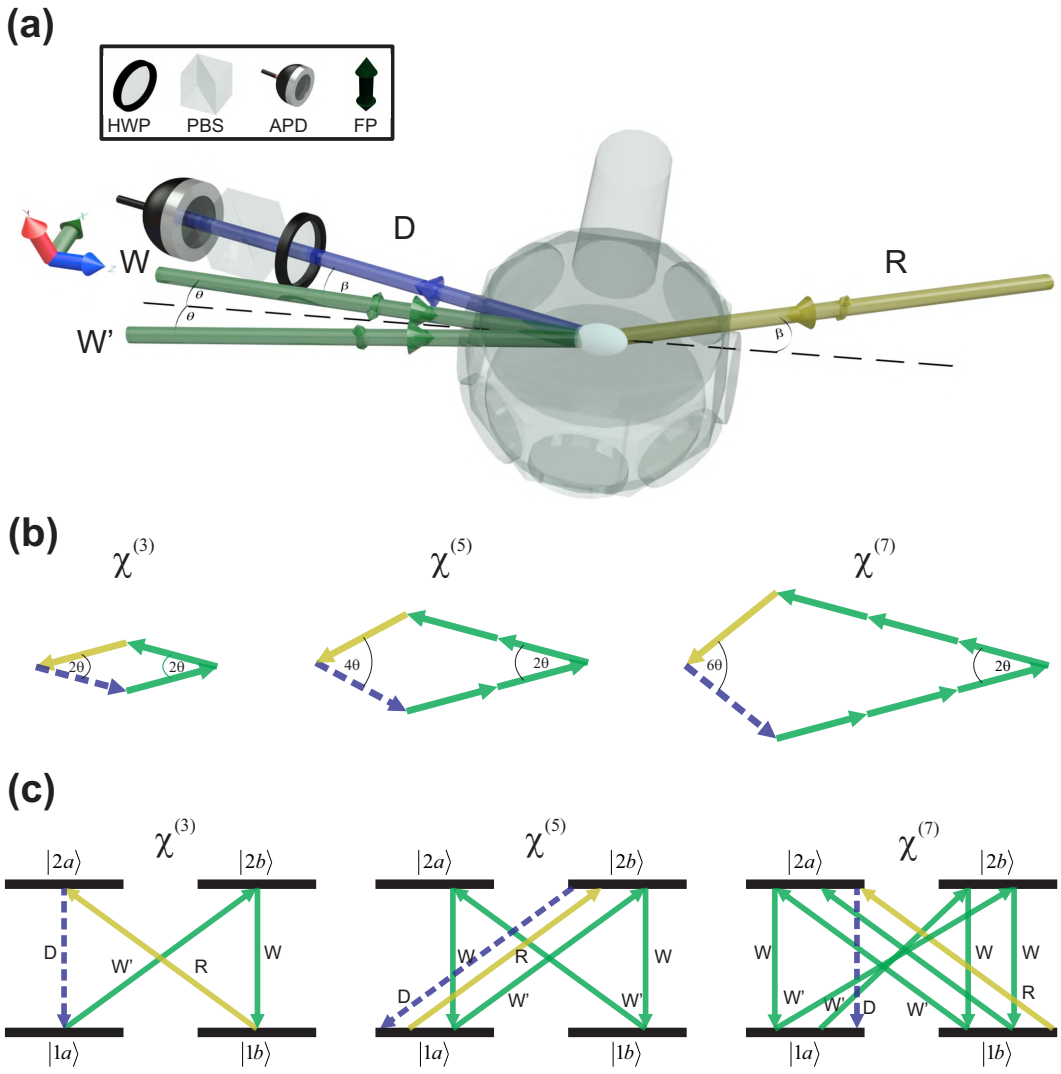

Figure 5.10 Experimental configuration for opposite processes from the figure 5.1.

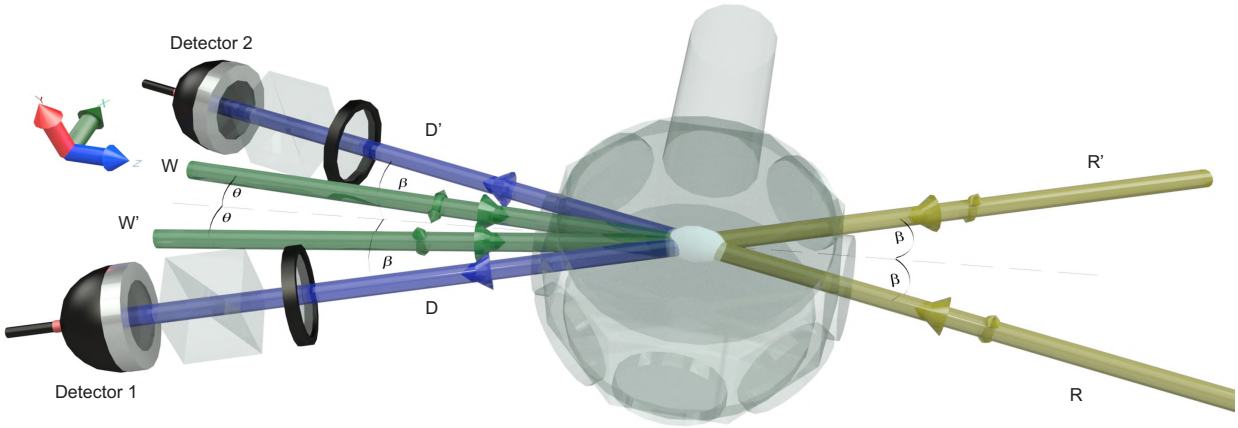

Figure 5.11 Double read. The existence of the two terms $(\Omega_W \Omega_{W'}^*)^n$ and $(\Omega_W^* \Omega_{W'})^n$ in Equation 5.10 creates the possibility of generating two fields, D and D', from the medium if one uses two fields in the read process, R and R'.

The existence of these two terms implies that part of the excitation cannot be fully recovered with a single read field. In other words, part of the information will be in another mode. On the other hand, this also creates an opportunity. If we use two fields in the read process, say R and R', then it is possible to recover two diffracted fields D and D' (see Fig. 5.11). Usually, these two signals are independent [77]. We can point out already here something that we will explain later again. If we use OAM in the write fields, the generated fields will also have OAM. Therefore, if the D has a topological charge $\ell = 1$, then D' will have a topological charge $\ell = -1$ since it is the opposite process in the writing.

Once the writing fields are turned off, the atomic coherences and populations evolve according to their respective decay rates (see Eq. 5.8 with $\Omega_W = \Omega_{W'} = 0$). Therefore, after a time $t \gg \Gamma^{-1}$, all the coherences and populations vanish except the ground-state ones, which are given by

$$\rho_{1a,1a}(t) = \frac{1}{2} + \frac{1}{2}(\rho^{st}_{1a,1a} - \rho^{st}_{1b,1b}) \,, \tag{5.11a}$$

$$\rho_{1b,1b}(t) = \frac{1}{2} - \frac{1}{2}(\rho^{st}_{1a,1a} - \rho^{st}_{1b,1b}) \,, \tag{5.11b}$$

$$\sigma_{1a,1b}(t) = \sigma^{st}_{1a,1b} \,. \tag{5.11c}$$

where $\rho^{st}_{i,j}$ and $\sigma^{st}_{i,j}$ are the steady-state solutions in (5.10). Note that if the system is considered symmetric (equal Clebsh-Gordan coefficients) the ground-state populations would be equal and the phase modulation in them would disappear ($\rho_{1a,1a} = \rho_{1b,1b} = 1/2$). The reason is quite simple. If the system is completely symmetrical, equal Clebsh-Gordan coefficients and decay rates, the beams will create modulations in the four populations that are exactly the same. After the fields are turned off, the populations will decay equally erasing the modulation in the ground-state populations [see Fig.(5.12a)]. An asymmetry is needed either in the excitation, to generate a population difference that would remain even if the decay rates of the excited states were the same [see Fig.(5.12b)], or in the decay rates of the excited states. Note that no decay was considered for the ground-state coherence so far. This will be introduced in the next

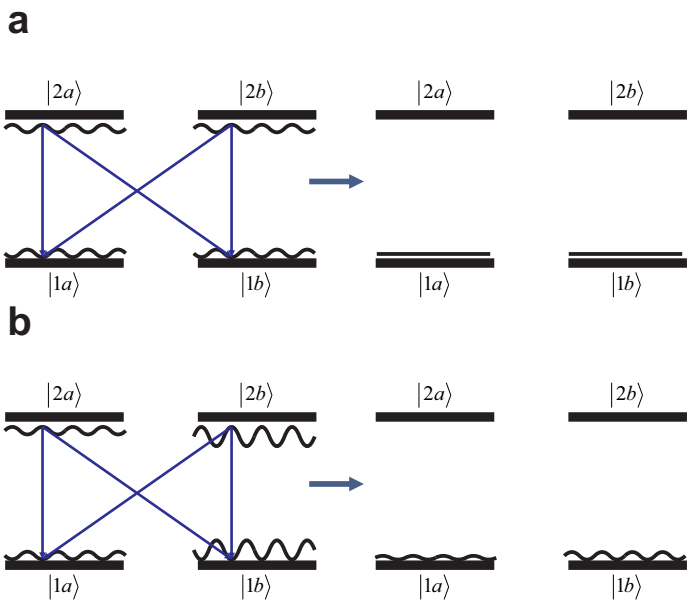

Figure 5.12 (**a**) For a completely symmetrical system, equal Clebsh-Gordan coefficients and decay rates, the beams will create a modulation in the four populations that are exactly the same, but out of phase. After the fields are turned off the populations will decay equally erasing the modulation in the ground-state populations. (**b**) For a non-symmetrical system, different Clebsh-Gordan coefficients, the beams will create a modulations in the four populations that are unbalanced. After the fields are turned off the excited-state populations will decay leaving a modulation in the ground-state populations.

section. It is considered that the magnetic field is well compensated leaving the atomic motion as the most important dephasing process.

5.9.2 Motional dephasing

After formed the gratings, we switch off the fields and the dephasing process starts, i.e., the modulation in Eq. 5.10 starts to be erased. It can be understood as follows. If we ignore collisions, since we are in a low temperature and density regime, the internal states of the atoms (or their spins) remain the same. However, the random motion of the atoms will destroy the modulation imprinted in internal states of the ensemble.

When the write beams are switched off, the population and coherence gratings will be washed out by the ballistic motion of the atoms. If we assume that the atomic velocities obey the Maxwell-Boltzmann distribution, then at a time t the average coherence of the ensemble will be

$$\sigma^{e}_{1a,1b}(r,t) = \frac{1}{\sqrt{\pi}u}\int dv e^{-\frac{v^2}{u^2}}\sigma_{1a,1b}(r-vt,0)\,, \tag{5.12}$$

where $u = \sqrt{\frac{2k_BT}{m}}$ is the most probable speed; m, k_B, and T are the atomic mass, the Boltzmann constant, and the temperature, respectively. Here $\sigma_{1a,1b}$ is the same of Eq. 5.10. The relevant

part of the coherence in the integral is the phase $e^{-in\Delta kvt}$, where $\Delta k = k_W - k_{W'}$ [or $\Delta k = \frac{\pi sin(\theta)}{\lambda}$ as one can deduce from the geometry of Fig. 5.1]. Then, the result of the integral will be proportional to $exp\left[-\frac{(n\Delta k)^2 k_B T t^2}{2m}\right]$. Since the intensity of the retrieved signal is proportional to the square of the optical coherence, then its expression will be proportional to

$$I_D(t) \propto e^{-(\frac{t}{\tau})^2} , \tag{5.13}$$

where $\tau = \frac{1}{(n\Delta k)}\sqrt{\frac{m}{k_B T}}$ is the decay time. One can also write

$$\tau = \frac{\Lambda}{(n\pi)}\sqrt{\frac{m}{k_B T}} , \tag{5.14}$$

where $\Lambda = 2\pi/\Delta k = \frac{\lambda}{2sin\theta}$ is the grating period [78]. For the populations, the calculation is analogous. Note that the grating decay time has angular and order (n) dependences. It is directly proportional to the grating period, which is determined by the angle between the writing beams and the laser wavelength λ, and inversely proportional to n. Therefore, as we increase the order of nonlinearity the storage time decreases, i.e., the $\chi^{(5)}$ decay time should be half of the $\chi^{(3)}$ decay time, and the $\chi^{(7)}$ decay time should be one-third of the $\chi^{(3)}$ decay time.

Knowing these decays is important since if one wants to recover the information stored in the atoms, the delay t_s between the writing and reading fields must be on the order of τ of Eq. 5.14.

5.9.3 Reading

The stored information in Eq. 5.10 is retrieved from the sample through a reading beam R that makes an angle β with the bisectrix between W and W' and has a linear polarization parallel to W', if the decoherence process described in section 5.9.2 has not erased the grating completely. Therefore, the set of Bloch equations (omitting the complex conjugated equations) describing the reading process is obtained in the same way as Eqs. 5.8, substituting $\Omega_{W'}$ by Ω_R and letting $\Omega_W = 0$. The number of equations generated is the same as Eqs. 5.8, but this time they are not all coupled. This natural dissociation bears an important physical meaning: it defines the polarization of the signal and, ultimately, guarantees the existence of a parametric process. This will be detailed shortly. The set of equations can be separated in two systems that are shown in Eqs. 5.15 and 5.16.

System 1

$$\frac{d\rho_{2a,2a}}{dt} = \beta\Omega_R^*\sigma_{2a,1b} + \beta\Omega_R\sigma_{1b,2a} - \Gamma\rho_{2a,2a} , \tag{5.15a}$$

$$\frac{d\rho_{2b,2b}}{dt} = \Omega_R^*\sigma_{2b,1a} + \Omega_R\sigma_{1a,2b} - \Gamma\rho_{2b,2b} , \tag{5.15b}$$

$$\frac{d\rho_{1a,1a}}{dt} = -\Omega_R^*\sigma_{2b,1a} - \Omega_R\sigma_{1a,2b} + \frac{\Gamma}{2}(\rho_{2a,2a} + \rho_{2b,2b}) , \tag{5.15c}$$

$$\frac{d\rho_{1b,1b}}{dt} = -\beta\Omega_R^*\sigma_{2a,1b} - \beta\Omega_R\sigma_{1b,2a} + \frac{\Gamma}{2}(\rho_{2a,2a} + \rho_{2b,2b}) , \tag{5.15d}$$

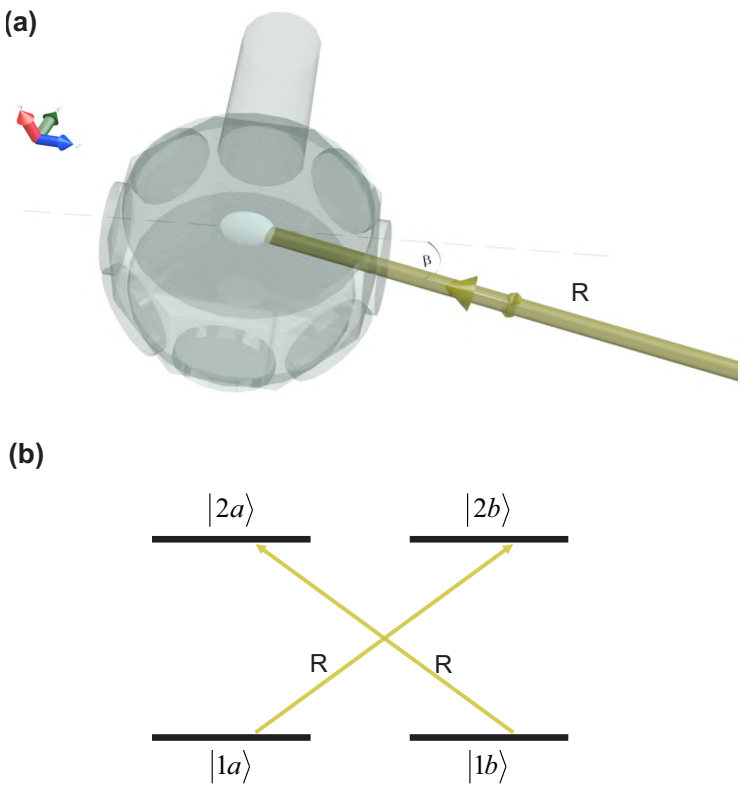

Figure 5.13 (**a**) The cold sample inside the cell is irradiated by the reading field R with orthogonal linear polarizations and forming an angle β between them. (**b**) Coupling of the writing fields with the internal states of the atom.

$$\frac{d\sigma_{1a,2b}}{dt} = \Omega_R^* \rho_{1a,1a} - \Omega_R^* \rho_{2b,2b} - \left(\frac{\Gamma}{2} + i\Delta\right)\sigma_{1a,2b}\ , \tag{5.15e}$$

$$\frac{d\sigma_{1b,2a}}{dt} = -\beta\Omega_R^* \rho_{2a,2a} + \beta\Omega_R^* \rho_{1b,1b} - \left(\frac{\Gamma}{2} + i\Delta\right)\sigma_{1b,2a}\ . \tag{5.15f}$$

System 2

$$\frac{d\sigma_{1a,2a}}{dt} = \beta\Omega_R^* \sigma_{1a,1b} - \Omega_R^* \sigma_{2b,2a} - \left(\frac{\Gamma}{2} + i\Delta\right)\sigma_{1a,2a}\ , \tag{5.16a}$$

$$\frac{d\sigma_{1b,2b}}{dt} = -\beta\Omega_R^* \sigma_{2a,2b} + \Omega_R^* \sigma_{1b,1a} - \left(\frac{\Gamma}{2} + i\Delta\right)\sigma_{1b,2b}\ , \tag{5.16b}$$

$$\frac{d\sigma_{1a,1b}}{dt} = -\beta\Omega_R \sigma_{1a,2a} - \Omega_R^* \sigma_{2b,1b}\ , \tag{5.16c}$$

$$\frac{d\sigma_{2a,2b}}{dt} = \Omega_R^* \sigma_{2a,1a} + \beta\Omega_R \sigma_{1b,2b} - \Gamma\sigma_{2a,2b}\ . \tag{5.16d}$$

The optical coherences $\sigma_{1a,2b}$ and $\sigma_{1b,2a}$ are coupled with the populations, whereas $\sigma_{1a,2a}$ and $\sigma_{1b,2b}$ are coupled only with the ground-state and excited-state coherences. This implies that the signal generated from the population grating will always have a polarization parallel to the reading beam and the one from the coherence grating will be always orthogonal to it. If one considers that the atom starts in the $|1a\rangle$ level, it will end in the $|1b\rangle$ after an odd number of interactions with the writing fields, and in the same $|1a\rangle$ for an even number of interactions [see Fig. (5.1c)]. The ground-state coherence stores the first type of interaction, whereas the ground-state populations store the second, as we have seen above. Thus, for the two kinds of signal, the atom returns to the initial state $|1a\rangle$ after emitting the D field. We have chosen the reading beam with a polarization parallel to W'. However, for the orthogonal case, the process is analogous. In such a case, the populations would be coupled with $\sigma_{1a,2a}$ and $\sigma_{1b,2b}$, and the ground-state coherence with $\sigma_{1a,2b}$ and $\sigma_{1b,2a}$. Therefore, independently of the reading beam polarization (as long as it remains linear), the atom will always end where it started in the first place. This means that the angular momentum is conserved in the whole process. Finally, it is noteworthy that if the reading field polarization is parallel to the W' field, just a three-level system is necessary to explain the $\chi^{(3)}$ process [Fig. (5.1c)]. The other orders still need at least a four-level system. However, for a reading field polarization parallel to W a four-level system is required for all three orders.

The retrieved pulse shape is obtained by finding the atomic dipole moment induced by the reading field, solving the two systems above, and using them as a polarization source term in Maxwell's equation, as we did in chapter 3. The polarization expression is found by considering that the read field will induce a dipole moment $\vec{p}$ in each atom. We calculate this dipole moment considering its mean value $\langle\vec{p}\rangle$ [79]. Each dipole moment will add up, producing a macroscopic polarization $\mathbf{P}$, associated with N atoms of the ensemble in a volume V, given by

$$\boldsymbol{P} = \frac{N}{V}\langle\boldsymbol{p}\rangle\ . \tag{5.17}$$

where $\nu = \frac{N}{V}$ is the atomic density. For the $\chi^{(5)}$ process the dipole moments will be associated with $\sigma_{1a,2a}$ and $\sigma_{1b,2b}$, which yields

$$\begin{aligned} \boldsymbol{P} &= \frac{N}{V}\langle \boldsymbol{p} \rangle \\ &= \nu \left(d_{1a,2a}\rho_{1a,2a} + d_{1b,2b}\rho_{1b,2b} + c.c. \right) , \end{aligned} \tag{5.18}$$

while for the $\chi^{(3)}$ and $\chi^{(7)}$ processes the dipole moments will be associated with $\sigma_{1a,2b}$ and $\sigma_{1b,2a}$, which yields

$$\begin{aligned} \boldsymbol{P} &= \frac{N}{V}\langle \boldsymbol{p} \rangle \\ &= \nu \left(d_{1a,2b}\rho_{1a,2b} + d_{1b,2a}\rho_{1b,2a} + c.c. \right) . \end{aligned} \tag{5.19}$$

Naturally, we still need to solve the systems 1 (Eq. 5.15) and 2 (Eq. 5.16) to find the polarization expression. This time we are not looking for the steady-state solution but the full temporal evolution of the optical coherences. The differential homogeneous linear system with constant coefficients can be solved numerically using the fourth-order Runge-Kutta method [80]. Assuming that the sample is thin and that the absorption of the D field can be neglected, one finds that the temporal envelope $\mathscr{E}_D(z',t)$ is proportional to the induced optical polarization.

$$\mathscr{E}_D(z',t) \propto P . \tag{5.20}$$

5.10 Results and discussions

This section is devoted to present, analyze and compare the measurements with the theoretical model of section 5.9.1. The polarization of each retrieved signal depends on the order being explored, as anticipated by the theoretical model. Thus, referring to the experimental scheme depicted in Fig. (5.1a), we have first analyzed the polarization of the retrieved beam with the *PBS* and an *HWP* optical components. The $\chi^{(3)}$ and $\chi^{(7)}$ retrieved pulses associated with the coherence grating have polarizations orthogonal to the R beam. The relative ratio between the parallel and orthogonal components for each signal is about 1 : 300 and 1 : 100 for the $\chi^{(3)}$ and $\chi^{(7)}$, respectively. For the $\chi^{(5)}$ the main component is parallel, with a ratio also around 1 : 100.

5.10.1 Writing

As the first set of results, we investigate the dependence of the retrieved signal with the writing fields intensities, since the whole nonlinearity is in the writing process. In Fig. 5.14 we show the dependence of the retrieved signal peak amplitude as a function of the W' field intensity for fixed intensities of the fields W and R (respectively equal to $I_W = 32$ mW/cm^2 and $I_R = 691$ mW/cm^2). According to the phase-matching condition, one can separate the different contributions by isolating the terms $\Omega_W\Omega^*_{W'}$, $\left(\Omega_W\Omega^*_{W'}\right)^2$ and $\left(\Omega_W\Omega^*_{W'}\right)^3$. The first term, in the low-intensity limit, represents the $\chi^{(3)}$ process, the second, the $\chi^{(5)}$ process, and the third, the $\chi^{(7)}$ process, respectively. Therefore, we should expect, for low intensities, a linear, quadratic,

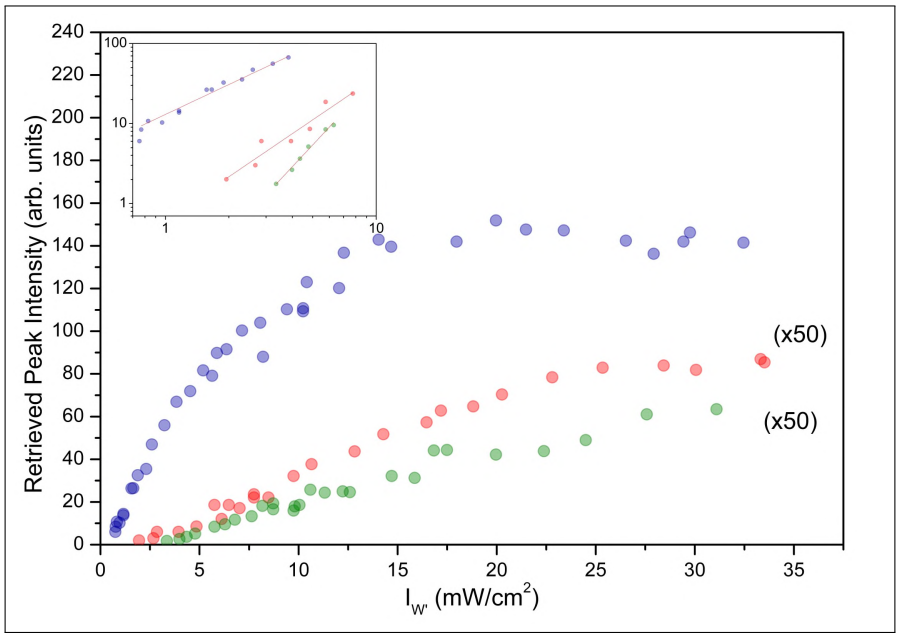

Figure 5.14 Dependence of the retrieved signal peak amplitude with the intensity of W' with fixed W ($I_W = 32$ mW/cm^2) and R ($I_R = 691$ mW/cm^2) intensities, and $\Delta_W = \Delta_{W'} = \Delta_R = 0$. The experimental data for $\chi^{(3)}$, $\chi^{(5)}$, and $\chi^{(7)}$ are represented by the blue, red, and green circles, respectively. The beginning of the curve in log-log scale is shown in the inset. The slope associated with each fitting is 1.2 ± 0.1, 1.8 ± 0.2, and 2.8 ± 0.1 for $\chi^{(3)}$, $\chi^{(5)}$, and $\chi^{(7)}$, respectively.

and cubic dependence for the $\chi^{(3)}$, $\chi^{(5)}$, and $\chi^{(7)}$ signals, respectively. In the inset of Fig. 5.14 we plot the retrieved signal as a function of the intensity of W', in the low intensity regime, with fixed W intensity in the log-log scale. The slope associated with each fitting is 1.2 ± 0.1, 1.8 ± 0.2, 2.8 ± 0.1 for $\chi^{(3)}$, $\chi^{(5)}$, and $\chi^{(7)}$, respectively. This is close to the expected values of 1, 2, and 3, since the atoms interact once, twice, and three times with the W' field in the $\chi^{(3)}$, $\chi^{(5)}$, and $\chi^{(7)}$ processes, respectively. For the complete curve, not only for low intensities, one should see also a fairly distinct behavior between the different orders. Each order saturates at different intensities, with the lower ones saturating first.

5.10.2 Reading

Theoretically it is expected only two kinds of pulse shapes: one arising from the population grating (System 1 of the reading Eq. 5.15) and other from the coherence grating (System 2 of the reading Eq. 5.16). Despite of this, the experiment shows a different behavior. With the reading beam in resonance, each order presents its particular pulse shape as one can see from Fig. (5.15a). These discrepancies, however, are a consequence of the fact that we considered the sample to be sufficiently thin to neglect propagation effects. Therefore, we cannot compare the pulses observed in resonance directly with our theoretical model, since propagation effects can alter significantly the pulse shapes in this situation [81]. However, off resonance, the propagation effects should be mitigated, and a better comparison could be achieved. Indeed, Fig. (5.15b) shows the results for $\Delta_R = 30$ MHz, where one can see that the $\chi^{(3)}$ and $\chi^{(7)}$ have

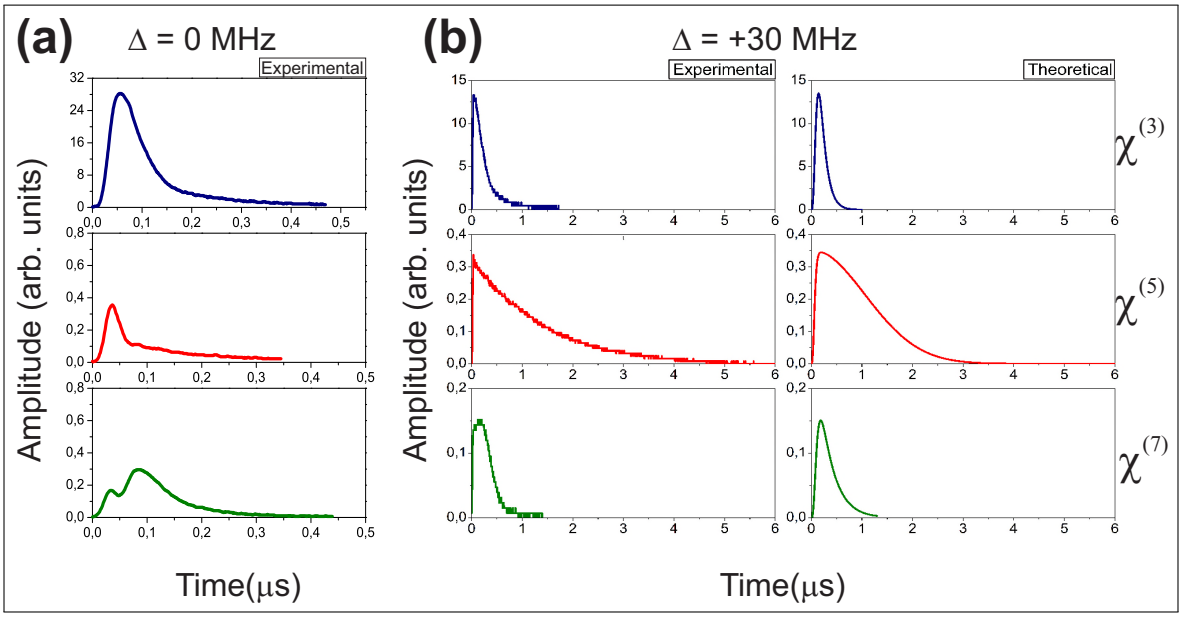

Figure 5.15 Experimental and theoretical pulse shapes of the retrieved signal. The blue, red and green pulse shapes correspond to the $\chi^{(3)}$, $\chi^{(5)}$ and $\chi^{(7)}$ orders, respectively. (**a**) Experimental pulses for a resonant reading beam. The experimental intensities and detunings are $I_R = 170$ mW/cm^2, $I_W = 148$ mW/cm^2, $I_{W'} = 122$ mW/cm^2 and $\Delta_R = \Delta_W = \Delta_{W'} = 0$ MHz for all pulses. (**b**) The experimental (first column) and the theoretical (second column) pulse shapes of the retrieved signal, for a non-resonant reading beam, for each order of nonlinearity. The theoretical pulses were obtained numerically. The used parameters for the numerical calculation were $\Omega_R = 0.12\Gamma$, $\Omega_R = 0.25\Gamma$, and $\Omega_R = 0.1\Gamma$ for $\chi^{(3)}$, $\chi^{(5)}$, and $\chi^{(7)}$, respectively, where $\Gamma/2\pi = 5.2$ MHz. The experimental intensities and detunings are $I_R = 170$ mW/cm^2, $I_W = I_{W'} = 148$ mW/cm^2, $\Delta_W = \Delta_{W'} = 0$ MHz, and $\Delta_R = 30$ MHz for all pulses.

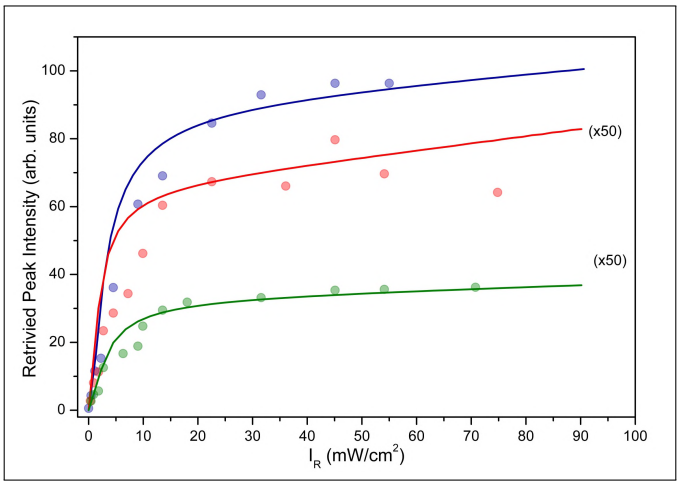

Figure 5.16 Dependence of the retrieved signal with the intensity of R with fixed W and W' intensities. The experimental data for $\chi^{(3)}$ (blue), $\chi^{(5)}$ (red), and $\chi^{(7)}$ (green) are represented by the circles, while the theoretical fits are represented by the solid curves. The other intensities and detunings are $I_W = 76$ mW/cm^2, $I_{W'} = 74$ mW/cm^2, and $\Delta_{W'} = \Delta_W = \Delta_R = 0$ MHz.

more similar pulse shapes, but significantly different from the $\chi^{(5)}$ case. However, since the $\chi^{(3)}$ and $\chi^{(7)}$ pulse shapes shown in Fig. (5.15b) are not exactly the same, even though they are similar, one can suppose that another process may be also involved. The Rabi frequencies employed in the numerical calculations ($\Omega_R = 0.12\Gamma$, $\Omega_R = 0.25\Gamma$, and $\Omega_R = 0.1\Gamma$ for $\chi^{(3)}$, $\chi^{(5)}$, and $\chi^{(7)}$, respectively) of Fig. (5.15b) are satisfactory when compared to the estimated experimental Rabi frequency of $\Omega_R = 0.8\Gamma$ for an average saturation intensity of the transition of approximately $I_s = 3.5$ mW/cm^2. The corresponding retrieved pulses were obtained for a fixed storage time $t_s = 500$ ns. In other words, we turn on the reading field 500 ns after we turn off the writing fields and recover the pulses of Fig. 5.15. In the theoretical pulses the field was multiplied by $e^{-(\frac{t}{\tau})^2}$ to include the grating wash-out.

We plot in Fig. 5.16 the experimental and theoretical maximum retrieved-signal amplitude for each order as a function of the intensity of the reading beam R for fixed intensities of the writing beams. The numerical parameters used for the simulation are given in the figure caption. The difference between the experimental and numerical parameters are most likely due to the simplifications in the model. Differently from the case of the writing beams, all the orders, in the low intensity regime, have the same linear dependence with the reading beam intensity. If we plot the same intensity dependence in a logarithmic scale in the low-intensity limit, the measured slopes are 0.8 ± 0.1, 1.0 ± 0.1, and 0.9 ± 0.2 for $\chi^{(3)}$, $\chi^{(5)}$, and $\chi^{(7)}$, respectively.

5.10.3 Memory Lifetime

Finally, we have investigated the memory lifetime for each nonlinear order. Differently from the previous measurements, where we read at the same time (around 500 ns after the writing fields turn off), here we keep the same duration of the reading pulse, but we vary its delay t_s in 500 ns steps (see Fig. 5.17) recovering a pulse with a smaller amplitude. The peak intensity of each pulse is plotted in Fig. 5.4.

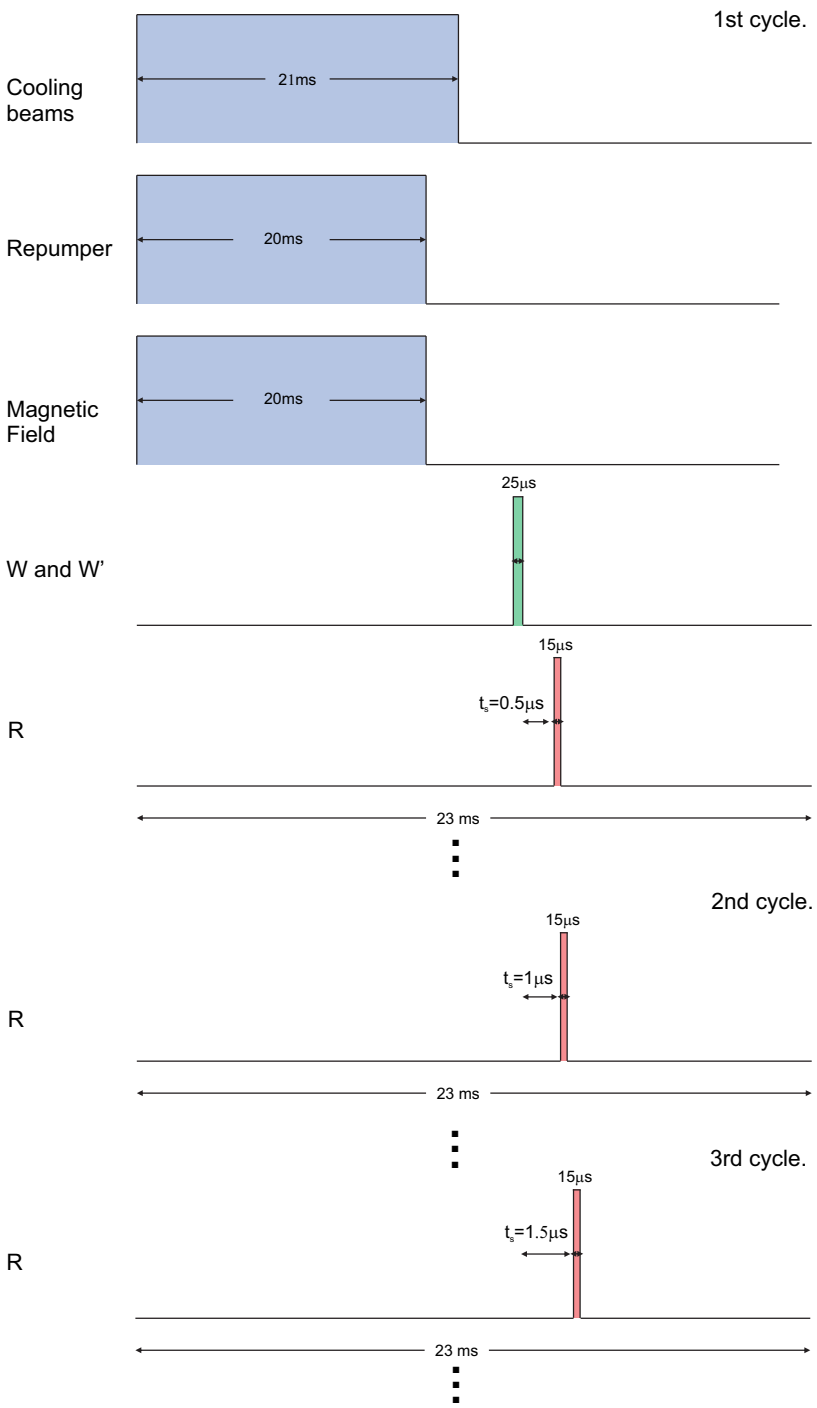

Figure 5.17 Experiment pulse sequence varying for measuring the storage time. As before, the cooling beam stays on during 21ms, while the repumper and the magnetic field are on during 20 ms. After that the write beam is switched on for 25 μs imprinting the phase information in the medium. The reading beam pulse is switched on at a time t_s after the writing fields switch off for 15 μs recovering a signal. At each cycle, we read at a different time t_s (increased in 500 ns steps) recovering a pulse with a smaller amplitude.

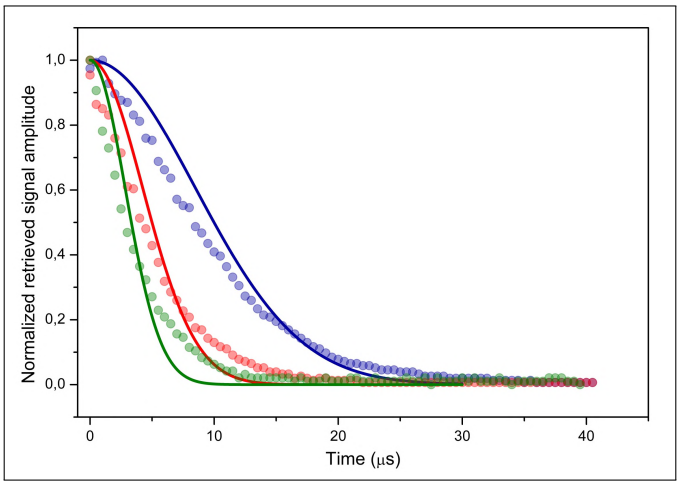

Figure 5.18 Normalized retrieved signal amplitude for different storage times. The blue, red, and green circles correspond to the data points of $\chi^{(3)}$, $\chi^{(5)}$, and $\chi^{(7)}$, respectively. The decay predicted for each order, as described in the text, is represented by the solid curves with the same colors as the data points. The theoretical parameters are $\tau = 12\mu$s, $\tau = 6\mu$s, and $\tau = 4\mu$s, for $\chi^{(3)}$, $\chi^{(5)}$ and $\chi^{(7)}$, respectively. Experimental intensities and detunings are $I_{W'} = I_W = 148$ mW/cm^2, $I_R = 679$ mW/cm^2, $\Delta_{W'} = \Delta_W = 0$, and $\Delta_R = 15$ MHz.

As expected and emphasized in the theoretical section, the main dephasing process is due to atomic motion. Since the period of each grating associated with the nonlinear term $\chi^{(2n+1)}$ is given by $\Lambda_n = 2\pi/n\Delta k$, it follows that each order has a different grating period. Atomic motion along the direction normal to the grating planes tends to "blur" in a scale of time proportional to the time taken by the atom to travel a distance on the order of the grating period. As a consequence, the smaller the period, the faster will be the decay. And since the spatial period decreases with n, the lifetime decreases as the order of nonlinearity increases. More specifically, the lifetime of the $\chi^{(5)}$ and $\chi^{(7)}$ are half and one-third of the $\chi^{(3)}$, respectively. In Fig. 5.18 we show the decay of the peak intensity of the D pulse signal for different storage times. We fitted the experimental curves by a Gaussian curve $e^{-\left(\frac{t}{\tau}\right)^2}$, with the theoretical parameters $\tau = 12\mu$s, $\tau = 6\mu$s, and $\tau = 4\mu$s, for $\chi^{(3)}$, $\chi^{(5)}$ and $\chi^{(7)}$, respectively.

There are a few approaches which should allow to suppress the dephasing by thermal motion of the atoms such as, for instance, by employing an optical lattice to restrain atomic motion in the grating direction [75, 82]. Another idea is to simply erase the phase information after switching off the writing fields. This was proposed in [83] for single photons in the DLCZ protocol context.

5.11 Manipulation of Orbital Angular Momentum of Light

So far we have focused on the mechanisms of information storage. However, we can show that this memory capability goes beyond the simple storage of information. In this section we would like to present an important concept of the nonlinear memory related to its capacity of

not only store but also manipulate the information stored.

5.12 Experimental set up

The experimental set up is basically the same as the one presented in section 5.2 with two small changes. The first change is the inclusion of two independent spatial light modulators (SLMs) to shape the writing beams W and W' as Laguerre–Gauss (LG) modes, as shown in Fig.5.19. These SLMs are voltage-controlled liquid crystals that can change the phase of light without altering the intensity or the polarization of the incoming field. Thus we modulate the wavefront of a light beam to generate LG modes.

The second change is the insertion of a CCD camera (Thorlabs DCC3240N) paired with a lens in the second port of the beam splitter (Fig.5.19) to record the intensity profile of the generated beam. The camera has a triggered mode and it is sensitive to nanowatts of light. This is important since our signals are pulses of a few hundreds nanowatts in a few hundreds of nanoseconds, or a few microseconds in the case of the $\chi^{(5)}$ (see Fig.5.15). The importance of the lens is explained in section 5.12.1.

5.12.1 Characterization of the topological charge

The topological charge is measured using the tilted lens method [84]. Several methods used to measure the charge are based on interferometry [85]. However, they can be very complex. Moreover, the interference pattern can be easily affected by misalignment, making the practical utilization of these techniques in the lab quite cumbersome. Other approaches using the far field diffraction pattern are not adequate for measuring higher topological charges [86]. The tilted lens on the other hand is an incredibly simple but extremely robust technique that allows to measure not only integer values of ℓ but fractional values, and mixed values (i.e. a beam that contains several components with different values of topological charges) as well [87].

The optical vortex with a topological charge ℓ exhibits a self-interference pattern after passing through an astigmatic optical element, with ℓ inclined nodes whose orientations are determined by the sign of the charge. In Fig.5.20, experimental images are shown for vortices with and without the lens. The clockwise rotated pattern has a positive sign, whereas the counter-clockwise has a negative sign.

5.13 Theoretical Model for OAM

The theoretical model follows the exact same idea of the one presented in section 5.9 with a small change. Since the fields can be in Laguerre-Gauss modes other than the fundamental ($\ell = 0$) Gaussian mode, we must include that in the expression for the electromagnetic field. Instead of using the equations 5.2, we must use the expression for a Laguerre-Gauss beam, which can be written as

$$u(r,\phi,z) = \mathscr{E}_W(\vec{r},t)e^{i(k_W z-\omega_W t)}e^{i\phi l} \ . \tag{5.21}$$

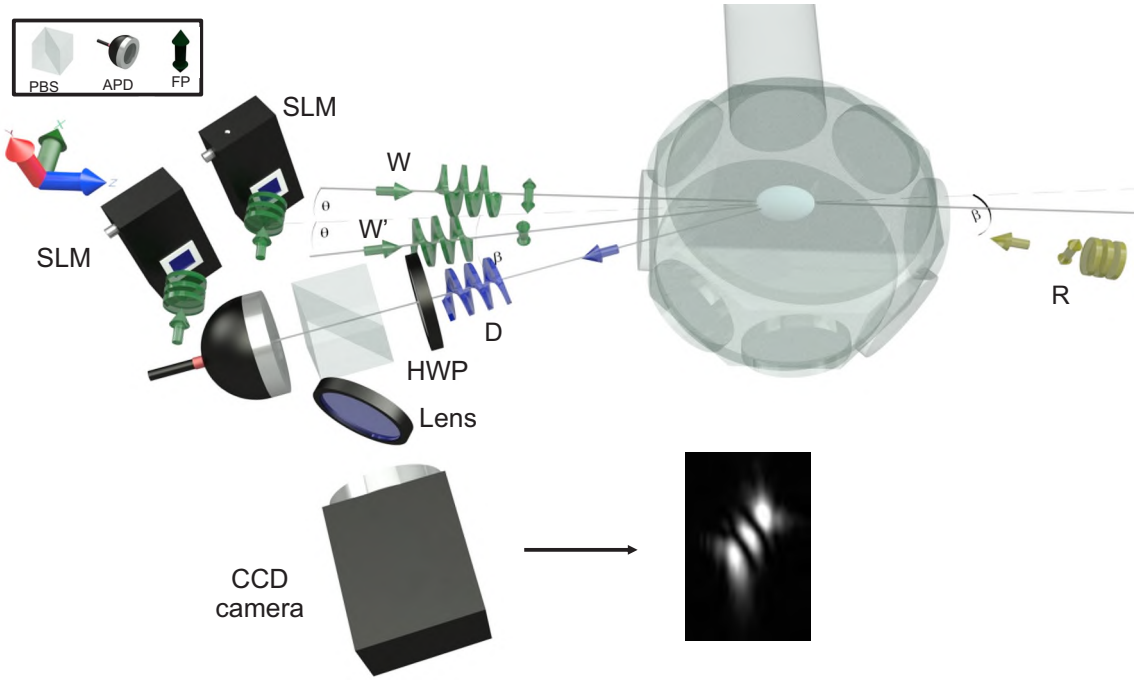

Figure 5.19 Simplified experimental configuration for generation of nonlinear atomic memories with OAM states. (**a**) The cold sample inside the cell is irradiated by two writing beams W and W', forming an angle 2θ between them, generating the population and coherence gratings. Two independent spatial light modulators (SLMs) shape the writing beams W and W' as Laguerre–Gauss (LG) modes, carrying topological charges ℓ_W and $\ell_{W'}$ for W and W', respectively. A Gaussian reading beam R selects the order of nonlinearity by choosing the angle β with the bisectrix between W and W'. The field polarization (FP) of the retrieved signal D is analyzed with a polarizing beam splitter (PBS), a half wave-plate (HWP), and an avalanche photodetector (APD). A CCD camera and a tilted lens measure the topological charge.

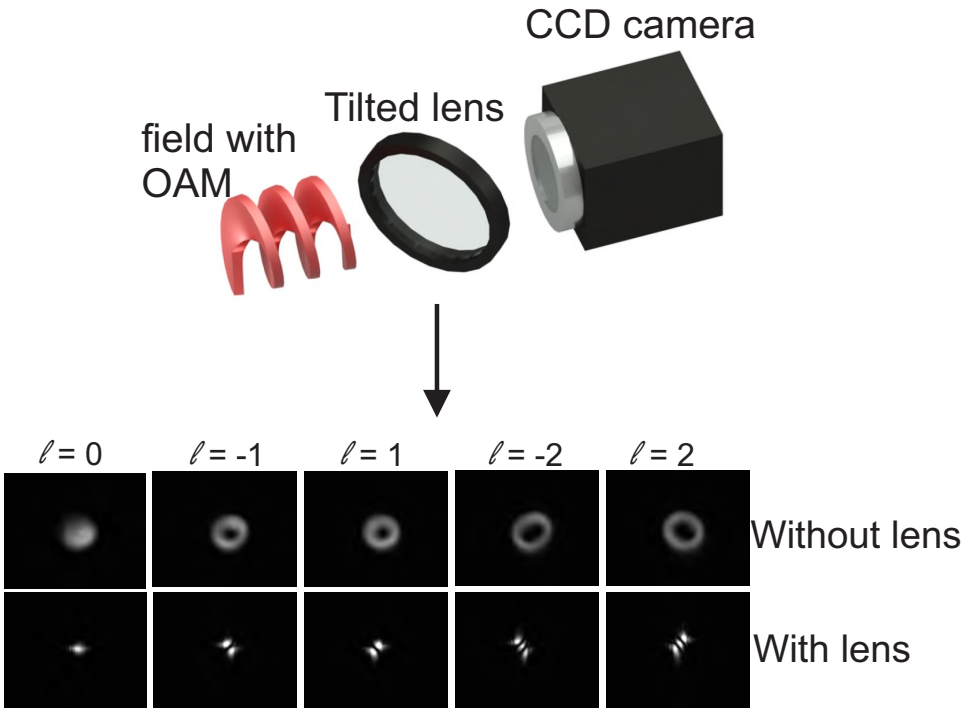

Figure 5.20 Tilted lens technique. The optical vortex with a topological charge ℓ exhibits a self-interference pattern after passing through an astigmatic optical element with ℓ inclined nodes whose orientation determines the sign of the charge. The first and second rows show experimental images for vortices without and with the lens, respectively.

Therefore the writing fields can be written as

$$\vec{E}_W = \frac{1}{2}[\mathscr{E}_W(\vec{r},t)e^{i(k_W z-\omega_W t)}e^{-i\phi\ell} + \mathscr{E}^*_W(\vec{r},t)e^{-i(k_W z-\omega_W t)}e^{i\phi l}]\hat{x}\,, \tag{5.22a}$$

$$\vec{E}_{W'} = \frac{1}{2}[\mathscr{E}_{W'}(\vec{r},t)e^{i(\vec{k}_{W'}\cdot\vec{r}-\omega_{W'}t)}e^{-i\phi l} + \mathscr{E}^*_{W'}(\vec{r},t)e^{-i(\vec{k}_{W'}\cdot\vec{r}-\omega_{W'}t)}e^{i\phi l}]\hat{y}\,, \tag{5.22b}$$

where again $\mathscr{E}_i(\vec{r},t)$ is the electric field envelope of beam $i(i = W, W')$. The Rabi frequency also must be redefined as

$$\Omega_j(\vec{r},t) = \frac{id_j\mathscr{E}_j(\vec{r},t)e^{i\vec{k}_j\cdot\vec{r}}e^{i\phi\ell}}{4\hbar} \tag{5.23}$$

The rest of the calculation is exactly the same as in section 5.9 and is not fully reproduced here. The steady-state solutions, in all orders in the W field and in first, second, and third order in the W' field for the coherence and populations are (as in Eq. 5.10)

$$\rho^{(0)}_{1a,1a} = \rho^{(0)}_{1b,1b} = \frac{\left(\frac{\Gamma}{2}\right)^2 + |\Omega_W|^2}{2\left[\left(\frac{\Gamma}{2}\right)^2 + 2|\Omega_W|^2\right]}\,, \tag{5.24a}$$

$$\rho^{(1)}_{1a,1a} = \rho^{(1)}_{1b,1b} = 0\,, \tag{5.24b}$$

$$\sigma^{(1)}_{1a,1b} = \Omega_W\Omega^*_{W'}A + \Omega^*_W\Omega_{W'}B\,, \tag{5.24c}$$

$$\sigma^{(2)}_{1a,1b} = \sigma^{(2)}_{1b,1a} = 0\,, \tag{5.24d}$$

$$\rho^{(2)}_{1a,1a} = I + [(\Omega_W\Omega^*_{W'})^2 + (\Omega^*_W\Omega_{W'})^2]J\,, \tag{5.24e}$$

$$\rho^{(2)}_{1b,1b} = K + [(\Omega_W\Omega^*_{W'})^2 + (\Omega^*_W\Omega_{W'})^2]L\,, \tag{5.24f}$$

$$\sigma^{(3)}_{1a,1b} = \Omega_W\Omega^*_{W'}U + \Omega^*_W\Omega_{W'}X + (\Omega_W\Omega^*_{W'})^3Y + (\Omega^*_W\Omega_{W'})^3Z\,. \tag{5.24g}$$

As previuosly, the quantities A, B, ..., Z, whose full expressions can be found in Appendix A, depend only on the moduli of Ω_W and $\Omega_{W'}$, not contributing to the phase-matching condition. Using the new Rabi frequency definition in Eq. 5.23, one can clearly see that for the $\chi^{(3)}$ terms we have

$$(\Omega_W\Omega^*_{W'}) \propto e^{-i\phi(\ell_{W'}-\ell_W)}\,, \tag{5.25}$$

for the $\chi^{(5)}$ terms we have

$$(\Omega_W\Omega^*_{W'})^2 \propto e^{-2i\phi(\ell_{W'}-\ell_W)}\,, \tag{5.26}$$

and for the $\chi^{(7)}$ terms we have

$$(\Omega_W\Omega^*_{W'})^3 \propto e^{-3i\phi(\ell_{W'}-\ell_W)}\,. \tag{5.27}$$

Therefore, we can conclude that the topological charge of the retrieved beam after the reading process has the values of $-(\ell_{W'}-\ell_W)$, $-2(\ell_{W'}-\ell_W)$, and $-3(\ell_{W'}-\ell_W)$ for the $\chi^{(3)}$, $\chi^{(5)}$, and $\chi^{(7)}$ processes, respectively. Again, as explained in section 5.9.1 this is valid for the terms related to the process where photons are absorbed from W and stimulatedly emitted in W'. In

this process when the atom absorbs a photon from the field W it gains a phase $e^{i\phi\ell_W}$, and when it emits a photon in the same mode as W', it gains a phase $e^{-i\phi\ell_{W'}}$. For the opposite process, we have obviously the contrary, and the topological charge of the retrieved beam after the reading process has the values of $(\ell_{W'}-\ell_W)$, $2(\ell_{W'}-\ell_W)$, and $3(\ell_{W'}-\ell_W)$ for the $\chi^{(3)}$, $\chi^{(5)}$, and $\chi^{(7)}$ processes, respectively.

Now we come back to the discussion of using two read fields initiated at the end of section 5.9.1. If we attempt to read the grating related to the process for which we have absorption in mode W (and emission in W') and the other related to the process for which we have stimulated emission in mode W (and absorption in W'), we may generate correlated beams with opposite charges. Therefore, if the D has a topological charge ℓ, then D' will have a topological charge $-\ell$ since it is the opposite process in the writing.

All our results were taken with a single read field. We shall concentrate on the first process (absorption in W) and therefore position the camera accordingly.

5.14 Results with OAM

Two sets of measurements have been implemented. In the first, we set the SLM in the W beam to generate a fundamental Gaussian mode ($\ell_W = 0$), while W' can carry arbitrary values of OAM. In the second, both writing beams can have arbitrary topological charges ($\ell_W, \ell_{W'} \neq 0$). The reading field is a regular Gaussian beam with null charge ($\ell_R = 0$) throughout all the measurements.

In the first case, we store and retrieve the topological charge of the W' beam up to $\ell_{W'} = \pm 2$, namely $\ell_{W'} = -2,-1,0,+1,+2$, whereas $\ell_W = 0$ for the W beam. Figure (5.21b) shows the measured topological charge of the retrieved beam for different pairs $(\ell_{W'}, \ell_W)$ for each order of non-linearity. For the $\chi^{(3)}$ process the output is always equal to the input. However, for the $\chi^{(5)}$ and $\chi^{(7)}$ the charge doubles and triples, respectively. The retrieved charge has a negative sign since in this process when the atom emits a photon on mode W', it gains a phase $e^{-i\phi\ell_{W'}}$.

We have also analyzed the opposite situation where W' is in the fundamental Gaussian mode ($\ell_{W'} = 0$) and W has a non-vanishing topological charge. This is illustrated in Fig. (5.21c). Note that the retrieved charge has the opposite sign of Fig. (5.21b), since in this process when the atom absorbs a photon from field W, it gains a phase $e^{i\phi\ell_W}$.

In the second case both W, W' may have different OAM states, namely $\ell_W = -2,-1,0,+1,+2$ and $\ell_{W'} = -2,-1,0,+1,+2$. Fig. 5.22 shows the measured topological charge of the retrieved beam for different pairs $(\ell_{W'}, \ell_W)$ for each order of non-linearity. Again, as before, for the $\chi^{(3)}$ process the output is always equal to the input and for the $\chi^{(5)}$ and $\chi^{(7)}$ the charge doubles and triples, respectively. As stated before, the topological charge of the retrieved beam after the reading process has the value of $(\ell_{W'}-\ell_W)$, $2(\ell_{W'}-\ell_W)$, and $3(\ell_{W'}-\ell_W)$ for the $\chi^{(3)}$, $\chi^{(5)}$, and $\chi^{(7)}$ processes, respectively. This allows one to perform algebraic operations like subtraction, addition and multiplication by factors of 1, 2 and 3 (see Fig. 5.22).

For example, for $(\ell_{W'}, \ell_W) = (1,-1)$ input, we would have an output charge of 2, 4, and 6 for the $\chi^{(3)}$, $\chi^{(5)}$, and $\chi^{(7)}$, respectively. If the beam W' was your signal arriving from any communication system, you could see this process as storage and manipulation of your original signal, where the W beam would be the responsible for the manipulation coupled with

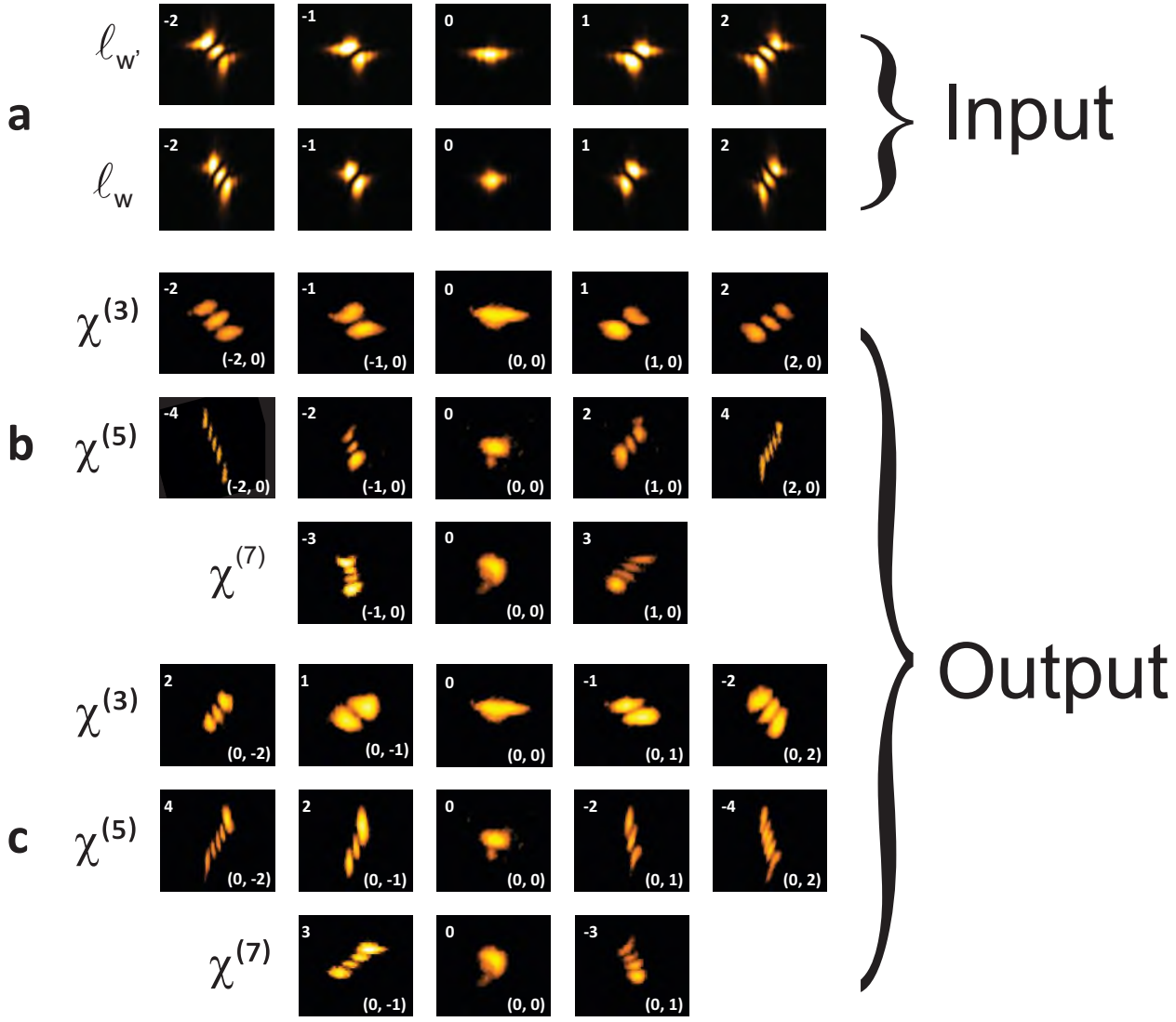

Figure 5.21 Input and output states of OAM in the case where one writing field is in the fundamental Gaussian mode and the other has a non-vanishing topological charge for the $\chi^{(3)}$, $\chi^{(5)}$, and $\chi^{(7)}$ memories. (a) Self-interference pattern of the incident writing beams $W(\ell_W)$ and $W'(\ell_{W'})$ after passing through a tilted stigmatic lens, evidencing the topological charge of each beam. (b), (c) Retrieved topological charges in the case where the topological charges of writing beams W and W' are, respectively, equal to (b) $\ell_{W'} = -2;-1;0;+1;+2$ and $\ell_W = 0$ and (c) $\ell_{W'} = 0$ and $\ell_W = -2;-1;0;+1;+2$. The values of the pair $(\ell_{W'}, \ell_W)$ and the values of the retrieved topological charges are indicated, respectively, in the bottom-right and top-left corners of each frame.

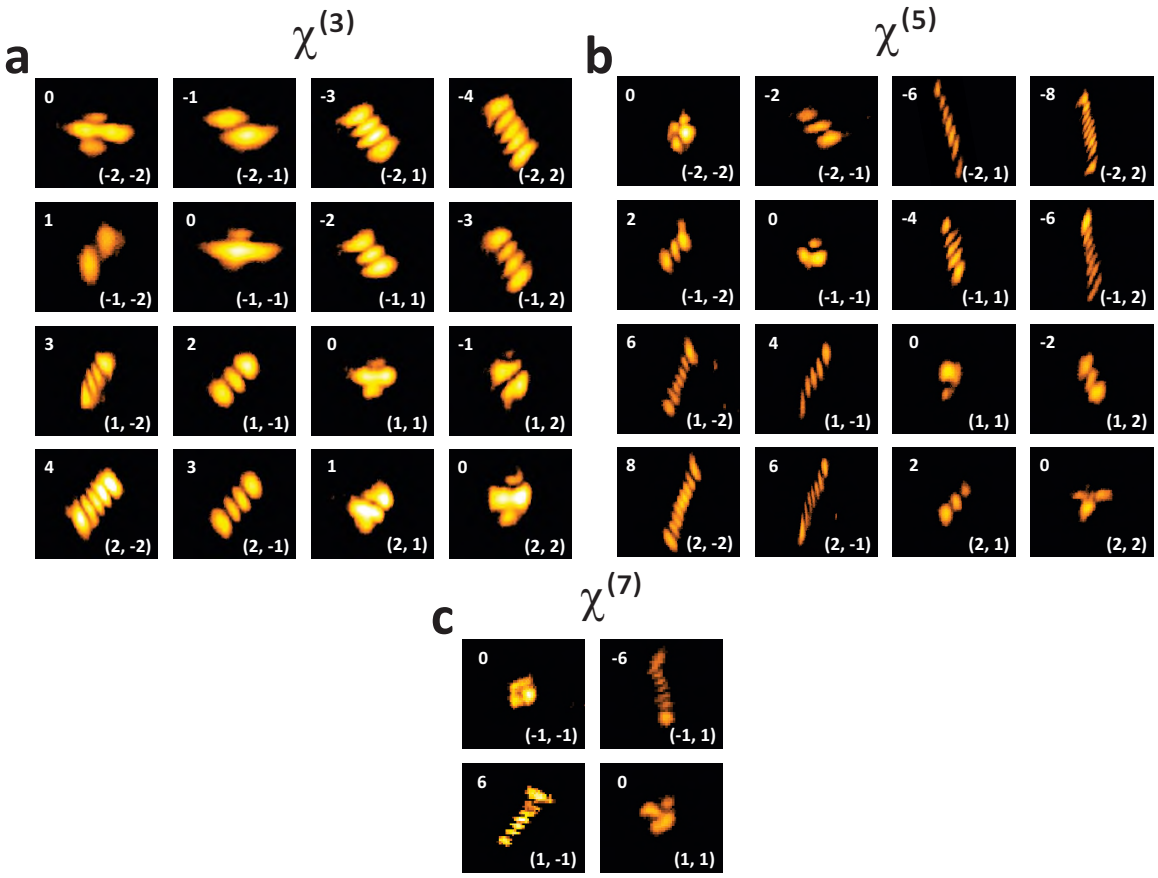

Figure 5.22 Memory output for input states with OAM in both writing beams. Retrieved topological charges for $\chi^{(3)}$ (a), $\chi^{(5)}$ (b), and $\chi^{(7)}$ (c) memories, in the case of different combinations of input topological charges of W' and W. The values of the pair $(\ell_{W'}, \ell_W)$ and the values of the retrieved topological charges are indicated, respectively, in the bottom-right and top-left corners of each frame.

the nonlinearity of the medium. Clearly the pulse durations used in a typical communication system are far shorter than the pulse durations required for imprinting the information in our atomic memory. Nevertheless, these results would be the first implementation of our initial proposal of integrating storage and manipulation of states of light inside the same quantum memory.

5.15 Manipulation of superpositions

In the last section we presented the manipulation for simple modes, i.e., beams with a well-defined charge $\ell = 0, 1, 2, ...$ However, we can use as an input more complex states of light such as superpositions of OAM modes. For instance, suppose that the W mode is a coherent superposition of OAM modes with charges ℓ_W and ℓ'_W. The field can be written as

$$u(r,\phi,z) = \mathscr{E}_W(\vec{r},t)e^{i(k_W z-\omega_W t)}\left(e^{i\phi\ell_W} + e^{i\phi\ell'_W}\right) . \tag{5.28}$$

Therefore, if W' is a Gaussian beam with charge $\ell_{W'} = 0$, we would have for the $\chi^{(3)}$, for the $\chi^{(5)}$, and for the $\chi^{(7)}$

$$(\Omega_W\Omega^*_{W'}) \propto \left(e^{i\phi\ell_W} + e^{i\phi\ell'_W}\right) , \tag{5.29a}$$

$$(\Omega_W\Omega^*_{W'})^2 \propto \left(e^{i\phi\ell_W} + e^{i\phi\ell'_W}\right)^2 = \left(e^{2i\phi\ell_W} + e^{2i\phi\ell'_W} + 2e^{i\phi(\ell_W+\ell'_W)}\right) , \tag{5.29b}$$

$$(\Omega_W\Omega^*_{W'})^3 \propto \left(e^{i\phi\ell_W} + e^{i\phi\ell'_W}\right)^3 = \left(e^{3i\phi\ell_W} + e^{3i\phi\ell'_W} + 3e^{i\phi(2\ell_W+\ell'_W)} + 3e^{i\phi(\ell_W+2\ell'_W)}\right) , \tag{5.29c}$$

respectively. Therefore, the output of the memory would be a different superposition for the higher orders.

In order to enlighten the usefulness of this, let's consider how OAM is used in quantum information. Usually in this context the topological charge is a good quantum number so that we may build a base defined by (..., $|\ell=-2\rangle$, $|\ell=-1\rangle$, $|\ell=0\rangle$, $|\ell=1\rangle$, $|\ell=2\rangle$, ...). Thus, states can be written, for instance, as

$$|\Psi\rangle = \alpha\,|\ell\rangle + \beta\,|\ell'\rangle , \tag{5.30}$$

where $\alpha^2+\beta^2 = 1$. In reference [63] there are a few experimental examples of such states. The authors show single-photon images of OAM simple states such as $|-1\hbar\rangle$, $|0\hbar\rangle$, $|+1\hbar\rangle$, $|+2\hbar\rangle$, and also superposition states such as $|+2\hbar\rangle + |-2\hbar\rangle$, $|+3\hbar\rangle + |-3\hbar\rangle$, and $|+20\hbar\rangle + |-20\hbar\rangle$.

Now, consider that our initial state is $|\ell=1\rangle$, our $\chi^{(5)}$ memory would transform it into $|\ell=2\rangle$. This shows that the transformation presented in the previous sections is nontrivial. Depending of the context, it can be more than an algebraic operation. In the last example it is a state transformation similar to a quantum gate.

As another example, we consider the possibility of transforming a superposition state. Let us suppose the initial photon state is

$$|\Psi\rangle = \frac{1}{\sqrt{2}}\left(|\ell\rangle + |-\ell\rangle\right) . \tag{5.31}$$

According to the Eq. (5.29b) for the special case with $\ell_W = -\ell'_W$ the $\chi^{(5)}$ process gives

$$(\Omega_W \Omega^*_{W'})^2 \propto \left(e^{2i\phi\ell_W} + e^{2i\phi\ell'_W} \right) . \tag{5.32}$$

Therefore, the output would be

$$|\Psi\rangle = \sqrt{1/2}\,(|2\ell\rangle + |-2\ell\rangle) . \tag{5.33}$$

We want to stress that even though the experimental results with OAM presented here involves bright beams, the orbital angular momentum is present due to the spatial structure of the beam. In principle, one should therefore be able to observe the same kind of transformation even at the single photon level.

Chapter 6

Raman Gain

6.1 Introduction

Since its first observation [88] many applications have been proposed for light carrying orbital angular momentum. To name a few, one can cite micromanipulation [89], imaging [90], and communication systems [91]. The motivation to use OAM states for applications in quantum information is related to the possibility of enhancing the efficiency of protocols using the multidimensional state space provided by OAM modes [91]. This is true not only for quantum communication but also for classical communication. For instance, it was recently demonstrated experimentally that OAM can be used to increase the channel capacity and spectral efficiency of millimetre-wave wireless communication links [92] and to implement high rate data encoding [93].

In this context of classical communication, an important issue is the ability to reverse the propagation losses, especially for long distances. The common method is to introduce amplifiers along the path to recover the damped signal. Here we demonstrate that a LG mode can be amplified through a nonlinear stimulated Raman process. The amplification of a mode can be also done through parametric gain via four-wave mixing, as has been studied exhaustively in the literature. However, the parametric gain produced by this kind of process can only be acheived under stringent experimental conditions, such as phase matching, high intensity and far from resonant detuning. Here it is shown that it is possible to observe gain in a much simpler configuration. The results discussed here were published in [35].

6.2 Experimental set up

The experimental apparatus used here is very similar to the one presented in the previous chapters. Therefore, we will not give all the details to avoid repetition. The experiment is performed in a cloud of cold cesium atoms obtained from the magneto-optical trap (MOT) using the Zeeman structure of the hyperfine levels $6S_{1/2}(F=3)$ and $6P_{3/2}(F'=2)$. The atoms are initially pumped into the $6S_{1/2}(F=3)$ ground-state via a non resonant excitation induced by the trapping beams. The writing and reading beams are switched on inside the period of 1 ms in which all MOT beams and magnetic field are off. Three pairs of Helmholtz coils are employed to compensate for residual magnetic fields.

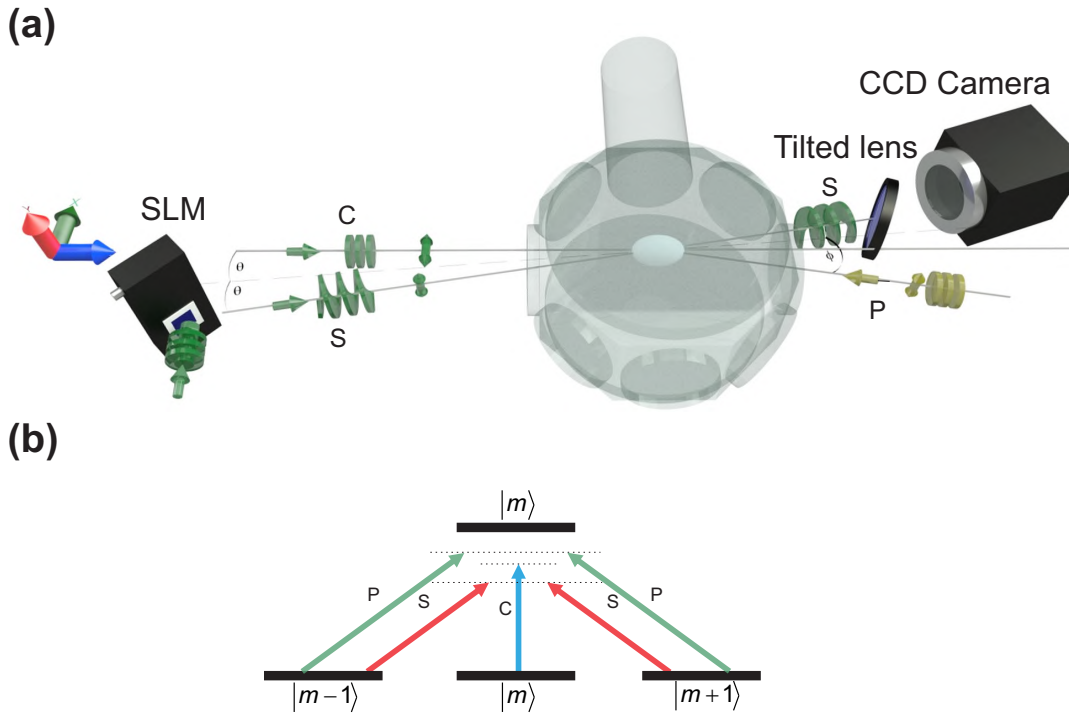

Figure 6.1 (a) Simplified spatial configuration of the optical fields. (b) Double-Λ system corresponding to Zeeman sublevels of the hyperfine transition $(F = 3) \rightarrow (F' = 2)$. It is also indicated the coupling of the sublevels with the respective optical fields.

A coupling beam C and a signal beam S, with orthogonal linear polarizations, are shined on the cold atomic ensemble forming a small angle $2\theta \approx 2^\circ$ as indicated in Fig. (6.1a). The sample also interacts with a couterpropagating pumping beam P, with the same linear polarization as the signal beam S. The three beams interact simultaneously for $30\mu s$ until the system reaches the steady state. The fields are temporally modulated by three independent acousto-optic modulators (AOM), that also enable us to control their frequencies individually. Since no external magnetic field is applied, we consider the C beam polarization direction as the quantization axis. Therefore, for the particular polarization composition of this set of beams, one can approximate the light-matter interaction in the whole Zeeman structure as the interaction in sets of Λ three-level systems as shown in Fig. (6.1b).

As in the memory case, we use a SLM to shape the signal S beam as a Laguerre–Gauss (LG) mode. The coupling and the pump beams are Gaussian beams with no topological charge.

6.3 Theoretical model

We model our atom as an homogeneously broadened three-level Λ system, as shown in Fig.6.2, where the states $|a\rangle$ and $|c\rangle$ are non-relaxing ground states with zero energy and the state $|b\rangle$ is the excited level with energy $\hbar\omega_0$ and decay rates to the two ground states equal to Γ_{ba} and Γ_{bc}, respectively, with $\Gamma = \Gamma_{ba} + \Gamma_{bc}$ being the total spontaneous decay rate, $\Gamma/2\pi =$

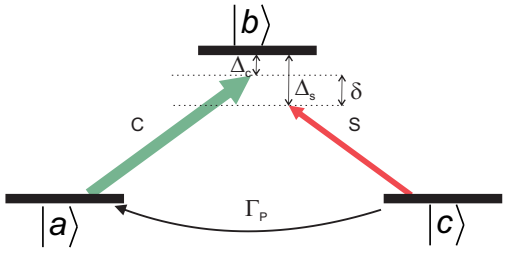

Figure 6.2 Simplified Λ system considered in the theoretical model.

$5.2MHz$.

The role of the P field is only to pump atoms from $|c\rangle$ to $|a\rangle$ to create a population inversion. Therefore, instead of considering the coherent coupling between the pump field and the excited states we treat it as an incoherent pump with an effective rate, that essentially transfers population from other Zeeman sublevels to the one interacting with the coupling beam C. In other words, the strong P field transfers population incoherently at rate Γ_P from $|c\rangle$ to $|a\rangle$, creating a population inversion between these levels. The C field excites the atom and the S field induces the stimulated decay, producing a gain. This simplification is sufficient to capture the essential physical characteristics of the system as we will see in the comparison with the experimental results.

In the rotating wave approximation, the time evolution of the slowly varying populations and coherences is given then by the equations:

$$\frac{d\sigma_{aa}}{dt} = i\left[\Omega_C\sigma_{ba} - \Omega_C^*\sigma_{ab}\right] + \Gamma_{ba}\sigma_{bb} + \Gamma_P\sigma_{cc}\ , \tag{6.1a}$$

$$\frac{d\sigma_{cc}}{dt} = i\left[\Omega_S\sigma_{bc} - \Omega_S^*\sigma_{cb}\right] + \Gamma_{bc}\sigma_{bb} - \Gamma_P\sigma_{cc}\ , \tag{6.1b}$$

$$\frac{d\sigma_{bb}}{dt} = -i\left[\Omega_C\sigma_{ba} - \Omega_C^*\sigma_{ab} + \Omega_S\sigma_{bc} - \Omega_S^*\sigma_{cb}\right] - \Gamma\sigma_{bb}\ , \tag{6.1c}$$

$$\frac{d\sigma_{ab}}{dt} = i\Delta_C\sigma_{ab} + i\Omega_C\left(\sigma_{bb} - \sigma_{aa}\right) - i\Omega_S\sigma_{ac} - \frac{\Gamma}{2}\sigma_{ab}\ , \tag{6.1d}$$

$$\frac{d\sigma_{cb}}{dt} = i\Delta_C\sigma_{cb} + i\Omega_S\left(\sigma_{bb} - \sigma_{cc}\right) - i\Omega_C\sigma_{ca} - \frac{\Gamma}{2}\sigma_{cb}\ , \tag{6.1e}$$

$$\frac{d\sigma_{ac}}{dt} = i\delta\sigma_{ac} + i\left[\Omega_C\sigma_{bc} - \Omega_S^*\sigma_{ab}\right] - i\Omega_C\sigma_{ca} - \frac{\Gamma}{2}\sigma_{cb}\ . \tag{6.1f}$$

where $\delta = \Delta_C - \Delta_S$ is the two-photon detuning,

$$\Omega_j(\vec{r},t) = \frac{id_j\mathscr{E}_j(\vec{r},t)e^{i\vec{k}_j\cdot\vec{r}}}{4\hbar} \tag{6.2}$$

is the Rabi frequency associated with beam j. We consider $\Gamma_{ba} = \Gamma_{bc} = \frac{\Gamma}{2}$. The system is considered closed, so $\rho_{aa} + \rho_{bb} + \rho_{cc} = 1$.

The response of the system is found, in the steady state regime, in all orders in the C field

and in first order in the S field. The solutions for the coherence and populations are

$$\sigma_{aa}^{(0)} = \frac{\left(\frac{\Gamma}{2}\right)^2 + |\Omega_C|^2 + \Delta_C^2}{\left(\frac{\Gamma}{2}\right)^2 + |\Omega_C|^2 \left(2 + \frac{\Gamma}{2\Gamma_P}\right) + \Delta_C^2}\,, \tag{6.3a}$$

$$\sigma_{bb}^{(0)} = \frac{1 - \sigma_{aa}^{(0)}}{1 + \frac{\Gamma}{2\Gamma_P}}\,, \tag{6.3b}$$

$$\sigma_{cc}^{(0)} = \frac{\Gamma}{2\Gamma_P} \frac{1 - \sigma_{aa}^{(0)}}{1 + \frac{\Gamma}{2\Gamma_P}}\,, \tag{6.3c}$$

$$\sigma_{ab}^{(0)} = \frac{\Gamma}{2\Gamma_P} \frac{1 - \left(2 + \frac{\Gamma}{2\Gamma_P}\right) \sigma_{aa}^{(0)}}{\left(2 + \frac{\Gamma}{2\Gamma_P}\right) \left(i\Delta_C - \frac{\Gamma}{2}\right)}\,, \tag{6.3d}$$

$$\sigma_{cb}^{(1)} = \frac{\Omega_S \left(i\frac{\Gamma_P}{2} - \delta\right) \left(\sigma_{cc}^{(0)} - \sigma_{bb}^{(0)}\right) - \Omega_C \Omega_S \sigma_{ba}^{(0)}}{\left(\frac{\Gamma_P}{2} + i\delta\right) \left(i\Delta_2 - \frac{\Gamma}{2}\right) - \Omega_C^2}\,. \tag{6.3e}$$

The dispersion and the absorption of the S field are related to the real and imaginary parts, respectively, of σ_{cb}. Therefore, we can use expression (6.3e) to plot the theoretical signal-beam transmission spectrum as depicted in Fig. 6.3. In the curves we used $\Omega_C/\Gamma = 0.1$, $\Gamma_P/\Gamma = 0.05$ and an optical depth of 3. The one order of magnitude discrepancy in the Rabi frequency for the coupling beam is probably due to the simplification of the model that ignores the multiplicity of the Zeeman structure, which results in a smaller effective intensity.

If the P beam is removed, we would be left with a strong and a weak field in a Λ three level system, which is the exact configuration for EIT. Therefore, it is expected that for $\Gamma_P = 0$, we obtain the usual EIT spectrum. This seems to be the case as one can see in Fig. 6.3, where at $\delta = 0$ we have a transmission maxima.

Equally important is the fact that σ_{cb} is proportional to Ω_S, which is by its turn proportional to the phase of the incoming S beam. This means that if we have a Laguerre-Gauss beam carrying a topological charge instead of a fundamental Gaussian beam, we would end having an amplified field with the same topological charge after the sample.

6.4 Experimental Results

We present in this section two sets of measurements. In the first, we set the SLM in the S beam to generate fundamental Gaussian modes ($\ell = 0$) to investigate the mechanics of the gain itself. In the second we set the SLM in the S beam to generate arbitrary values of OAM, to investigate the amplification of the LG mode.

6.4.1 Spectral analysis of the gain

As stated in the previous section, in this first set of measurements all the beams are gaussian modes and we investigate the gain itself through its spectral analysis. All fields have their

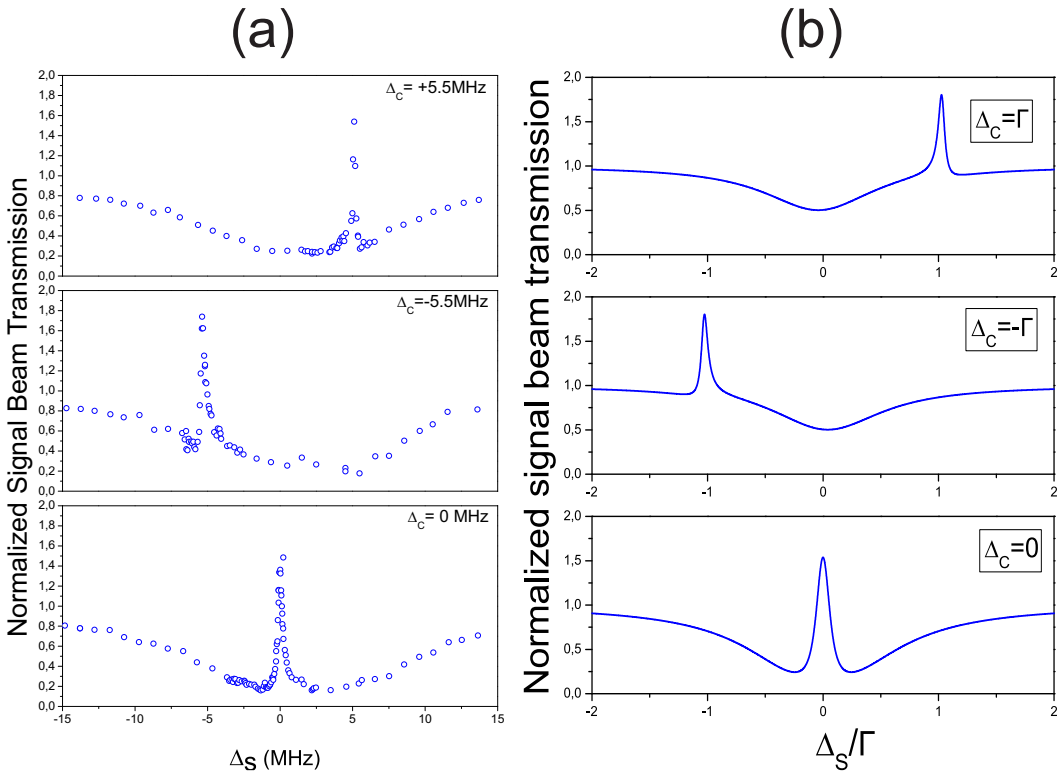

Figure 6.3 (a) Experimental spectrum of the transmission of the field S as a function of the frequency detuning Δ_S for different values of the detuning Δ_C. (b) Theoretical spectrum of the transmission of field S as a function of the frequency detuning Δ_S for different values of the detuning Δ_C.

frequencies tuned around the $6S_{1/2}(F=3) \rightarrow 6P_{3/2}(F'=2)$ transition. Each field has it own detuning, namely, Δ_S, Δ_C, and Δ_P.

For the pump beam P blue-detuned by $\Delta = 1MHz$, we examine the signal transmission while we scan the two-photon detuning $\delta = \Delta_C - \Delta_S$ for three different detunings of the coupling beam C, namely, $\Delta_C = 0, \pm 5.5$ MHz. In Fig. (6.3a) we show curves for 100 kHz steps. The spectra exhibit gains up to 70% for $\Delta_C = -5.5MHz$ around $\delta = 0$. This gain also depends on the intensity and detuning of the pump beam P and cannot be observed in its absence. Since the fields are in the four wave mixing (FWM) configuration, as one can see from the spatial arrangement in Fig.(6.1a), one might be induced to assume this is a gain generated by the nonlinear process. We have also tested orienting the pump beam in a direction which is non-phase-matched in order to assure that it does not contribute to any parametric gain via FWM. The gain was resilient to these changes, demonstrating that the P field acts only as an incoherent pump that generates a population inversion between two Zeeman ground states. We understand this gain as originating from Raman amplification of the signal beam S due to a population inversion between the two Zeeman ground states, induced by the pumping beam P.

6.4.2 Amplification of the LG mode

In the second set of measurements, we use the SLM to generate LG modes with topological charges $\ell = 1, 2, 3, 4$.

We have adjusted the waist of the signal beam to fit inside the intersection of the pump and coupling fields in order to obtain a homogeneous amplification in the spatial structure of the field. This is the reason behind the reduction of the gain in the OAM amplification (up to 20%) showed in Fig. 6.4 compared to the gain without OAM showed (up to 70%) in Fig.(6.1a).

The beam waist increases with the topological charge and its values at the atomic cloud are 0.3 mm, 0.5 mm, 0.7 mm 1.0 mm and 1.1 mm, respectively for the modes with $\ell = 0, 1, 2, 3, 4$, which are all smaller than the 1.5 mm of the *C* and *P* beams. As a consequence, the beams with higher topological charge interact with more atoms. This explains why the gain increases with the topological charge, as may be observed in Fig. 6.4.

6.5 Conclusion

We have experimentally observed the amplification of a weak signal beam in an ensemble of cold cesium atoms through a stimulated narrow-band Raman gain mechanism. This was used to demonstrate the amplification of a LG mode carrying OAM. These results might be useful in classical communication using light modes with OAM-encoded information, particularly for long-distance communication, which requires amplification nodes that preserves the phase structure of the mode, to compensate for inevitable losses.

A simple theoretical model using density matrix approximates the whole Zeeman structure interacting with three fields as sets of Λ three-level systems interacting with two coherent fields in the presence of an incoherent pumping. The model reproduces qualitatively well the experimental results, in particular the amplitude and subnatural spectral width of the gain's spectrum.

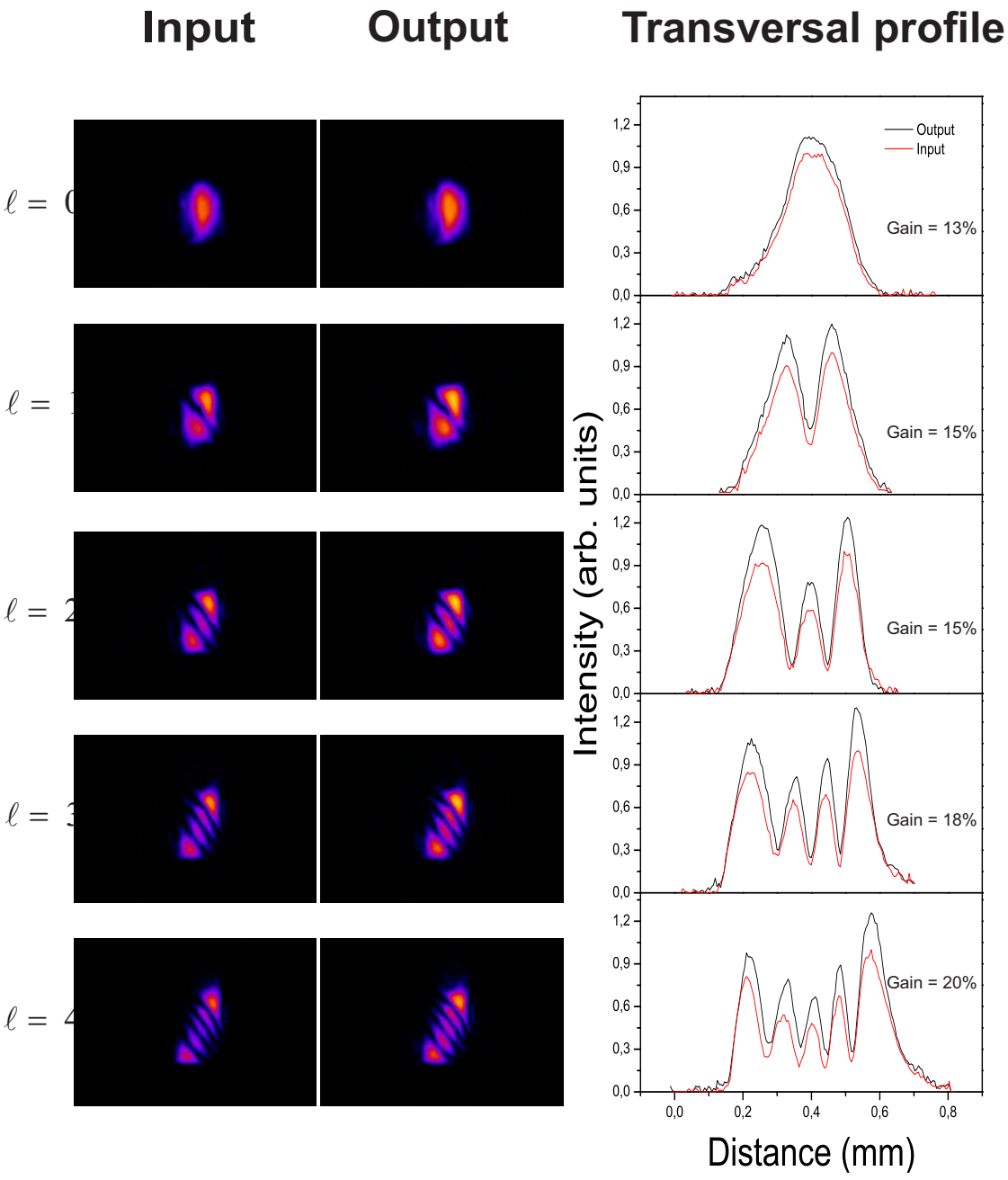

Figure 6.4 Measurement of the topological charge of the signal beam *S*. The first column displays the topological charge of the incident beam, measured without the atoms. The second column displays the topological charge after the amplification in the atomic system. The third column shows the transversal profile of the images of the first (red) and second (black) columns.

PART III

Single photon regime

Chapter 7

Atomic memory in the single-photon regime

7.1 Introduction

Nonlinear optics is behind the generation and manipulation of many quantum states of light such as squeezed states [94] and Fock states [95]. Therefore, we expect that, by moving to higher orders, one would observe new quantum states of light. Moreover, nonlinear optical phenomena allows the creation of entangled states. Twin photon generation became one of the most popular procedures to generate entanglement between pairs of photons. However, to go beyond two dimensional spaces can be quite challenging using the common methods.

Multipartite entanglement provides considerable advantages when compared with bipartite entanglement in several applications in quantum technologies and fundamental tests of quantum mechanics. For instance, it can be used to create a network with multiple senders and receivers [96], increase the sensitivity in metrology [97], observe extreme spin squeezing [98], and so forth. Therefore, generation of photonic multipartite entanglement became an important goal in quantum optics.

The first step to generate multiphoton entangled states would be the production of photon triplets. Several theoretical proposals have been suggested for the generation of photon triplets. A few examples are cascaded spontaneous parametric down-conversion [99], tri-excitons in quantum dots [100], and combinations of $\chi^{(2)}$ processes [101]. However, due to the low efficiency of these processes only a few experimental implementations can be found in the literature. We highlight the efforts using cascaded spontaneous parametric down-conversion [102] and a third-order nonlinear process [103].

In cascaded spontaneous parametric down-conversion, the idea is to use one of the photons from the pair generated by a first down-conversion source pumped by a laser as the pump for a second down-conversion crystal. However, since conversion efficiency in these crystals are very low, using a single-photon as a pump field can lead to a low rate of triplet generation. In reference [102] this rate was approximately 4.7 ± 0.6 counts per hour.

Here we propose a concrete method to generate triplets of correlated photons based on the configuration presented in the previous chapters. The experiment is not yet finished, therefore only the concept will be discussed. We believe that the final version of the system will provide the observation of new quantum states of light. We also expect to have a higher efficiency

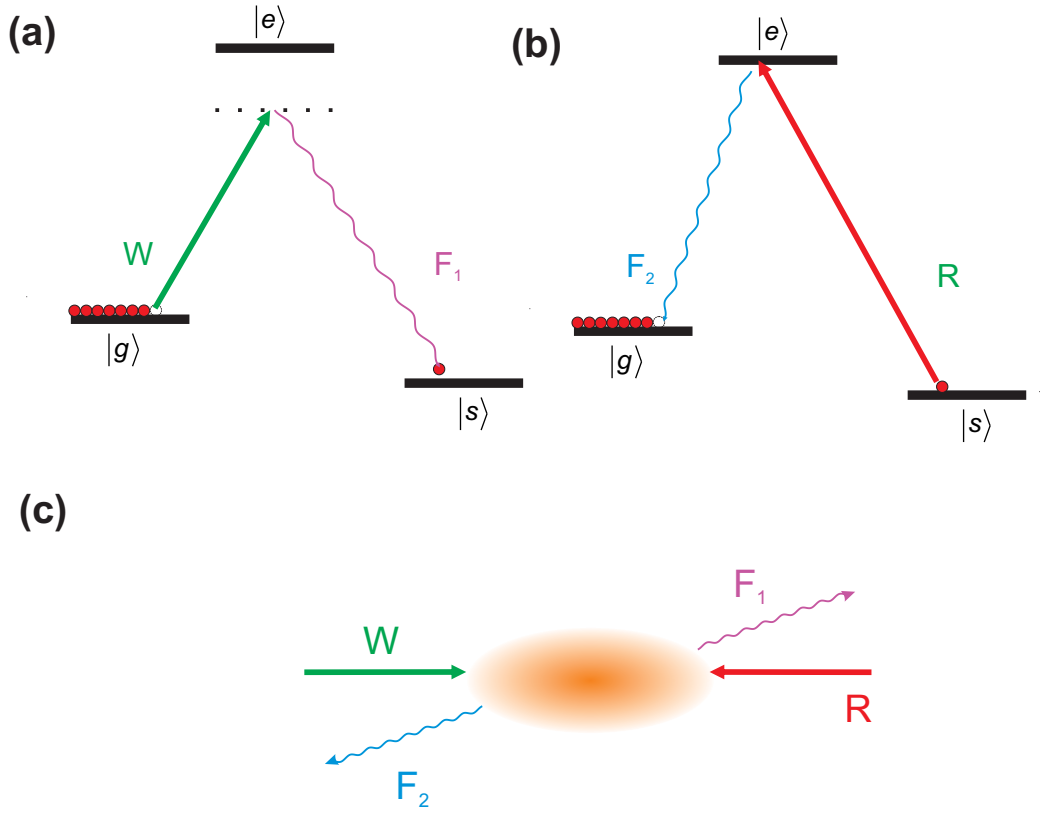

Figure 7.1 Schematic description for photon-pair generation in the DLCZ-protocol scheme. (a) Firstly, one shines a write beam transferring an atom from $|g\rangle$ to the other ground state $|s\rangle$ and generating the Field 1. (b) After a chosen delay, the read field is switched on, transferring the atom back from $|s\rangle$ to $|g\rangle$ with the emission of the Field 2. (c) The spatial configuration of the fields involved is the same of the four-wave mixing. The pairs write and read, Field 1 and Field 2 are counter-propagating.

compared to the popular method of spontaneous parametric down-conversion. Our scheme offers another advantage compared to parametric down-conversion: it has memory.

7.2 Generation of photon-pairs in the DLCZ-protocol scheme

Before explaining our proposal for generation of multiple quantum-correlated photons, it is necessary to explain the inspiration for our method, i.e., the generation of photon-pairs in the DLCZ-protocol scheme [5].

The building block of the protocol is an ensemble with N identical atoms in a Λ configuration, interacting with two fields, a writing field W and a reading field R, that induces the spontaneous generation of two other fields (see Fig. 7.1).

Initially, all the atoms are prepared in the same ground state $|g\rangle$, in such a way that the state

of the system can be written as

$$|\Psi\rangle = \prod_{i=1}^{N} |g_i\rangle \tag{7.1}$$

A first light field W interacts with the sample, having a small probability of transferring one atom from $|g\rangle$ to the other ground state $|s\rangle$, simultaneously with the emission of the field 1 [see Fig. (7.1a)]. However, since all the atoms illuminated by the writing field have the same probability of being transferred, we cannot know which one made the transition. This indeterminacy forces one to write the new state of the system as a superposition of all possibilities, namely

$$|1_a\rangle = \frac{1}{N} \sum_i |g_1\rangle \cdots |s_i\rangle \cdots |g_N\rangle \ , \tag{7.2}$$

which is a symmetric collective state. Naturally, during the excitation of the writing field, more than one atom can be transferred from $|g\rangle$ to $|s\rangle$. In this case, other states like $|2_a\rangle$, $|3_a\rangle$, etc. would be generated.

In the situation where one has a writing field power low enough to make the higher-order excitation components negligible, the total state, field 1 and atomic parts, can be written as

$$\left|\Psi_{a,1}\right\rangle = |0_1\rangle\,|0_a\rangle + e^{i\beta}\sqrt{p}\,|1_1\rangle\,|1_a\rangle + O(p) \ , \tag{7.3}$$

where $|n_1\rangle$ corresponds to the state of the field 1 with n photons, p is the probability of a single atomic excitation, $O(p)$ represents the terms with excitation probabilities equal or higher than p^2, and β is the phase determined by the propagation of the writing field. Note that Eq. 7.3 tells that the detection of a photon in the mode of field 1 heralds a single excitation in the ensemble. That is if field state is $|1_1\rangle$, then the atomic state must be $|1_a\rangle$. This excitation (and the superposition that exists in it) remains stored in the ensemble as long as the decoherence processes do not erase it.

One can access this excitation to generate a second photon. If one switches on a reading field resonant with the transition $|s\rangle \rightarrow |e\rangle$, the atom is transferred back to the state $|g\rangle$, and the collective excitation is mapped back to the photonic state called field 2 [see Fig. (7.1b)]. In this case the superposition among the atoms is destroyed, erasing completely the information from the ensemble. The total state of field 1 and 2 is

$$\left|\Psi_{1,2}\right\rangle = |0_1\rangle\,|0_2\rangle + e^{i\beta'}\sqrt{p}\,|1_1\rangle\,|1_2\rangle + O(p) \ . \tag{7.4}$$

Note that the state in Eq. 7.4 is an entangled state in the number of photon basis, similar to the one in parametric down-conversion [5]. Therefore, the two photons exhibit strong correlations between them.

7.3 General idea of the experiment

In this chapter we aim to introduce a full quantum version of the experiment presented in chapter 5. The basic spatial configuration employed is the same as the one presented in chapter

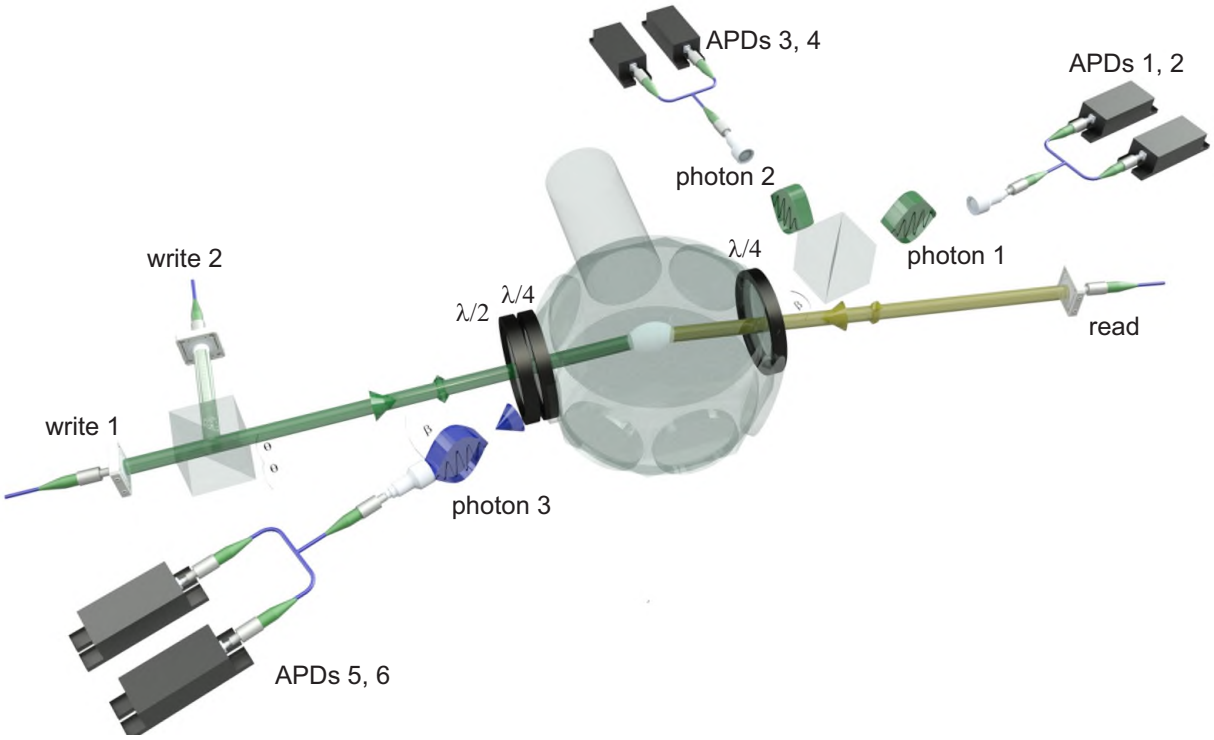

Figure 7.2 Simplified experimental set up for generation of triplets. The process consists in one absorption in the mode W_1 and one emission in the mode of *photon 1*, followed by a second absorption in the mode W_2 and one emission in the mode of the *photon 2*, followed by a one-photon absorption of R and one-photon emission of *photon 3* in the phased-matched direction.

5 that allows an angular selection of a specific order of nonlinearity. However, instead of using two write fields W and W' (writing beams) with an angle $2\theta \approx 2^\circ$ between them as in chapter 5, where the first excites the atom and the second induces stimulated emission, we remove W' to observe spontaneous emission in this mode. We consider only the $\chi^{(3)}$ and $\chi^{(5)}$ signals, leaving the $\chi^{(7)}$ for future efforts.

Another difference is that, unlike the semi-classical case, where the write process reaches a steady-state with two strong fields, here we are interested in the pulsed excitations. Only one atom is excited from the whole ensemble into the target collective mode and, as a consequence, only one photon is emitted per transition. Therefore, for the $\chi^{(5)}$ process one has one absorption in mode W_1 and one emission in the mode of *photon 1*, followed by a second absorption in mode W_2 and one emission in the mode of the *photon 2*, followed by a one-photon absorption of R and one-photon emission of *photon 3* in the phased-matched direction. Figure 7.2 depicts schematically the idea for the $\chi^{(5)}$ experiment.

The details of the cloud formation, write and read processes are presented in the following sections.

7.4 Magneto-optical trap (MOT)

The basic idea for obtaining a cold sample is the same as explained in the chapter 5. There are only a few differences between the MOT used in the single-photon experiment and the one used in the semi-classical experiment. The first difference is the atom. This experiment is performed in another laboratory that uses Rubidium 87 instead of Cesium.

The cooling laser is locked at the cross-over $F = 1-3$, which is exactly midway the transitions $5S_{1/2}(F=2) \rightarrow 5P_{3/2}(F'=1)$ and $5S_{1/2}(F=2) \rightarrow 5P_{3/2}(F'=3)$, while the repumper laser is at the $F = 1-2$ cross-over, which is exactly midway the transitions $5S_{1/2}(F=1) \rightarrow 5P_{3/2}(F'=1)$ and $5S_{1/2}(F=1) \rightarrow 5P_{3/2}(F'=2)$ (Fig.7.3). A pair of independent AOMs are used to tune the cooling and repumping laser frequencies to 17 MHz below resonance from the $5S_{1/2}(F=2) \rightarrow 5P_{3/2}(F'=3)$ transition and exactly on resonance with $5S_{1/2}(F=1) \rightarrow 5P_{3/2}(F'=2)$ transition, respectively. The first is kept on for 20 ms together with the MOT quadrupolar magnetic field, whereas the second for 21 ms, providing a cold sample with 2 mm diameter and an optical density of approximately 30. During the additional 1 ms the repumping beam is on, it pumps the atoms into the $5S_{1/2}(F=2)$ ground-state.

The beams are conducted by three independent polarization maintaining (PM) optical fibers to the glass chamber. At the exit of each fiber, there is a collimator with a lens $f = 100mm$, that leaves the beam with 1cm. Here we have another difference with respect to the MOT presented in chapter 5. We do not retroreflect the three beams that leave the fibers, instead we split into two x axis beams in a PBS. The transmitted beam goes to one window of the science chamber, while the reflected part goes to the opposite window (see Fig.7.4). The same occurs for the y axis. The z axis remains retroreflected. Before the cell we use quarter-wave plates to change the linearly polarized light that leaves the fiber into circularly polarized light.

We use one homemade laser head (diode model Thorlabs DL7140-201S), with an output power of approximately $70mW$, for generating all six cooling fields, write, and read beams and a second diode laser identical to the first, for the repumper. The cooling laser is amplified by a tampered amplifier (Sacher Lasertechnik – Tapered Littrow Laser 1.5W).

7.5 Experimental set up

We prepare our state by shining the medium with a circularly polarized σ^- beam, pumping all the atoms to the extreme of the Zeeman structure. In other words we prepare the system with all atoms in the same level through optical pumping to the state $|g\rangle = |F=2, m_F=-2\rangle$ of the $5S_{1/2}$ manifold (see Fig. 7.5). Therefore, we are left with an ensemble of atoms in a double Λ configuration. The other relevant ground state $|s\rangle$ corresponds then to the Zeeman sublevel $|F=2, m_F=0\rangle$ from the same manifold (Fig.7.5). There are two excited states $|e\rangle$ and $|e'\rangle$ that correspond to the Zeeman sublevels $|F'=3, m_{F'}=-1\rangle$ and $|F'=2, m_{F'}=-1\rangle$, respectively, from the hyperfine level $5P_{3/2}(F'=2)$ of the D_2 line of Rubidium 87 (Fig.7.5). The reason we use $(F'=2)$ transition for the second writing beam and not $(F'=3)$ is due to the fact that the $(F'=3)$ beam would also interact with the other atoms in $|g\rangle$. With the beam tuned to the $5S_{1/2}(F=2) \rightarrow 5P_{3/2}(F'=2)$ transition, we can use a strong and resonant beam

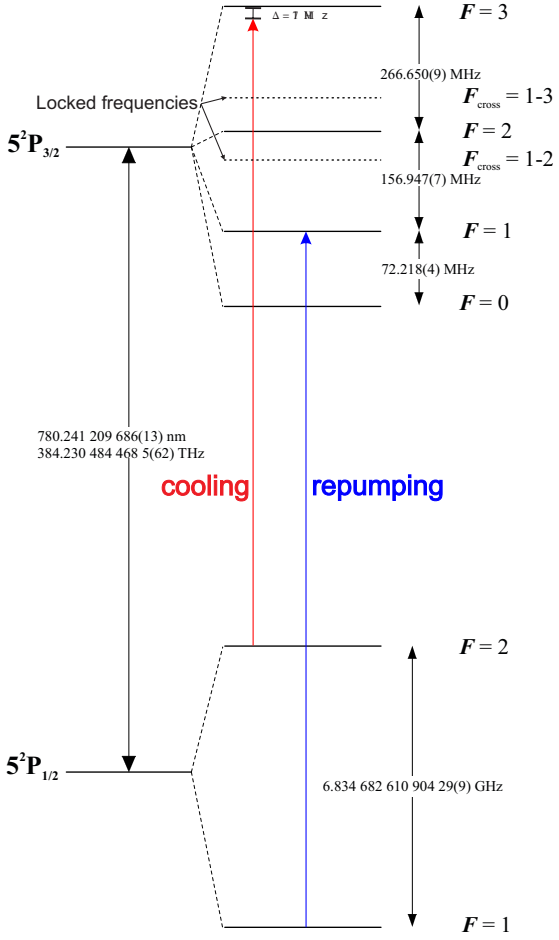

Figure 7.3 Rubidium MOT transitions. The numbers were taken from [104]

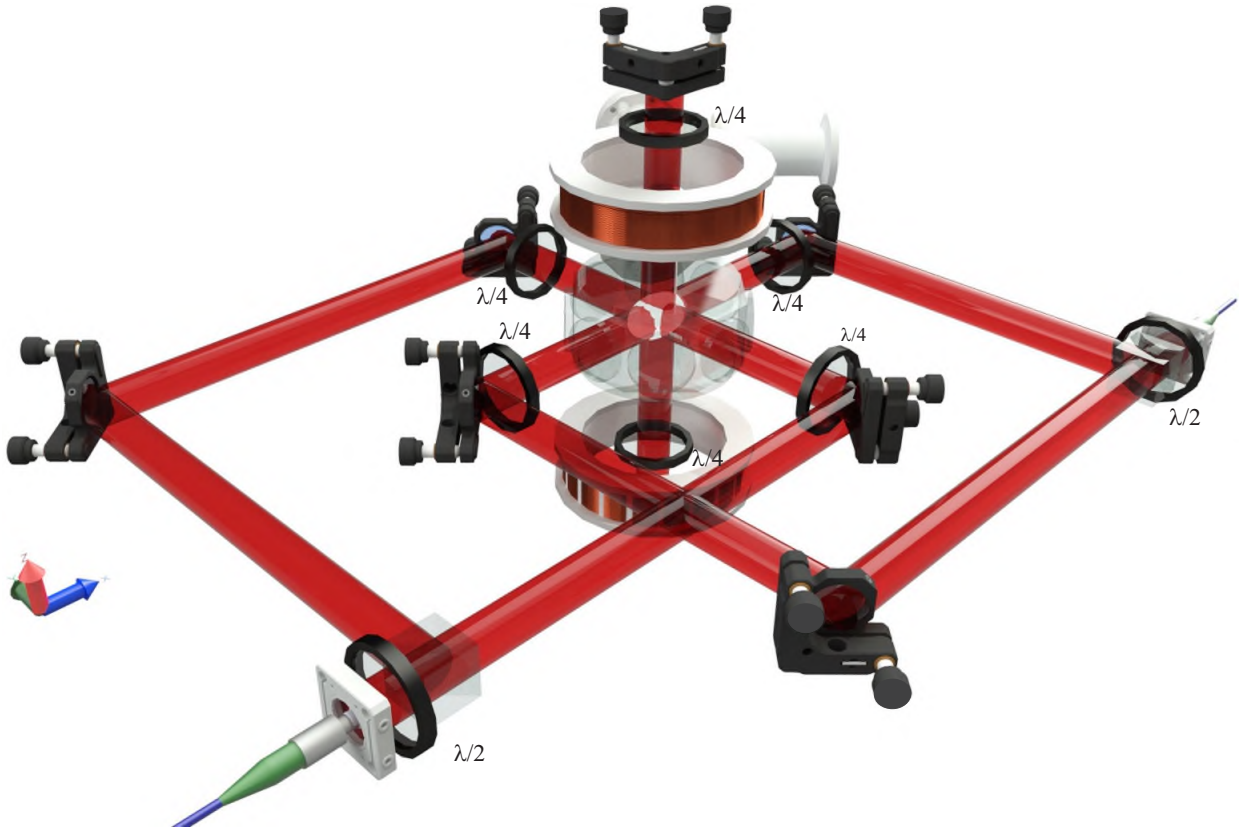

Figure 7.4 Basic implementation of the MOT for the ^{87}Rb optical table. Three independent polarization maintaining (PM) optical fibers conduct the beams to the glass chamber. A PBS splits into two the x axis beams and a half-wave plate controls the relative power allowing to optimize the optical depth by fine tuning the splitting ratio between the two counter-propagating beams on the x direction. The same goes for the y axis. Two coils with currents running in opposite directions generate the magnetic field in anti-Helmholtz configuration.

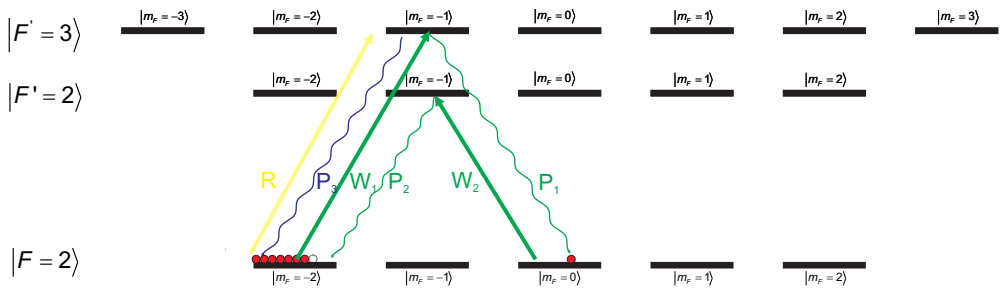

Figure 7.5 Transition sequence in a double-Λ system.

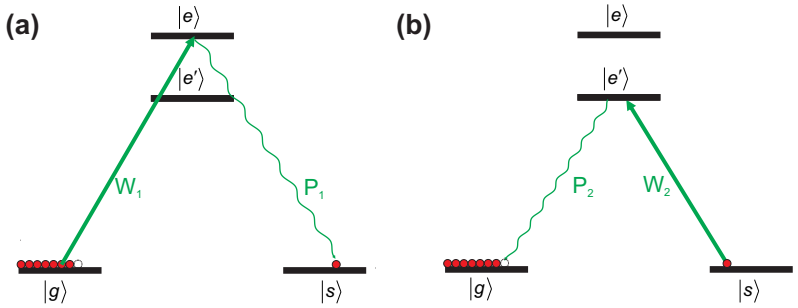

Figure 7.6 Write process.

with a smaller risk of disturbing the rest of the system, since it only interacts strongly with one atom. The cold ensemble is obtained from a magneto-optical trap (MOT), whose trapping and repumping lasers are turned off during the experiment period.

7.6 Writing

As in section 7.2, the system is initially prepared with all atoms in the same internal state. However, unlike in the most of DLCZ discussions, here it is included in the discussion also the external degrees of freedom, namely, the linear momentum **p**. The reasons will become clear in this section.

After preparation of the system in the state $|\Psi\rangle = |g,\mathbf{p}\rangle = |g_1\rangle|\mathbf{p}_1\rangle|g_2\rangle|\mathbf{p}_2\rangle\cdots|g_N\rangle|\mathbf{p}_N\rangle$ we can start the writing process. A write pulse most likely excites just one atom of the ensemble in the transition $|g\rangle \rightarrow |e\rangle$. To diminish the odds of more than a single excitation, a weak and $20MHz$ red-detuned write field is used during 50 ns. Therefore, there is a probability to transfer this atom spontaneously to the state $|s\rangle$ with the simultaneous emission of a single photon in the $|e\rangle \rightarrow |s\rangle$ transition, which we call *photon 1* [see Fig. (7.6a)]. The detection of *photon 1* heralds the transfer of one atom from $|g\rangle$ to $|s\rangle$. However, we do not know which atom made this transition. Therefore, we have to take into account all possibilities, leaving the ensemble

in the state

$$\begin{aligned}|\Psi\rangle =& A_1(0)e^{i(\boldsymbol{k}_W-\boldsymbol{k}_1)\cdot\hat{\boldsymbol{r}}_1}|s_1\rangle|g_2\rangle\cdots|g_N\rangle + A_2(0)e^{i(\boldsymbol{k}_W-\boldsymbol{k}_1)\cdot\hat{\boldsymbol{r}}_2}|g_1\rangle|s_2\rangle\cdots|g_N\rangle+\cdots \\ &+A_N(0)e^{i(\boldsymbol{k}_W-\boldsymbol{k}_1)\cdot\hat{\boldsymbol{r}}_N}|g_1\rangle|g_2\rangle\cdots|s_N\rangle \\ =&\sum_i A_i(0)|s_i\rangle|\boldsymbol{p}_i-\hbar(\boldsymbol{k}_W-\boldsymbol{k}_1)\rangle \end{aligned} \tag{7.5}$$

At this point we have two possibilities. One is to switch on the read field in the counter-propagating direction of the writing field, closing the $\chi^{(3)}$ process. The other is to use the second write field polarized orthogonally to the first one, accessing the $\chi^{(5)}$ process. This would be the quantum version of the selective memory presented in the chapter 5, where we create all different gratings choosing only one with the direction of the reading field.

In the second scenario, we use a field W_2 in the transition $|s\rangle$ to $|e'\rangle$. Since only one atom can interact with this field, unlike the first writing beam, we now use a stronger resonant field that increases the chances of success. Therefore, there is a probability to transfer this atom spontaneously back to the state $|g\rangle$ with the simultaneous emission of a single photon in the $|e'\rangle\rightarrow|g\rangle$ transition, which we call *photon 2* [see Fig. (7.6b)]. The detection of the photon 2 leaves the ensemble in the state

$$|\Psi\rangle = |g\rangle\sum_i A_i'(0)|\boldsymbol{p}_i-\hbar(\boldsymbol{k}_{W_1}-\boldsymbol{k}_1)-\hbar(\boldsymbol{k}_{W_2}-\boldsymbol{k}_2)\rangle \tag{7.6}$$

Note a striking difference between the $\chi^{(3)}$ and $\chi^{(5)}$ process. The first leaves the ensemble in a collective state that is entangled in the internal degrees of freedom (Eq. 7.5). The second does not have entanglement in the internal degrees of freedom because all atoms are back in the $|g\rangle$ state. However, even though the atom that performed the two writing transitions returned to the same internal state, it did not return to the same external state, since it gained momentum in the $(\mathbf{k}_{W_1}-\mathbf{k}_1)+(\mathbf{k}_{W_2}-\mathbf{k}_2)$ direction. In other words, in the $\chi^{(3)}$ we have entanglement in the internal degrees of freedom and in the $\chi^{(5)}$ we have entanglement in the external degrees of freedom (Eq. 7.6). The information is stored in different places, similar to the semi-classical case presented in chapter 5, where we have coherence and population gratings.

7.7 Reading

After the write process, the ensemble is left in the state described by Eq. 7.6, that will live as long as the written grating is present. The reading process can occur at any time between the collective state formation and the grating wash out. After a delay chosen by the experimentalist, a read pulse excites the atom in the transition $|g\rangle\rightarrow|e\rangle$ with a probability to transfer this atom spontaneously back to the state $|g\rangle$ with the simultaneous emission of a *photon 3* in the $|e\rangle\rightarrow|g\rangle$ transition (see Fig. 7.7). One can see that the reading process occurs basically in a two level system.

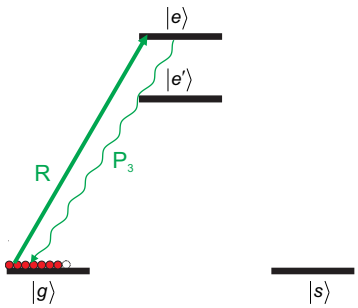

Figure 7.7 Read process.

7.8 Control system

All the pulses of the experiment, such as the magnetic field, cooling, repumper, writing, and reading fields are electronically controlled by an Arduino Due board, operated by an Arduino software. All the pulses are generated in 20ms cycles and they repeat themselves at the end of each cycle. First we generate a pulse to switch on the cooling and repumper beams for 17ms and 18ms, respectively. The MOT magnetic field remains on during the same 17ms of the cooling beams (see Fig.7.8). The coils that compensate for residual magnetic fields have no temporal control and stay on continuously. During the extra 1ms of the repumper beam pulse the atoms are optically pumped from $5S_{1/2}(F=1)$ to $5S_{1/2}(F=2)$, preparing the desired initial state. Here we have a few differences between the write and read pulses from the semi-classical memory present in chapter 5 and the ones used here. First of them is the number of pulses per cycle. In the semi-classical memory the write and read processes occurs once per cycle, i.e., we write the information, read it and restart the cycle all over switching on the MOT beams. Here, since we are dealing with single photons, and the process of creating the excitation is probabilistic, we perform about 500 trials in each cycle to increase the probability of success. This means that we turn on and off the optical pump, write 1, write 2, and read pulses 500 times during each cycle. This is illustrated in Fig.7.8. That is one reason why we use the Arduino Due instead of the National Instrument (NI) board of chapter 5. The NI board channels only accepts one TTL pulse for each channel for each cycle, while the Arduino Due permits more than one pulse per channel for each cycle.

We start with a 260 ns optical pump to prepare the initial state in the extreme of the Zeeman structure. After that we switch on the write field 1 for 52 ns. We use an OR gate to electronically filter the TTL signals emitted by the APDs. We leave only a window around each write pulse, which is when the photon from the process is emitted. We do the same for the write field 2. Finally, we switch on the read field for 500ns.

7.9 Alignment

The reading beam comes through a different fiber, in the counter-propagating direction with the same transverse mode as the writing fields. The $\chi^{(3)}$ reading field is exactly counter-

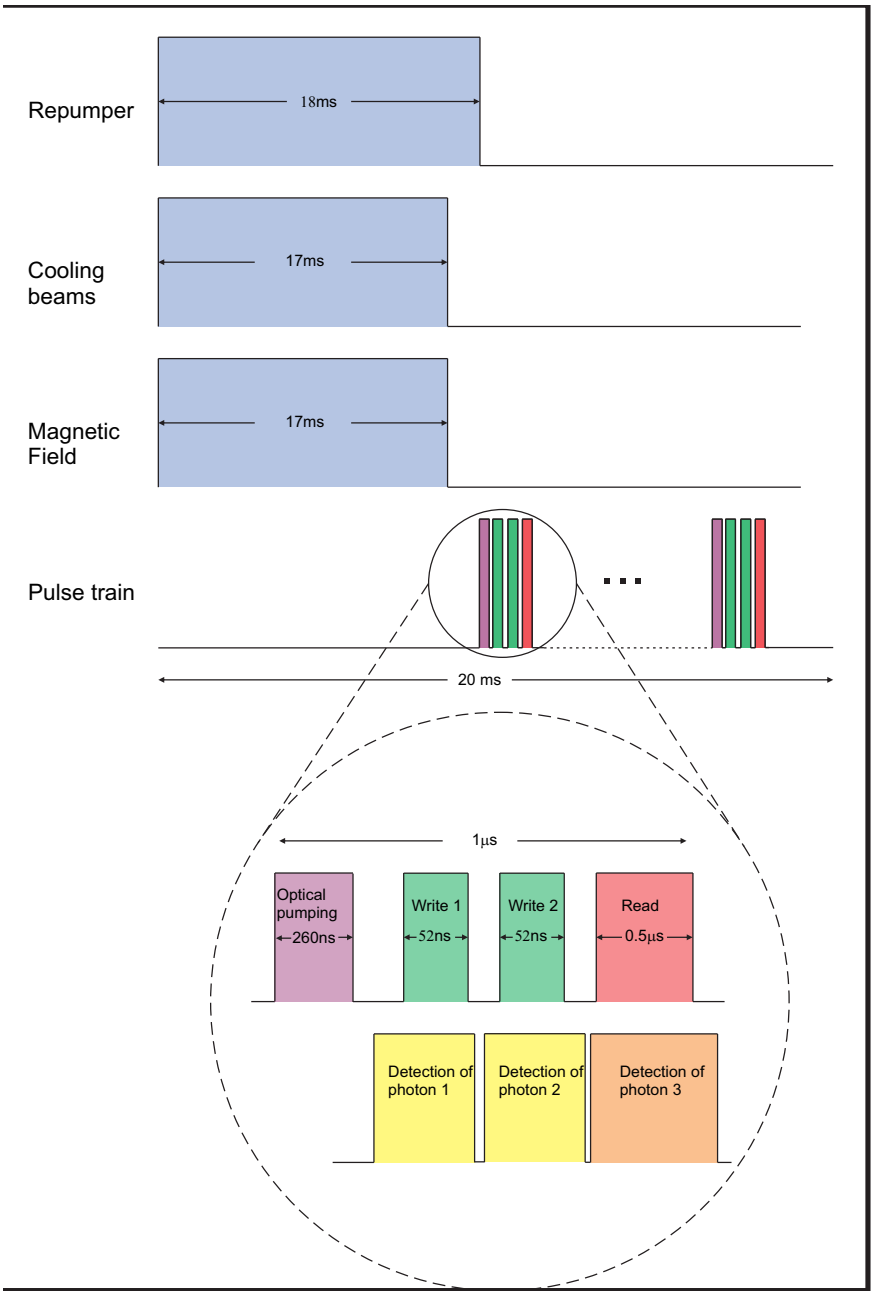

Figure 7.8 Experiment Pulse Sequence. The cooling and repumper beams stay on for 17ms and 18ms, respectively. The MOT magnetic field remains on during the same 17ms of the repumper. We perform about 500 write and read trials in each cycle to increase the probability of detecting three photons. This means that we turn on and off the optical pump, write 1, write 2, read pulses 500 times during each cycle. A 260 ns optical pump prepares the initial state in the extreme of the Zeeman structure. After that we switch on the write field 1 for 52 ns. We use a or gate to electronically filter the TTL signals emitted by the APDs. Finally, we use switch on the read field for 500ns. For the detection of the photons 1, 2, and 3 we leave only a window around the write and read pulses which is when the photons from the process are emitted. The gates are represented by the yellow and beige pulses.

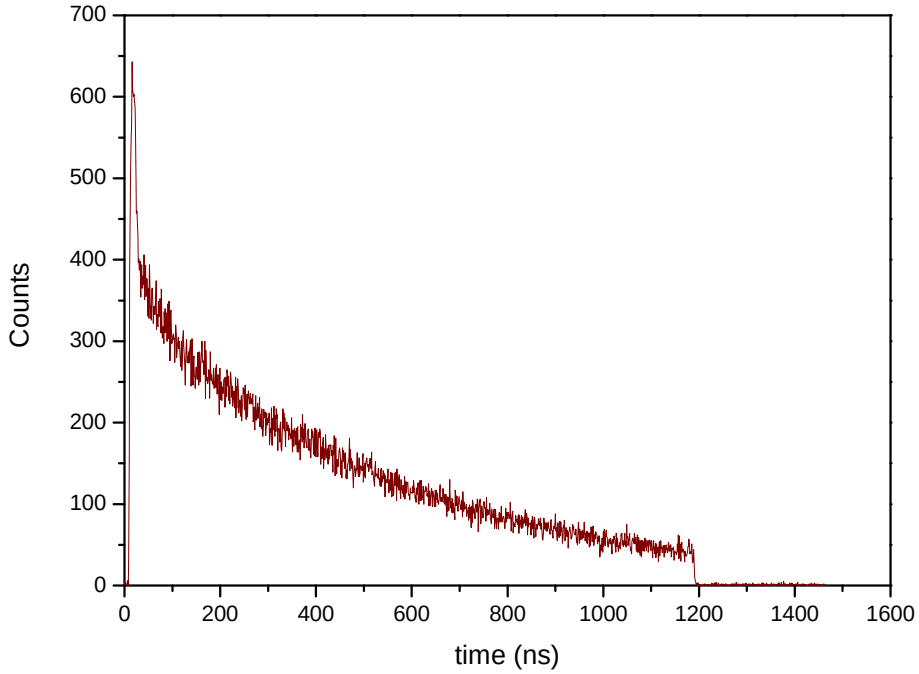

Figure 7.9 Semi-classical $\chi^{(5)}$ signal measured by the SPCM.

propagating to the writing fields and the $\chi^{(5)}$ reading field makes an angle $\theta \approx 1^\circ$ with respect to the $\chi^{(3)}$ reading field. For the $\chi^{(3)}$ signal, the read beam is coupled to the writing beam fiber with 70% efficiency. This guarantees both that they are exactly counter-propagating and have the same transverse mode along the path, including inside the MOT, where it matters the most. The same is done for photons 1 and 2 emitted during the process. We use an input field for alignment in the fibers used to collect the photons. For the $\chi^{(5)}$ process, it is more complicated since the beams are neither counter-propagating, nor have the same transverse mode. In fact, before assembling the set up for the single-photon experiment we analyzed the transverse mode for the $\chi^{(5)}$ semi-classical signal. We identified that the $\chi^{(5)}$ signal defocus faster than the $\chi^{(3)}$. This is expected since the signal is a convolution of all modes. In the polarization expression

$$P = \chi^{(3)} E_W E_{p_1} E_R + \chi^{(5)} \left(E_W E_{p_1}\right)^2 E_R \,, \tag{7.7}$$

we see that if the write field is the exact conjugate of the read field ($E_R = E_W^*$), the second photon in the $\chi^{(3)}$ process will be the exact conjugate of the first ($E_{p_2} = E_{p_1}^*$). However, this does not happen for the $\chi^{(5)}$. Since all the beams are focused in the MOT, the signal (the last photon) is also generated with its focus in the MOT. Therefore, our solution is to use a 1m lens a meter away from the MOT for collimation and then couple the semi-classical signal in the fiber for alignment. Fig. 7.9 shows the semi-classical $\chi^{(5)}$ signal measured by the single photon counting module (SPCM) with more than 50% efficiency.

7.10 Conclusion

We have presented a viable scheme to produce photons triplets, which might be expanded to more photons, based on a multiwave-mixing configuration. The first write pulse excites just one atom of the ensemble in the transition leading to the emission of one photon in the mode of *photon 1*. A second write pulse excites the same one atom back to its original states leading to the emission of the second photon in the mode of *photon 2*. A read field finishes the process exciting the atom leading to the emission of the third photon in the mode of *photon 3* in the phased-matched direction. The process can be expanded to other nonlinear orders like $\chi^{(7)}$, $\chi^{(9)}$, etc.

Since nonlinear optics is the standard method to observe many interesting quantum states of light, like squeezed states observed in the production of photons pairs, we would also expect that the final state of the triplets will provide the observation of other new quantum states of light.

Chapter 8

Conclusions

Here we give the final remarks and discuss the perspectives of the work of this thesis. First, we have presented an investigation of the writing and readout processes of an optical memory using higher-order nonlinearities in an atomic medium. A characterization of the dependence with the intensities of the writing and the reading beams was performed. It was shown that the information is encoded either in the population or in the coherence of the Zeeman structure of the hyperfine cesium ground state depending on the order of nonlinearity. The retrieved signal associated with an odd number of interactions with the writing beams [$\chi^{(3)}$, $\chi^{(7)}$, etc.] is stored only in the coherence. However, for an even number of interactions [$\chi^{(5)}$, $\chi^{(9)}$, etc.], the signal exists only in the populations. This leads to two different processes, which by consequence leads to differences in memory features that can be explored for different applications. It is also shown that each order has a different decay time that decreases as the order increases.

We also propose that these quantum memories can integrate a few of the desired properties for a quantum memory inside a single process. For instance, we show that, with the $\chi^{(5)}$ and $\chi^{(7)}$ processes, it is possible to combine storage and processing abilities in a single process. We demonstrate this by adding orbital angular momentum in the write fields. As the fields interact with the ensemble, each atom will accumulate a different amount of OAM from the applied laser beams for each nonlinear process. As a result the new field generated at the read process can have a different charge from the original ones.

The same scheme used here can be in principle applied in the single-photon regime. We propose a method to generate triplets of correlated photons based on the six-wave mixing configuration presented in the semi-classical experiments in this thesis. The idea is to use the many photons that are naturally involved in multiwave-mixing processes to signalize two photons [in the case of the $\chi^{(5)}$] or more [in the case of the $\chi^{(7)}$, $\chi^{(9)}$, etc.] with one. More explicitly one has one absorption in the mode W_1 and one emission in the mode of $photon1$, followed by a second absorption in the mode W_2 and one emission in the mode of the $photon2$, followed by a one-photon absorption of R and one-photon emission of $photon3$ in the phased-matched direction.

Finally, we present the amplification of an optical vortex beam carrying orbital angular momentum via induced narrow Raman gain in an ensemble of cold cesium atoms. This might be useful for classical communication using OAM, where reversing the propagation losses, especially for long distances, is crucial.

We expect that the results and proposals presented here contribute to the development of quantum memories and quantum optics, opening new perspectives in these fields.

Appendix A - Quantities of the steady-state solution

The quantities related to the steady-state solution are listed below.

$$A = \frac{(2\rho^{(0)}_{1a,1a} - \frac{1}{2})\left[2\alpha|\Omega_W|^2 - \alpha\left(2\left(\frac{\Gamma}{2}\right)^2 + (1+\alpha^2)|\Omega_W|^2\right)\right] - \frac{\left(\frac{\Gamma}{2}\right)^2\left[2\left(\frac{\Gamma}{2}\right)^2 + (1-\alpha)^2|\Omega_W|^2\right]}{2\left[\left(\frac{\Gamma}{2}\right)^2 + 2|\Omega_W|^2\right]}}{\left[2\left(\frac{\Gamma}{2}\right)^2(1+\alpha^2) + (1-\alpha)^2|\Omega_W|^2\right]}, \tag{A.1a}$$

$$B = \frac{(2\rho^{(0)}_{1a,1a} - \frac{1}{2})\left[2\alpha^2\beta|\Omega_W|^2 - \beta\left(2\left(\frac{\Gamma}{2}\right)^2 + (1+\alpha^2)|\Omega_W|^2\right)\right] - \frac{\beta\left(\frac{\Gamma}{2}\right)^2\left[2\left(\frac{\Gamma}{2}\right)^2 + (1-\alpha)^2|\Omega_W|^2\right]}{2\left[\left(\frac{\Gamma}{2}\right)^2 + 2|\Omega_W|^2\right]}}{\left[2\left(\frac{\Gamma}{2}\right)^2(1+\alpha^2) + (1-\alpha)^2|\Omega_W|^2\right]}, \tag{A.1b}$$

$$C = \frac{2\alpha|\Omega_W|^2 A + \left(2\rho^{(0)}_{1a,1a} - \frac{1}{2}\right) + \frac{\left(\frac{\Gamma}{2}\right)^2}{2\left[\left(\frac{\Gamma}{2}\right)^2 + 2|\Omega_W|^2\right]}}{2\left(\frac{\Gamma}{2}\right)^2 + (1+\alpha^2)|\Omega_W|^2}, \tag{A.1c}$$

$$D = \frac{2\alpha|\Omega_W|^2 B + \alpha\beta\left(2\rho^{(0)}_{1a,1a} - \frac{1}{2}\right) + \frac{\beta\left(\frac{\Gamma}{2}\right)^2}{2\left[\left(\frac{\Gamma}{2}\right)^2 + 2|\Omega_W|^2\right]}}{2\left(\frac{\Gamma}{2}\right)^2 + (1+\alpha^2)|\Omega_W|^2}, \tag{A.1d}$$

$$E = \frac{\left[2\rho^{(0)}_{1a,1a} - \frac{1}{2} + \alpha A|\Omega_W|^2 - C|\Omega_W|^2\right]}{\frac{\Gamma}{2}}, \tag{A.1e}$$

$$F = \frac{[\alpha B - D]}{\frac{\Gamma}{2}}, \tag{A.1f}$$

$$G = \frac{\left[\beta\left(2\rho^{(0)}_{1a,1a} - \frac{1}{2}\right) + B|\Omega_W|^2 - \alpha D|\Omega_W|^2\right]}{\frac{\Gamma}{2}}, \tag{A.1g}$$

$$H = \frac{[A - \alpha C]}{\frac{\Gamma}{2}}, \tag{A.1h}$$

$$I = \frac{2|\Omega_{W'}|^2}{8\left(\frac{\Gamma}{2}\right)^2|\Omega_W|^2\left[\left(\frac{\Gamma}{2}\right)^2(1+\alpha^2) + 4\alpha^2|\Omega_W|^2\right]} \times$$

$$\left\{\beta\frac{\Gamma}{2}G\left[8|\Omega_W|^2\left[\left(\frac{\Gamma}{2}\right)^2+2\alpha^2|\Omega_W|^2\right]+4\left(\frac{\Gamma}{2}\right)^2\left[\left(\frac{\Gamma}{2}\right)^2+\alpha^2|\Omega_W|^2\right]\right]\right.$$
$$-2\Gamma E\left[\left(\frac{\Gamma}{2}\right)^2+|\Omega_W|^2\right]\left[\left(\frac{\Gamma}{2}\right)^2+4\alpha^2|\Omega_W|^2\right]$$
$$+2|\Omega_W|^2\left(\frac{\Gamma}{2}\right)^2\left[\alpha A\left[2\left(\frac{\Gamma}{2}\right)^2+2|\Omega_W|^2\right]-\beta B\left[2\left(\frac{\Gamma}{2}\right)^2+6\alpha^2|\Omega_W|^2\right]\right]$$
$$+2|\Omega_W|^2\left(\frac{\Gamma}{2}\right)^2\left[C\left[2\left(\frac{\Gamma}{2}\right)^2+6\alpha^2|\Omega_W|^2\right]-\alpha\beta D\left[2\left(\frac{\Gamma}{2}\right)^2+2|\Omega_W|^2\right]\right]$$
$$\left.+2\alpha^2|\Omega_W|^2\left(\frac{\Gamma}{2}\right)^2\left[2\left(\frac{\Gamma}{2}\right)^2+2|\Omega_W|^2\right]\right\}, \tag{A.1i}$$

$$J=\frac{1}{8\left(\frac{\Gamma}{2}\right)^2|\Omega_W|^2\left[\left(\frac{\Gamma}{2}\right)^2(1+\alpha^2)+4\alpha^2|\Omega_W|^2\right]}\times$$
$$\left\{\beta\frac{\Gamma}{2}H\left[8|\Omega_W|^2\left[\left(\frac{\Gamma}{2}\right)^2+2\alpha^2|\Omega_W|^2\right]+4\left(\frac{\Gamma}{2}\right)^2\left[\left(\frac{\Gamma}{2}\right)^2+\alpha^2|\Omega_W|^2\right]\right]\right.$$
$$-2\Gamma F\left[\left(\frac{\Gamma}{2}\right)^2+|\Omega_W|^2\right]\left[\left(\frac{\Gamma}{2}\right)^2+4\alpha^2|\Omega_W|^2\right]$$
$$+2|\Omega_W|^2\left(\frac{\Gamma}{2}\right)^2\left[\alpha B\left[2\left(\frac{\Gamma}{2}\right)^2+2|\Omega_W|^2\right]-\beta A\left[2\left(\frac{\Gamma}{2}\right)^2+6\alpha^2|\Omega_W|^2\right]\right]$$
$$\left.+2|\Omega_W|^2\left(\frac{\Gamma}{2}\right)^2\left[D\left[2\left(\frac{\Gamma}{2}\right)^2+6\alpha^2|\Omega_W|^2\right]-\alpha\beta C\left[2\left(\frac{\Gamma}{2}\right)^2+2|\Omega_W|^2\right]\right]\right\}, \tag{A.1j}$$

$$K=\frac{2|\Omega_W\Omega_{W'}|^2\left[2\left(\frac{\Gamma}{2}\right)^2(\alpha\beta D+\alpha A)+\Gamma\alpha^2E\right]-\left[2\left(\frac{\Gamma}{2}\right)^2+2\alpha^2|\Omega_W|^2\right]\left[2|\Omega_{W'}|^2G\beta\frac{\Gamma}{2}-\left(\frac{\Gamma}{2}\right)^2(1-I)\right]}{2\left(\frac{\Gamma}{2}\right)^2\left[\left(\frac{\Gamma}{2}\right)^2+3\alpha^2|\Omega_W|^2\right]}, \tag{A.1k}$$

$$L=\frac{2\left(\frac{\Gamma}{2}\right)^2\left(\alpha\beta C+\alpha B\right)+2\alpha^2|\Omega_W|^2\frac{\Gamma}{2}F-\left[2\left(\frac{\Gamma}{2}\right)^2+2\alpha^2|\Omega_W|^2\right]\left[\beta\frac{\Gamma}{2}H+\left(\frac{\Gamma}{2}\right)^2J\right]}{2\left(\frac{\Gamma}{2}\right)^2\left[\left(\frac{\Gamma}{2}\right)^2+3\alpha^2|\Omega_W|^2\right]}, \tag{A.1l}$$

$$M=\frac{\left[\Gamma\beta|\Omega_{W'}|^2G+2|\Omega_W\Omega_{W'}|^2\left(\beta B-C\right)+2|\Omega_W|^2I\right]}{\left[2\left(\frac{\Gamma}{2}\right)^2+2|\Omega_W|^2\right]}, \tag{A.1m}$$

$$N=\frac{\left[\frac{\Gamma}{2}\beta H+\beta A-D+2|\Omega_W|^2J\right]}{\left[2\left(\frac{\Gamma}{2}\right)^2+2|\Omega_W|^2\right]}, \tag{A.1n}$$

$$O = \frac{\left[\Gamma|\Omega_{W'}|^2 E + 2|\Omega_W \Omega_{W'}|^2\left(\alpha A - \alpha\beta D\right) + 2\alpha^2|\Omega_W|^2 K\right]}{\left[2\left(\frac{\Gamma}{2}\right)^2 + 2\alpha^2|\Omega_W|^2\right]}\,, \tag{A.1o}$$

$$P = \frac{\left[\frac{\Gamma}{2}F + \alpha B - \alpha\beta C + 2\alpha^2|\Omega_W|^2 L\right]}{\left[2\left(\frac{\Gamma}{2}\right)^2 + 2\alpha^2|\Omega_W|^2\right]}\,, \tag{A.1p}$$

$$Q = \frac{I - M + |\Omega_{W'}|^2(\beta B - C)}{\frac{\Gamma}{2}}\,, \tag{A.1q}$$

$$R = \frac{\beta A - D + |\Omega_W|^2(J - N)}{\frac{\Gamma}{2}}\,, \tag{A.1r}$$

$$S = \frac{\alpha(K - O) + |\Omega_{W'}|^2(-\beta D + A)}{\frac{\Gamma}{2}}\,, \tag{A.1s}$$

$$T = \frac{-\beta C + B + \alpha|\Omega_W|^2(L - P)}{\frac{\Gamma}{2}}\,, \tag{A.1t}$$

$$U = \frac{1}{|\Omega_W|^2\left[2\left(\frac{\Gamma}{2}\right)^2(1+\alpha^2) + (1-\alpha^2)|\Omega_W|^2\right]} \times$$
$$\left\{ -\alpha\left[2\left(\frac{\Gamma}{2}\right)^2 - (1-\alpha^2)|\Omega_W|^2\right](I - O) - \beta\left[2\left(\frac{\Gamma}{2}\right)^2 + (1-\alpha^2)|\Omega_W|^2\right]|\Omega_W \Omega_{W'}|^2(L - N)\right.$$
$$\left. -\left[2\left(\frac{\Gamma}{2}\right)^2 + (1+\alpha^2)|\Omega_W|^2\right]\frac{\Gamma}{2}(|\Omega_W|^2\beta R + S) + 2\alpha^2|\Omega_W|^2\frac{\Gamma}{2}(\beta|\Omega_{W'}|^2 T + Q)\right\}\,, \tag{A.1u}$$

$$X = \frac{1}{|\Omega_W|^2\left[2\left(\frac{\Gamma}{2}\right)^2(1+\alpha^2) + (1-\alpha^2)|\Omega_W|^2\right]} \times$$
$$\left\{ -\beta\left[2\left(\frac{\Gamma}{2}\right)^2 + (1-\alpha^2)|\Omega_W|^2\right](K - M) - \alpha\left[2\left(\frac{\Gamma}{2}\right)^2 - (1-\alpha^2)|\Omega_W|^2\right]|\Omega_W \Omega_{W'}|^2(J - P)\right.$$
$$\left. -\left[2\left(\frac{\Gamma}{2}\right)^2 + (1+\alpha^2)|\Omega_W|^2\right]\frac{\Gamma}{2}(|\Omega_{W'}|^2 T + \beta Q) + 2\alpha^2|\Omega_W|^2\frac{\Gamma}{2}(\beta S + |\Omega_{W'}|^2 R)\right\}\,, \tag{A.1v}$$

$$Y = \frac{-\alpha\left[2\left(\frac{\Gamma}{2}\right)^2 - (1-\alpha^2)|\Omega_W|^2\right](J - P) - \left[2\left(\frac{\Gamma}{2}\right)^2 + (1+\alpha^2)|\Omega_W|^2\right]\alpha(L - P) + 2\alpha^2|\Omega_W|^2\alpha\beta(J - N)}{|\Omega_W|^2\left[2\left(\frac{\Gamma}{2}\right)^2(1+\alpha^2) + (1-\alpha^2)|\Omega_W|^2\right]}\,, \tag{A.1w}$$

$$Z = \frac{-\beta\left[2\left(\frac{\Gamma}{2}\right)^2 + (1-\alpha^2)|\Omega_W|^2\right](L - N) - \left[2\left(\frac{\Gamma}{2}\right)^2 + (1+\alpha^2)|\Omega_W|^2\right](J - N) + 2\alpha^2|\Omega_W|^2\alpha\beta(L - P)}{|\Omega_W|^2\left[2\left(\frac{\Gamma}{2}\right)^2(1+\alpha^2) + (1-\alpha^2)|\Omega_W|^2\right]}\,. \tag{A.1x}$$

Bibliography

[1] T. D. Ladd, F. Jelezko, R. Laflamme, Y. Nakamura, C. Monroe, and J. L. O'Brien. Quantum computers. *Nature*, 464(7285):45–53, 2010.

[2] Nicolas Gisin, Grégoire Ribordy, Wolfgang Tittel, and Hugo Zbinden. Quantum cryptography. *Rev. Mod. Phys.*, 74:145–195, 2002.

[3] Charles H. Bennett, Gilles Brassard, Claude Crépeau, Richard Jozsa, Asher Peres, and William K. Wootters. Teleporting an unknown quantum state via dual classical and einstein-podolsky-rosen channels. *Phys. Rev. Lett.*, 70:1895–1899, 1993.

[4] Dik Bouwmeester, Jian-Wei Pan, Klaus Mattle, Manfred Eibl, Harald Weinfurter, and Anton Zeilinger. Experimental quantum teleportation. *Nature*, 390(6660):575–579, 1997.

[5] L.-M. Duan, M. D. Lukin, J. I. Cirac, and P. Zoller. Long-distance quantum communication with atomic ensembles and linear optics. *Nature*, 414(6862):413–418, 2001.

[6] H.-J. Briegel, W. Dür, J. I. Cirac, and P. Zoller. Quantum repeaters: The role of imperfect local operations in quantum communication. *Phys. Rev. Lett.*, 81:5932–5935, 1998.

[7] W. Dür, H.-J. Briegel, J. I. Cirac, and P. Zoller. Quantum repeaters based on entanglement purification. *Phys. Rev. A*, 59:169–181, 1999.

[8] Alexander I. Lvovsky, Barry C. Sanders, and Wolfgang Tittel. Optical quantum memory. *Nature Photonics*, 3(12):706–714, 2009.

[9] Mikael Afzelius, Nicolas Gisin, and Hugues de Riedmatten. Quantum memory for photons. *Physics Today*, 68(12):42–47, 2015.

[10] Khabat Heshami, Duncan G. England, Peter C. Humphreys, Philip J. Bustard, Victor M. Acosta, Joshua Nunn, and Benjamin J. Sussman. Quantum memories: emerging applications and recent advances. *Journal of Modern Optics*, 63(20):2005–2028, 2016.

[11] Félix Bussières, Nicolas Sangouard, Mikael Afzelius, Hugues de Riedmatten, Christoph Simon, and Wolfgang Tittel. Prospective applications of optical quantum memories. *Journal of Modern Optics*, 60(18):1519–1537, 2013.

[12] H. J. Kimble. The quantum internet. *Nature*, 453(7198):1023–1030, 2008.

[13] T. E. Northup and R. Blatt. Quantum information transfer using photons. *Nature Photonics*, 8(5):356–363, 2014.

[14] S. Debnath, N. M. Linke, C. Figgatt, K. A. Landsman, K. Wright, and C. Monroe. Demonstration of a small programmable quantum computer with atomic qubits. *Nature*, 536(7614):63–66, 2016.

[15] C. Monroe, R. Raussendorf, A. Ruthven, K. R. Brown, P. Maunz, L.-M. Duan, and J. Kim. Large-scale modular quantum-computer architecture with atomic memory and photonic interconnects. *Phys. Rev. A*, 89:022317, 2014.

[16] W. K. Wootters and W. H. Zurek. A single quantum cannot be cloned. *Nature*, 299(5886):802–803, 1982.

[17] W. K. Wootters and W. H. Zurek. The no-cloning theorem. *Physics Today*, 62(2):76–77, 2009.

[18] D. F. Phillips, A. Fleischhauer, A. Mair, R. L. Walsworth, and M. D. Lukin. Storage of light in atomic vapor. *Phys. Rev. Lett.*, 86:783–786, 2001.

[19] Chien Liu, Zachary Dutton, Cyrus H. Behroozi, and Lene Vestergaard Hau. Observation of coherent optical information storage in an atomic medium using halted light pulses. *Nature*, 409(6819):490–493, 2001.

[20] G. Hétet, M. Hosseini, B. M. Sparkes, D. Oblak, P. K. Lam, and B. C. Buchler. Photon echoes generated by reversing magnetic field gradients in a rubidium vapor. *Opt. Lett.*, 33(20):2323–2325, 2008.

[21] Mikael Afzelius, Christoph Simon, Hugues de Riedmatten, and Nicolas Gisin. Multimode quantum memory based on atomic frequency combs. *Phys. Rev. A*, 79:052329, 2009.

[22] Darrick E. Chang, Vladan Vuletić, and Mikhail D. Lukin. Quantum nonlinear optics — photon by photon. *Nature Photonics*, 8(9):685–694, 2014.

[23] H. Schmidt and A. Imamoglu. Giant kerr nonlinearities obtained by electromagnetically induced transparency. *Optics Letters*, 21(23):1936, 1996.

[24] Alexey V. Gorshkov, Johannes Otterbach, Michael Fleischhauer, Thomas Pohl, and Mikhail D. Lukin. Photon-photon interactions via rydberg blockade. *Physical Review Letters*, 107(13), 2011.

[25] R. A. de Oliveira, G. C. Borba, W. S. Martins, S. Barreiro, D. Felinto, and J. W. R. Tabosa. Nonlinear optical memory for manipulation of orbital angular momentum of light. *Optics Letters*, 40(21):4939, 2015.

[26] G. C. Borba, D. Felinto, and J. W. R. Tabosa. Nonlinear optical memory: theory and experiment. *Journal of the Optical Society of America B*, 34(12):2528, 2017.

[27] A. S. Coelho, F. A. S. Barbosa, K. N. Cassemiro, A. S. Villar, M. Martinelli, and P. Nussenzveig. Three-color entanglement. *Science*, 326(5954):823–826, 2009.

[28] F. A. S. Barbosa, A. S. Coelho, L. F. Muñoz Martínez, L. Ortiz-Gutiérrez, A. S. Villar, P. Nussenzveig, and M. Martinelli. Hexapartite entanglement in an above-threshold optical parametric oscillator. *Phys. Rev. Lett.*, 121:073601, 2018.

[29] Shota Yokoyama, Ryuji Ukai, Seiji C. Armstrong, Chanond Sornphiphatphong, Toshiyuki Kaji, Shigenari Suzuki, Jun ichi Yoshikawa, Hidehiro Yonezawa, Nicolas C. Menicucci, and Akira Furusawa. Ultra-large-scale continuous-variable cluster states multiplexed in the time domain. *Nature Photonics*, 7(12):982–986, 2013.

[30] D Felinto, Chin-Wen Chou, J Laurat, E. W. Schomburg, H De Riedmatten, and H. Jeff Kimble. Conditional control of the quantum states of remote atomic memories for quantum networking. *Nature Physics*, 2(12):844–848, 2006.

[31] Chin-Wen Chou, Julien Laurat, Hui Deng, Kyung Soo Choi, Hugues de Riedmatten, Daniel Felinto, and H. Jeff Kimble. Functional quantum nodes for entanglement distribution over scalable quantum networks. *Science*, 316(5829):1316–1320, 2007.

[32] T. Chanelière, D. N. Matsukevich, S. D. Jenkins, S.-Y. Lan, T. A. B. Kennedy, and A. Kuzmich. Storage and retrieval of single photons transmitted between remote quantum memories. *Nature*, 438(7069):833–836, 2005.

[33] D. N. Matsukevich, T. Chanelière, S. D. Jenkins, S.-Y. Lan, T. A. B. Kennedy, and A. Kuzmich. Entanglement of remote atomic qubits. *Phys. Rev. Lett.*, 96:030405, 2006.

[34] J. Hofmann, M. Krug, N. Ortegel, L. Gerard, M. Weber, W. Rosenfeld, and H. Weinfurter. Heralded entanglement between widely separated atoms. *Science*, 337(6090):72–75, 2012.

[35] G. C. Borba, S. Barreiro, L. Pruvost, D. Felinto, and J. W. R. Tabosa. Narrow band amplification of light carrying orbital angular momentum. *Optics Express*, 24(9):10078, 2016.

[36] C. J. Foot. *Atomic Physics*. Oxford University Press, 1 edition, 2005.

[37] H. J. Metcalf and P. van der Straten. *Laser Cooling and Trapping*. Springer, 1 edition, 1999.

[38] H. J. Metcalf and P. van der Straten. *Atoms and Molecules interacting with Light*. Cambridge University Press, 1 edition, 2016.

[39] Dmitry Budker, Derek F. Kimball, and David P. DeMille. *Atomic Physics: An exploration through problems and solutions*. Cambridge University Press, 2 edition, 2008.

[40] Claude Cohen-Tannoudji, Jacques Dupont-Roc, and Gilbert Grynberg. *Atom-Photon Interactions: Basic Processes and Applications*. Wiley-VCH, 1 edition, 1998.

[41] Massimo Inguscio and Leonardo Fallani. *Atomic Physics: Precise Measurements and Ultracold Matter*. Oxford University Press, 1 edition, 2013.

[42] Daniel A. Steck. *Quantum and Atom Optics, available online at http://steck.us/teaching (revision 0.10.6, 25 May 2016)*.

[43] J. Dalibard and C. Cohen-Tannoudji. Laser cooling below the doppler limit by polarization gradients: simple theoretical models. *Journal of the Optical Society of America B*, 6(11):2023, 1989.

[44] John David Jackson. *Classical Electrodynamics*. John Wiley & Sons, 3 edition, 1999.

[45] David J Griffiths. *Introduction to Electrodynamics*. Pearson, 3 edition, 1999.

[46] Sandra S. Vianna and Cid B. de Araujo. Coherent excitation of phonon polaritons in a centrosymmetric crystal. *Phys. Rev. Lett.*, 56:1475–1477, 1986.

[47] Robert W. Boyd. *Nonlinear optics*. Acad. Press, 2 edition, 2003.

[48] P. A. Franken, A. E. Hill, C. W. Peters, and G. Weinreich. Generation of optical harmonics. *Phys. Rev. Lett.*, 7:118–119, 1961.

[49] Y. R. Shen. *The principles of Nonlinear optics*. Wiley, 1 edition, 2002.

[50] Chunfei Li. *Nonlinear optics: Principles and Applications*. Springer, 1 edition, 2017.

[51] Amnon Yariv. *Quantum Electronics*. John Wiley & Sons, 3 edition, 1988.

[52] R.K. Raj, Q.F. Gao, D. Bloch, and M. Ducloy. Direct observation of high-order optical susceptibilities via angularly-resolved multiwave mixing. *Optics Communications*, 51(2):117 – 120, 1984.

[53] Michael Rosenbluh Yehiam Prior, Abraham Ben-Reuven. *Methods of laser spectroscopy*. Plenum Press, 1 edition, 1986.

[54] S. Le Boiteux, P. Simoneau, D. Bloch, F. De Oliveira, and M. Ducloy. Saturation behavior of resonant degenerate four-wave and multiwave mixing in the doppler-broadened regime: Experimental analysis on a low-pressure ne discharge. *IEEE Journal of Quantum Electronics*, 22(8):1229–1247, 1986.

[55] M. Ducloy and D. Bloch. Polarization properties of phase-conjugate mirrors: Angular dependence and disorienting collision effects in resonant backward four-wave mixing for doppler-broadened degenerate transitions. *Phys. Rev. A*, 30:3107–3122, 1984.

[56] Martial Ducloy. Optical phase conjugation with frequency up-conversion via high-order, nondegenerate multiwave mixing. *Applied Physics Letters*, 46(11):1020–1022, 1985.

[57] J. H. Poynting. The wave motion of a revolving shaft, and a suggestion as to the angular momentum in a beam of circularly polarised light. *Proceedings of the Royal Society A: Mathematical, Physical and Engineering Sciences*, 82(557):560–567, 1909.

[58] David L. Andrews and Mohamed Babiker. *The angular momentum of light*. Cambridge, 1 edition, 2013.

[59] Juan P. Torres and Lluis Torner. *Twisted Photons*. Wiley-VCH, 1 edition, 2011.

[60] David L. Andrews. *Structured Light and Its Applications: An Introduction to Phase-Structured Beams and Nanoscale Optical Forces*. Academic Press, 1 edition, 2008.

[61] S.J. van Enk and G. Nienhuis. Eigenfunction description of laser beams and orbital angular momentum of light. *Optics Communications*, 94(1-3):147–158, 1992.

[62] N. R. Heckenberg, R. McDuff, C. P. Smith, and A. G. White. Generation of optical phase singularities by computer-generated holograms. *Optics Letters*, 17(3):221, 1992.

[63] Manuel Erhard, Robert Fickler, Mario Krenn, and Anton Zeilinger. Twisted photons: new quantum perspectives in high dimensions. *Light: Science & Applications*, 7(3):17146, 2017.

[64] Earl T. Campbell, Hussain Anwar, and Dan E. Browne. Magic-state distillation in all prime dimensions using quantum reed-muller codes. *Phys. Rev. X*, 2:041021, 2012.

[65] Alex Bocharov, Martin Roetteler, and Krysta M. Svore. Factoring with qutrits: Shor's algorithm on ternary and metaplectic quantum architectures. *Phys. Rev. A*, 96:012306, 2017.

[66] Toshihiko Sasaki, Yoshihisa Yamamoto, and Masato Koashi. Practical quantum key distribution protocol without monitoring signal disturbance. *Nature*, 509(7501):475–478, 2014.

[67] Hiroki Takesue, Toshihiko Sasaki, Kiyoshi Tamaki, and Masato Koashi. Experimental quantum key distribution without monitoring signal disturbance. *Nature Photonics*, 9(12):827–831, 2015.

[68] L. Veissier. *Quantum memory protocols in large cold atomic ensembles*. Thèse de doctorat, Université Pierre et Marrie Curie, Laboratoire Kastler-Brossel, 2013.

[69] D. Moretti, D. Felinto, J. W. R. Tabosa, and A. Lezama. Dynamics of a stored zeeman coherence grating in an external magnetic field. *Journal of Physics B: Atomic, Molecular and Optical Physics*, 43(11):115502, 2010.

[70] Daniel Adam Steck. Cesium d line data. 01 2010.

[71] William D. Phillips. Nobel lecture: Laser cooling and trapping of neutral atoms. *Rev. Mod. Phys.*, 70:721–741, 1998.

[72] D. Felinto, D. Moretti, R. A. de Oliveira, and J. W. R. Tabosa. Delayed four- and six-wave mixing in a coherently prepared atomic ensemble. *Optics Letters*, 35(23):3937, 2010.

[73] D. Felinto, C. W. Chou, H. de Riedmatten, S. V. Polyakov, and H. J. Kimble. Control of decoherence in the generation of photon pairs from atomic ensembles. *Physical Review A*, 72(5), 2005.

[74] Bo Zhao, Yu-Ao Chen, Xiao-Hui Bao, Thorsten Strassel, Chih-Sung Chuu, Xian-Min Jin, Jörg Schmiedmayer, Zhen-Sheng Yuan, Shuai Chen, and Jian-Wei Pan. A millisecond quantum memory for scalable quantum networks. *Nature Physics*, 5(2):95–99, 2008.

[75] R. Zhao, Y. O. Dudin, S. D. Jenkins, C. J. Campbell, D. N. Matsukevich, T. A. B. Kennedy, and A. Kuzmich. Long-lived quantum memory. *Nature Physics*, 5(2):100–104, 2008.

[76] A. J. F. de Almeida, M.-A. Maynard, C. Banerjee, D. Felinto, F. Goldfarb, and J. W. R. Tabosa. Nonvolatile optical memory via recoil-induced resonance in a pure two-level system. *Phys. Rev. A*, 94:063834, 2016.

[77] D. Moretti, D. Felinto, and J. W.R. Tabosa. Pulse pair generation from coherently prepared atomic ensembles. *The European Physical Journal D*, 60(2):373–382, 2010.

[78] J.W.R Tabosa, A Lezama, and G.C Cardoso. Transient bragg diffraction by a transferred population grating: application for cold atoms velocimetry. *Optics Communications*, 165(1–3):59 – 64, 1999.

[79] Franck Laloën Claude Cohen-Tannoudji, Bernard Diu. *Quantum Mechanics*. John Wiley & Sons, 1 edition, 2005.

[80] William H. Press, Saul A. Teukolsky, William T. Vetterling, and Brian P. Flannery. *Numerical Recipes: The Art of Scientific Computing*. Cambridge University Press, 3 edition, 2007.

[81] R. A. de Oliveira, D. Moretti, D. Felinto, and J. W. R. Tabosa. Readout spectroscopy of an atomic memory. *Phys. Rev. A*, 86:013839, 2012.

[82] Y. O. Dudin, L. Li, and A. Kuzmich. Light storage on the time scale of a minute. *Phys. Rev. A*, 87:031801, 2013.

[83] Yan Jiang, Jun Rui, Xiao-Hui Bao, and Jian-Wei Pan. Dynamical zeroing of spin-wave momentum to suppress motional dephasing in an atomic-ensemble quantum memory. *Phys. Rev. A*, 93:063819, 2016.

[84] Pravin Vaity, J. Banerji, and R.P. Singh. Measuring the topological charge of an optical vortex by using a tilted convex lens. *Physics Letters A*, 377(15):1154 – 1156, 2013.

[85] H. I. Sztul and R. R. Alfano. Double-slit interference with laguerre-gaussian beams. *Optics Letters*, 31(7):999, 2006.

[86] J. M. Hickmann, E. J. S. Fonseca, W. C. Soares, and S. Chávez-Cerda. Unveiling a truncated optical lattice associated with a triangular aperture using light's orbital angular momentum. *Phys. Rev. Lett.*, 105:053904, 2010.

[87] Mariia Shutova, Alexandra A. Zhdanova, and Alexei V. Sokolov. Detection of mixed OAM states via vortex breakup. *Physics Letters A*, 381(4):408–412, 2017.

[88] L. Allen, M. W. Beijersbergen, R. J. C. Spreeuw, and J. P. Woerdman. Orbital angular momentum of light and the transformation of laguerre-gaussian laser modes. *Phys. Rev. A*, 45:8185–8189, 1992.

[89] David G. Grier. A revolution in optical manipulation. *Nature*, 424(6950):810–816, 2003.

[90] Lluis Torner, Juan P. Torres, and Silvia Carrasco. Digital spiral imaging. *Optics Express*, 13(3):873, 2005.

[91] H. Bechmann-Pasquinucci and W. Tittel. Quantum cryptography using larger alphabets. *Phys. Rev. A*, 61:062308, 2000.

[92] Yan Yan, Guodong Xie, Martin P. J. Lavery, Hao Huang, Nisar Ahmed, Changjing Bao, Yongxiong Ren, Yinwen Cao, Long Li, Zhe Zhao, Andreas F. Molisch, Moshe Tur, Miles J. Padgett, and Alan E. Willner. High-capacity millimetre-wave communications with orbital angular momentum multiplexing. *Nature Communications*, 5(1), 2014.

[93] Asher J. Willner, Yongxiong Ren, Guodong Xie, Zhe Zhao, Yinwen Cao, Long Li, Nisar Ahmed, Zhe Wang, Yan Yan, Peicheng Liao, Cong Liu, Mohammad Mirhosseini, Robert W. Boyd, Moshe Tur, and Alan E. Willner. Experimental demonstration of 20 gbit/s data encoding and 2 ns channel hopping using orbital angular momentum modes. *Optics Letters*, 40(24):5810, 2015.

[94] D. F. Walls. Squeezed states of light. *Nature*, 306(5939):141–146, 1983.

[95] A. I. Lvovsky, H. Hansen, T. Aichele, O. Benson, J. Mlynek, and S. Schiller. Quantum state reconstruction of the single-photon fock state. *Phys. Rev. Lett.*, 87:050402, 2001.

[96] Aditi Sen De and Ujjwalr Sen. Quantum advantage in communication networks. *Physics News*, 40(4):17–32, 2010.

[97] Géza Tóth. Multipartite entanglement and high-precision metrology. *Phys. Rev. A*, 85:022322, 2012.

[98] Anders S. Sørensen and Klaus Mølmer. Entanglement and extreme spin squeezing. *Phys. Rev. Lett.*, 86:4431–4434, 2001.

[99] Daniel M. Greenberger, Michael A. Horne, Abner Shimony, and Anton Zeilinger. Bell's theorem without inequalities. *American Journal of Physics*, 58(12):1131–1143, 1990.

[100] J. Persson, T. Aichele, V. Zwiller, L. Samuelson, and O. Benson. Three-photon cascade from single self-assembled inp quantum dots. *Phys. Rev. B*, 69:233314, 2004.

[101] Timothy E. Keller, Morton H. Rubin, Yanhua Shih, and Ling-An Wu. Theory of the three-photon entangled state. *Phys. Rev. A*, 57:2076–2079, 1998.

[102] Hannes Hübel, Deny R. Hamel, Alessandro Fedrizzi, Sven Ramelow, Kevin J. Resch, and Thomas Jennewein. Direct generation of photon triplets using cascaded photon-pair sources. *Nature*, 466(7306):601–603, 2010.

[103] Kamel Bencheikh, Fabien Gravier, Julien Douady, Ariel Levenson, and Benoît Boulanger. Triple photons: a challenge in nonlinear and quantum optics. *Comptes Rendus Physique*, 8(2):206 – 220, 2007.

[104] Daniel Adam Steck. Rubidium 87 d line data. 01 2003.